Experimental Evaluation of the Interfacial Dzyaloshinskii-Moriya Interaction in Co/Ni Magnetic Multilayers

Submitted in partial fulfillment of the requirements for

the degree of

Doctor of Materials Science and Engineering

in

Materials Science and Engineering

Derek K. Lau

B.S., Nanoengineering, University of California, San Diego
M.S., Materials Science and Engineering, Carnegie Mellon University

Carnegie Mellon University
Pittsburgh, PA

August, 2018

Abstract

In this thesis work, different approaches to engineer spin-orbit coupling phenomena has been explored experimentally because of their importance in next generation spintronic devices. The studies are focused primarily on tuning the Dzyaloshinskii-Moriya Interaction for more efficient current-induced domain wall motion in thin films composed of Co/Ni repeating magnetic layers.

The Dzyaloshinskii-Moriya Interaction (DMI) is initially characterized for the Pt / $[Co/Ni]_{2.5}$ / Ta system to develop a suitable experimental methodology for future material systems. We performed preliminary studies on the system in order to obtain the necessary texture, perpendicular anisotropy, coercivity, and film morphology. In order to characterize the interfacial DMI, we measure field-driven, asymmetric domain wall growth through the use of a Magneto-Optical Kerr Effect Microscope (MOKE). Using this technique, we are able to determine the effective field (H_{DMI}) generated by the interfacial DMI. This experimental characterization was significant in the development of a comprehensive model for describing domain wall behavior, used to guide the analysis of subsequent studies.

Despite the ubiquitous role of alloying in developing magnetic materials, there have been few studies of its impact on DMI in heavy metal seedlayers. We used combinatorial techniques to examine a range of heavy metal alloy seedlayers. A $[Co/Ni]_{2.5}/Ta$ multilayer is deposited on top of a seedlayer solid solution with a composition gradient. We have characterized the $Pt - Ir$ system to find that the DMI changes magnitude as one moves across the composition range. A similar trend has been characterized in the $Pt - Au$ alloyed seedlayer systems. We have demonstrated that other factors (namely chiral damping effects) not related to DMI may be contributing to domain wall motion. In addition, we have also been able to characterize the effect of seedlayer alloying on the efficiency of current-induced domain wall motion (CIDWM), which is ultimately the metric that matters for future domain wall devices. We show a correlation between DMI and device performance to demonstrate the viability of tuning device performance through seedlayer composition.

Finally, we discuss preliminary results for a study to characterize the effects of capping layer interfaces on the effective DMI induced in a magnetic multilayer. There are relative

magnitude differences between different heavy metal/ferromagnet (and vice versa) interfaces, which have implications for tuning DMI by designing the magnetic multilayer structure. Continuing this study through computational and experimental work shows potential for engineering of DMI in superlattice structures or magnetic multilayers for spintronics applications.

ACKNOWLEDGEMENTS

I would first like to recognize and thank my advisor Professor Vincent Sokalski who made all this work possible. Without his guidance and support, my growth as a researcher and scientist during my graduate school career would not have been possible. I have learned so much working with him and I am very grateful for the experience.

I would also like to thank my committee members, Profesor David E. Laughlin, Professor Michael E. McHenry, and Dr. Luc Thomas. Their input during this thesis work has been significant in guiding the course of this project. Most importantly, their critique and insight has been instrumental in challenging and developing my own knowledge of materials science.

Since this research work was a collaborative effort, I would like to thank the colleagues that I have had the pleasure of working with over the last four years. Dr. Price Pellegren was crucial in developing a new model for domain wall motion that was pivotal to understanding my experimental work. His efforts have made a lot of my thesis work possible and much more compelling. I would also like to thank Dr. Masaki Furuta who offered much guidance and advice with my research work. His knowledge of magnetism, device fabrication, device testing/characterization certainly made my life easier and I am grateful for his willingness to help and teach. I am also thankful for Bing Zhao, Yang Liu, and Dr. Vignesh Sundar who

have also helped me develop the skills necessary to complete this thesis work. This thesis work would not be possible without the expertise and the dedication of the Nanofabrication staff at CMU and I am grateful for all their help over the years. I would also like to thank Hans Nembach and Justin Shaw at NIST for their important contributions to my research as collaborators.

I have made some great friends here in Pittsburgh and I would like to thank everyone for making my life here so enjoyable. In particular, I would like to thank Dr. Simon Lu, Dr. Kevin Parrish, Dr. Ryan Harrison, Paul Choi, Alice Perrin, Tim Hsu, Maxwell Li, Andrew Kitahara, who have had to deal with me on a daily basis. A special shout-out to Michael Chen and Joseph Huang for their friendship from across the country. And, of course, my girlfriend Connie Yen has my most heartfelt gratitude for her understanding and encouragement during my doctorate career. I am fortunate to have her in my life.

Finally, I would like to thank my family for their endless support and patience through everything. Raymond Lau and Vicki Lau are a constant source of inspiration and guidance. Without my parents, Yiu Keung Lau and Yue Shao Li, I would not be the person I am today. Without their sacrifices, I would not have any of the opportunities I have been blessed with. I dedicate this thesis to them.

List of Publications Resulting from this Work

The following papers related to the work presented in this thesis have been published or submitted:

1. **D. Lau**, J. P. Pellegren, H. T. Nembach, J. M. Shaw, and V. Sokalski. (2017). Disentangling factors governing Dzyaloshinskii domain wall creep in Co/Ni thin films using Pt_xIr_{1-x} Seedlayers. *Physical Review B.* (In Preparation)

2. J. P. Pellegren, **D. Lau**, and V. Sokalski. (2017). Dispersive Stiffness of Dzyaloshinskii Domain Walls. *Physical Review Letters*, 119, 027203

3. M. Jaris, **D. Lau**, V. Sokalski, and H. Schmidt. (2017). Magnetization dynamics and damping behavior of Co/Ni multilayers with a graded Ta capping layer. *Journal of Applied Physics*, 121(16), 163903.

4. **D. Lau**, V. Sundar, J. G. Zhu, and V. Sokalski. (2016). Energetic molding of chiral magnetic bubbles. *Physical Review B*, 94(6), 060401. (Rapid Communications, Editor's Suggestion)

List of Presentations Resulting from this Work

The following presentations related to the work presented in this thesis have been published or submitted:

1. **D. Lau**, J. P. Pellegren, H. Nembach, J. M. Shaw, and V. Sokalski. (2019). Assessing a refined elastic model of Dzyaloshinskii domain wall creep using composition graded Pt-Ir- Au seedlayers in Co/Ni heterostructures. *2019 Joint MMM-Intermag Conference* (Submitted).

2. **D. Lau**, J. P. Pellegren, and V. Sokalski. (2018). Effect of Seedlayer Composition on Interfacial DMI in Co/Ni Multilayers. *International Conference on Magnetism (ICM)*.

3. **D. Lau**, J. P. Pellegren, and V. Sokalski. (2017). Effect of Pt-Ir Intermixing in Co/Ni Thin Film Seedlayers on Interfacial DMI. 62nd *Annual Conference on Magnetism and Magnetic Materials (MMM)*.

4. **D. Lau**, J. P. Pellegren, P. Rengasamy, and V. Sokalski. (2016). Impact of Ta-Mo Seedlayer Alloying on the Interfacial DMI in FeCoB/MgO Thin Films. 61st *Annual Conference on Magnetism and Magnetic Materials (MMM)*.

5. **D. Lau**, J. P. Pellegren, V. Sundar, J. G. Zhu, and V. Sokalski. (2016). Energetic Calculations fo Chiral Magnetic Bubble Domains. 16th *Annual Non-Volatile Memory Technology Symposium (NVMTS)*.

6. **D. Lau**, V. Sundar, J. G. Zhu, and V. Sokalski. (2016). Asymmetric Chiral Domain Growth in Perpendicular Co/Ni Multi-layers Influenced by the DMI. 13th *Joint MMM-Intermag Conference*.

TABLE OF CONTENTS

LIST OF FIGURES

CHAPTER I

Introduction and Motivation

With the increasingly ubiquitous nature of computers and electronic devices in the modern world, the demand for advances in their performance, storage capabilities, and energy efficiency has also grown. To meet those demands, semiconductor technology has been advancing at an extremely fast rate. According to Moore's Law, the density and performance of semiconductor device is predicted to double every two years, improving with each generation. Since it was postulated in 1975, the trend has been met and advancements in technology have been consistent. Due to advancements in fabrication techniques, transistors have continually decreased in size over the past few decades. However, the semiconductor industry is rapidly approaching the physical size limit of Moore's law as transistors shrink to below $10nm$. Beyond the size limit, transistors encounter additional concerns, including heat dissipation issues and quantum effects. Researchers, both in academia and industry, are currently exploring new and innovative technologies as alternatives to transistor technology in an effort to meet the expectations of Moore's Law. The emerging field of spintronics shows a lot of potential as the alternative to conventional semiconductor technology. Instead of incorporating electron charge to produce functional devices, spintronic devices relies heavily on the combination of electron charge and electron spin. The digital storage industry is one of the fields receiving a lot of attention in their efforts to incorporate spintronics into their technology. Data storage has transitioned from analogue devices, to magnetic media, to solid state devices. The next generation of data storage is already being explored as many novel devices have been discussed in recent literature. Technologies such as MRAM and magnetic racetrack devices have been proposed as the answer for

non-volatile, energy efficient, high-density, and high-performance data storage. However, spin phenomena critical for these next generation devices, such as the Dzyaloshinskii-Moriya Interaction (DMI), the Spin-Hall Effect (SHE), spin-transfer torque, and current-induced domain wall motion are still not completely understood [1]. In this thesis, we perform a set of experimental measurements on perpendicular magnetic multilayers to explore new materials and elucidate information about the role of these emergent phenomena.

1.1 Domain Wall Devices

Domain wall motion devices are expected to play a significant part in advancing spintronic technology. Racetrack memory [1, 2] and some MRAM applications [3] incorporate domain wall motion in their designs. More primitive domain wall devices fabricated from soft magnetic materials, mainly Permalloy, were shown to move domain walls slower and were not as stable for practical applications [1, 4]. The potential for highly efficient domain wall motion devices originating from spin-orbit torques was first observed in Co/Ni multilayers [5–7]. They demonstrate the functionality of prototype racetrack memory by fabricating a domain wall nanowire shift register. With it, they have shown that a domain wall can be written at one end of the nano shift register and read at the other end by moving them along the nanowire using current pulses [4, 7]. The rise of chiral magnetism is important to the development of domain wall devices because they had the capability to induce higher domain wall velocities, denser capacities, and more stable domain walls, at the same current densities. Advancements in domain wall motion have been made possible from a better understanding of spin-orbit coupling phenomena. An increase in magneto-crystalline anisotropy, for example, is shown exhibit smaller and more robust domain walls. The discovery of DMI, another spin-orbit coupling phenomenon, induces a chirality in domain walls contributing to more stable domain wall motion. The discovery of the spin-hall effect introduces a new method of spin-injection contributing to more efficient torques to drive the domain wall motion. More work on nanowire devices have demonstrated the potential of tuning devices to optimize speed and current requirements [8–11]. Better understanding of the fundamentals of chiral magnetism and spin-orbit phenomena moves technology closer to the next generation of computer memory and logic.

1.2   Materials Exploration for Device Applications

Spin-orbit phenomena such as Heisenberg Exchange, Spin-Hall Effect, perpendicular magnetic anisotropy, and the DMI vary from material to material. In engineered magnetic multilayers, the interfaces between layers also have a significant effect on spin-orbit phenomena. For future technology, it is critical to understand how spin-orbit phenomena can be optimized to our benefit. One aspect of spin-orbit phenomena that is being explored is how they are exhibited in different material systems. For example, it has been shown in literature that sandwiching Co/Ni ferromagnetic layers between Pt layers results in a faster domain wall velocities. Further work on that topic has revealed that DMI and the Spin-Hall effect both vary with seedlayer composition. Significant work has been done to characterize the DMI properties of heavy metals such as platinum, gold, iridium, tungsten, and tantalum. Different heavy metals also show different Spin-Hall angles that determine their spin transport properties in a domain wall device. Many heavy metals and layer combinations remain unstudied and would be worth exploring. Advances in sputter deposition technology and device fabrication has made it easier to develop systems with ideal interfaces and structures used in the study of spin-orbit phenomena. It is now possible to deposit a wider range of materials to study using new combinatorial techniques. Further exploration of heavy metals will result in more possible routes of optimization for domain wall devices, making it an extremely important aspect of this thesis work.

1.3   Outline

Chapter 1 will introduce the necessary background information to frame this thesis work. The section will start with an introduction to general magnetism and magnetic domain walls. Spin-orbit phenomena that are relevant to chiral domain walls and the function of nanowire devices will also be introduced. **Chapter 2** will be an introduction of the various characterization techniques that have been used for this thesis work. The section is split into the three following sections: characterization techniques, thin film and nanowire device fabrication, thin film and nanowire device testing. **Chapter 3** covers the experimental evaluation of DMI in the Pt / $[Co/Ni]_2$ / Co / Ta magnetic multilayer. From experimental

findings, we are able to further our understanding of chiral domain walls and eventually construct two models that detail the driving force on bubble domain shape and the elastic mechanism for domain wall motion. In **Chapter 4**, the models developed previously are utilized effectively to characterize the link between seedlayer composition and interfacial DMI. We examine two different systems (Pt / Pt_xIr_{1-x} / $[Co/Ni]_2$ / Co / Ta and Pt / Pt_xAu_{1-x} / $[Co/Ni]_2$ / Co / Ta) using Kerr microscopy, and extract DMI magnitude and direction as a function of composition (x). In addition, the link between nanowire device performance and composition is also explored and and discussed. In **Chapter 5**, we explore the seedlayer and capping layer interfaces in our magnetic multilayers in greater detail. We elucidate the relative contribution of each interface (Pt/Co, Co/Pt, Co/Ir, Ni/Pt, Ni/Ir) to the effective DMI of the system and comment on its importance for engineering more efficient domain wall devices. Finally, **Chapter 6** summarizes the thesis work and sets the framework for future work on this topic.

1.4 Hypothesis

This thesis work will elaborate on the research conducted to support two main hypotheses:

(1) Interfacial DMI in a magnetic multilayer can be optimized via filmstack structure and layer engineering to achieve DMI magnitudes larger than values found in pure Heavy Metal/Ferromagnet interfaces.

(2) Current-driven domain wall motion in magnetic multilayers is directly correlated with DMI and any changes in DMI will be reflected in the performance of domain wall devices.

Background

In order to discuss our efforts in exploring next generation magnetic materials, it is necessary to go into more detail about the fundamental concepts of magnetism. The following sections briefly discuss the fundamentals of conventional ferromagnetism, chiral magnetism, and transport phenomenon relevant for understanding the behavior of magnetic domain walls for spintronics applications. Further advancements and understanding in these areas are necessary for implementation of stable, high performance, energy efficient devices.

2.1 Spin-Orbit Coupling in Magnetic Materials

The physical origin of magnetism and magnetic systems, like most physical phenomena, are the intrinsic quantum properties of elementary particles. More specifically, magnetism is a manifestation of the intrinsic spin angular momentum ($\vec{S}$) of an electron and its angular momentum ($\vec{L}$) around a nucleus, which gives rise to a magnetic moment. The generated magnetic moment due to spin is described by the following equation, which defines a constant known as the Bohr Magneton [12]:

$$\vec{\mu} = g_s \frac{-e}{2m_e} \vec{S} = \frac{-e\hbar}{2m_e} = \vec{\mu}_B \tag{2.1}$$

$$g_s = 2 \tag{2.2}$$

$$\vec{S} = \frac{\hbar}{2} \tag{2.3}$$

where e is the elementary charge of an electron, $\hbar$ is the Planck constant, m_e is the elementary mass of an electron, g_s is the g-factor of an electron, and $\overrightarrow{S}$ is the quantized spin angular momentum of an electron. [12] When $\overrightarrow{L}$ and $\overrightarrow{S}$ are coupled, the effect is known as the spin-orbit interaction. Simply, the spin-orbit interaction is an effective magnetic field caused by an electrons orbiting motion interacting with its intrinsic spin magnetic moment described by the equation:

$$E_{SO} = \lambda \overrightarrow{S} \cdot \overrightarrow{L} \tag{2.4}$$

$$\lambda \propto Z^4 \tag{2.5}$$

with Z corresponding to atomic number. The Spin-Orbit coupling is strongest in heavy metals and responsible for perpendicular magnetic anisotropy, the Spin-Hall Effect, and the Dzyaloshinskii-Moriya Interaction. They are critical for spintronic applications and they are the main phenonmena explored in this thesis work.

2.1.1 Heisenberg Exchange

The work of this thesis is primarily concerned with the properties of ferromagnetic materials, a class of materials that have a nonzero magnetic moment without the application of an external field. Common ferromagnetic materials such as Fe, Co, and Ni are used ubiquitously for many applications today. The origin of their magnetic moment comes from a nonzero net spin angular momentum ($\overrightarrow{S}$) per unit volume in a material. Applying Hund's Rules to different transition metals demonstrates that the nonzero spin angular momentum is the result of incomplete electron orbitals for each element. The magnetic moment (Bohr Magneton) originating from each unpaired electron spin gives the material a net magnetic moment. However, this phenomenon does not fully explain the relative magnitude of a ferromagnet when compared to the magnitude of the Bohr Magneton. Ferromagnetic materials demonstrate magnetic moments that are many orders of magnitude smaller than expected, which Pierre Weiss attempted to explain using his *Molecular Field Theory*. Essentially, the presence of an internal molecular field in a material acted as a force to align

individual magnetic moments in parallel, resulting in spontaneous magnetization of a material that would otherwise be too strong to align. From empirical calculations, the magnitude of the molecular field was shown to match the magnitude of the magnetization measured in ferromagnetic materials. This theory was later expanded by Werner Heisenberg when he showed that the physical origin of the molecular field was the result of a phenomenon called *Exchange Coupling*. The Heisenberg exchange interaction is a quantum mechanical phenomenon that aligns neighboring electron magnetic moments to be parallel to each other. Unlike a dipole-dipole interaction, the exchange interaction is short range and much stronger. At the small length scales between atoms, the Heisenberg exchange dominates and its energy is given by the equation:

$$E_{ex} = -2J_{ij}(\overrightarrow{S}_i \cdot \overrightarrow{S}_j) \tag{2.6}$$

where J is the exchange integral and $\overrightarrow{S}$ are the spin angular momentum of neighboring spins.

The effective field from the Heisenberg exchange is of the same order of magnitude as the empirically derived molecular field. Due to the non-localized nature of the conduction electrons in the $3d$ orbitals of transition metals, the Pauli Exclusion Principle affects the Heisenberg exchange coupling between individual atoms in a material. In this model, the atomic orbitals between neighboring atoms overlap to some degree. Depending on the interatomic distance, the exchange interaction aligns neighboring spins to be parallel(ferromagnetic) or antiparallel(antiferromagnetic). When the interatomic distance is large(small), there is less(more) overlap in their electron orbits. The electron spins are aligned by the Heisenberg Exchange interaction to satisfy the Pauli Exclusion Principle accordingly, as seen in Fig. 2.1. The Bethe-Slater curve shows how the exchange integral in transition metals is affected by the inter atomic distances of individual materials, explaining the trend from antiferromagnetic exchange to ferromagnetic exchange across the periodic table. If the scalar J is negative, the energy term is minimized when the spins are in an anti-parallel configuration. However, if the scalar J is positive, the energy term is minimized when the spins are parallel [13]. Generally, if the distance between neighboring atoms is small, the Pauli
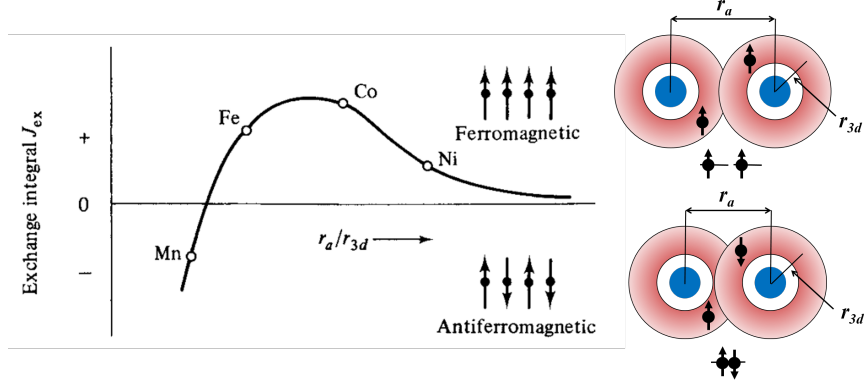
Figure 2.1: Interatomic exchange coupling in transition metals described by the Bethe-Slater Curve. [14]

Exclusion Principle determines that the antiparallel configuration is energetically favorable, resulting in a negative J (Fig. 2.2a). Positive J corresponds to a system with neighboring atoms that are farther apart, making the parallel configuration more favorable. Although there are some exceptions, the relationship between atomic spacing and exchange energy for different transition metals is mapped by this Bethe-Slater Curve.

2.1.2 Dzyaloshinskii-Moriya Interaction

The Heisenberg Exchange interaction determines the magnetic configuration of bulk materials. More specifically, exchange interactions are responsible for aligning individual magnetic spins in energetically favorable orientations giving rise to ferromagnetic, antiferromagnetic, and ferrimagnetic materials. In addition to the Heisenberg exchange, an additional exchange interaction called the Dzyaloshinskii-Moriya Interaction, or the anti-symmetric exchange, was discovered relatively recently. The total exchange energy of a system can be described by the exchange Hamiltonian, divided into the contributing exchange interaction terms [15, 16]:

$$H = H_{ex} + H_{DMI} \tag{2.7}$$

$$H = -\sum_{i \neq j} J_{ij} \vec{S}_i \vec{S}_j - \sum_{i \neq j} \vec{D}_{ij} \cdot (\vec{S}_i \times \vec{S}_j) \tag{2.8}$$

which describe isotropic exchange and anti-symmetric exchange, respectively. J_{ij} describes

Magnetism : Competing Spin-Orbit Interactions

Heisenberg Exchange

$$E_{ex} = -J \cdot \overrightarrow{S_1} \bullet \overrightarrow{S_2}$$

Antisymmetric Exchange (DMI)

$$E = -\overrightarrow{D} \cdot (\overrightarrow{S_1} \times \overrightarrow{S_2})$$

Energy minimized when
parallel/antiparallel
(ferromagnetic/antiferromagnetic)

Energy minimized when perpendicular
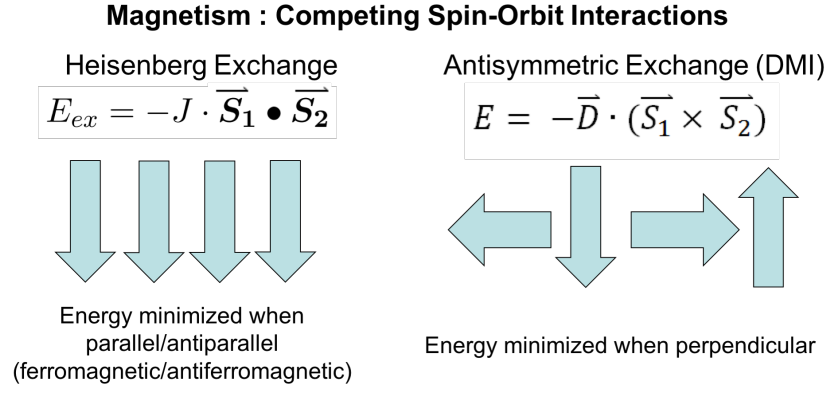
Figure 2.2: Heisenberg Exchange and Anti-Symmetric Exchange

the Heisenberg exchange coupling coefficient. D_{ij} describes the Dzyaloshinskii-Moriya vector. S_i and S_j describe two neighboring spins. Like the Heisenberg Exchange, the energy from DMI between two spins is given by a similar equation:

$$E_{DMI} = -\overrightarrow{D}_{ij}(\overrightarrow{S}_i \times \overrightarrow{S}_j) \tag{2.9}$$

The anti-symmetric exchange term represents the Dzyaloshinskii-Moriya Interaction (DMI), where D is the DMI vector [17]. In contrast to the Heisenberg Exchange term, the anti-symmetric exchange energy is minimized when neighboring spins are perpendicularly oriented (Fig. 2.2b). The sign of the DMI vector determines the direction of the canting, with a positive value favoring spins canted towards each other and a negative value favoring spins canted away from each other. The possible direction of the DMI vector is determined by Moriya's rules, after the work of Toru Moriya [18] in his work studying the symmetry of the interaction. He has shown in his work that a system with an inversion center show no anti-symmetric exchange contributions. Because of this symmetry restriction, bulk DMI has only been found in more exotic magnetic materials, such as FeGe. However, because of the reduction in symmetry near the surface, the DMI is enhanced at an interface. There has recently been more attention devoted to interfacial DMI because it has been induced in thin film materials fabricated to exhibit structural inversion asymmetry [19–21]. Magnetic thin films are shown to fulfill all Moriya rules and are able to exhibit antisymmetric exchange, theoretically. More specifically, having an asymmetric film stack removes the in-
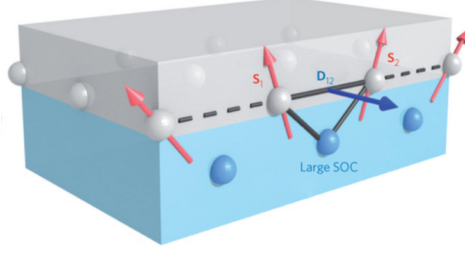
Figure 2.3: Spin canting and interfacial DMI induced by structural asymmetry [22]
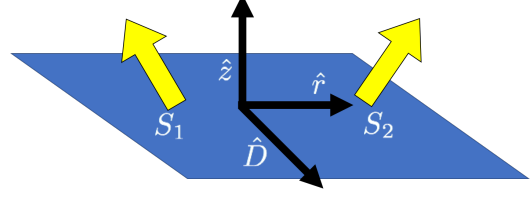
Figure 2.4: Interfacial DMI coordinate system

version center of the bulk material allowing for DMI at the interfaces. The only restriction for these induced DMI structures is that the layers have to be extremely thin because of the short-range nature of exchange interactions (Fig. 2.3). When interfacial DMI is introduced in a system, the Dzyaloshinskii-Moriya vector ($\overrightarrow{D}_{ij}$) is adjusted to account for the new geometry:

$$\overrightarrow{D}_{ij} = D_{int}(\overrightarrow{r} \times \overrightarrow{z}) \tag{2.10}$$

where D_{int} is a material dependent constant, $\overrightarrow{r}$ corresponds to the vector separating two neighboring spins, and $\overrightarrow{z}$ corresponds to the vector perpendicular to the film surface (Fig. 2.4). This interaction gives rise to unique spin textures and chiral domain walls, a important part of this thesis work to be discussed later in the document.

2.2 Static Magnetic Properties in Thin Films

In order to describe the magnetization, magnetic domain, and domain wall behaviors in a magnetic material, a more fundamental understanding of static magnetic energy is required. In the context of this work, this encompasses numerous effects from internal or external sources that can influence the total magnetic energy in a system. In the study of magnetic thin films, the magnetic effects of interest include energy from exchange interactions, magnetocrystalline anisotropy, shape anisotropy, dipole-dipole interactions, and Zeeman interactions. Understanding the role of all the magnetostatic effects becomes useful for describing complex magnetic behavior.

2.2.1 Magnetocrystalline Anisotropy

Magnetocrystalline anisotropy describes the difference in energy required to magnetize a material along different crystallographic orientations. This difference in energy is determined by the spin-orbit coupling in a material as well as the symmetry of the system. Those crystallographic directions are referred to as the material's *hard axis* or *easy axis*. When a system is magnetized along its *easy axis*, it requires less energy to reach its saturation magnetization, M_s, when all magnetic moments are oriented in the same direction. A relatively low external field is required to completely magnetize a system when it is oriented along the easy crystallographic direction. However, when the external field is oriented along the *hard axis*, more energy is expended to reach saturation. For example, plotting the magnetization of BCC Fe in response to applied external field will show that it takes a significantly larger external field to magnetize along the [111] *hard axis* compared to the [100] *easy axis*. In FCC Ni, the relationship is reversed, where the [111] direction corresponds to an *easy axis* and the [100] corresponds to a *hard axis*. The magnitude of the energy required to overcome the spin-orbit coupling and its preferred magnetic orientation, in a uniaxial system, can be described by the following equation:

$$E_{anisotropy} = K_1 sin^2\theta + K_2 sin^4\theta + K_3 sin^6\theta + ... \tag{2.11}$$

where K corresponds to material specific constants and θ corresponds to the angle between the systems easy axis and direction of magnetization.

2.2.2 Perpendicular Magnetic Anisotropy

In materials, magnetic anisotropy describes the dependence of energy on magnetic orientation. The main kinds of anisotropy are magnetocrystalline anisotropy, shape anisotropy, interfacial anisotropy, and magnetoelastic anisotropy. In our thin film systems, the magnetic anisotropy originates from the interface between Co/Ni and Pt/Co. Starting with (2.11) for describing uniaxial anisotropy in a magnetic system, the equation can be simplified by only considering the first term, resulting in the following equation:

$$E_{anisotropy} = K_{mc} \sin^2 \theta \tag{2.12}$$

Equation (2.12) describes the uniaxial anisotropy enery where K_{mc} encompasses all the magnetocrystalline anisotropy contributions and θ is the angle between the easy axis and the magnetization vector.

When materials are reduced to thin films, interfacial anisotropy is introduced to the system, adding another contribution to the anisotropy energy constant K:

$$K_{mc} = K_v + \frac{2K_s}{t} = 2\pi M_s^2 + \frac{2K_s}{t} \tag{2.13}$$

where K_v corresponds to volume anisotropy, K_s corresponds to interfacial anisotropy, and t is the film thickness. The latter contribution is what gives rise to perpendicular magnetic anisotropy in our films. When the interfacial anisotropy dominates over K_v, the magnetization easy axis is perpendicular to the film surface. When volume anisotropy dominates, the magnetization is in-plane. The effective anisotropy of a magnetic thin film has been shown to change linearly as a function of the magnetic layer thickness. A Co/Pd system, for example, has an out-of-plane easy axis for thin layers of magnetic Co. However, as the thickness of Co increases past a critical thickness, the preferred orientation lies in-plane. [23] This phenomenon has been observed in many thin film materials like [Co/Ni] multilayer systems [24].

2.2.3   Shape Anisotropy

Shape anisotropy describes the relationship between the physical shape of a system and its magnetization. Unlike magnetocrystalline anisotropy, where the direction of magnetization is determined by the strength of the spin-orbit coupling at the lattice structure, the shape anisotropy is related to the dipolar interactions in the system. Dipolar interactions, in the context of magnetism, describes a phenomenon where magnetic moments behave like point charges. The ends of a moment vector can be considered either "positive" or "negative". Similar to point charges, opposite charges tend to attract while like charges tend to repel.

Since dipolar interactions are long-range effects, the shape of the material influences its magnetization energy. Due to shape anisotropy, the magnetization prefers to lie along the long axis of an asymmetric shape, effectively giving the system an easy axis. In order to explain this phenomenon, it is necessary to introduce the idea of a demagnetization field. In a magnetic system, a self-generated field is induced in the direction opposite of its magnetization to reduce the total magnetic moment. This field is described by the equation:

$$H_d = -N_d M \tag{2.14}$$

where N_d describes a demagnetizing factor that is determined by shape. It can be shown that the short axis of an asymmetric shape results in s larger demagnetization factor (N_d), which means a larger demagnetizing field is generated when a sample is magnetized along its short axis. Therefore, it is energetically favorable to magnetize the system along the long axis, since a smaller demagnetizing field requires less energy to overcome. The energy for overcoming a demagnetizing field is given by the equation:

$$E_{shape} = -\frac{1}{2}\overrightarrow{H}_d \cdot \overrightarrow{M} \tag{2.15}$$

where $\overrightarrow{M}$ corresponds to the magnetization vector. The equation can be further reduced to:

$$E_{shape} = K_{shape} \sin^2 \theta \tag{2.16}$$

where K_{shape} is a constant that includes the effects demagnetization factors and the total magnetic moment and θ is the angle between the magnetization vector the system's easy axis. This equation assumes the following for in the case of magnetic thin films:

$$E_{shape} = \frac{1}{2}M_s{}^2 \sin^2 \theta \tag{2.17}$$

2.2.4   Zeeman Energy

The Zeeman Energy describes the energy contribution of any externally applied magnetic fields to the system. The energy can be described by the following equation:

$$E_{Zeeman} = -MH\cos\theta \tag{2.18}$$

After combining all the effects of the magnetostatic energy terms the simplified equation for the energy of the magnetic system becomes:

$$E_{total} = K_{eff}\sin^2\theta - MH\cos\theta \tag{2.19}$$

where K_{eff} is the effective anisotropy constant that includes all the contributions from anisotropy (magnetocrystalline, shape, interfacial) and θ is the angle between the magnetization vector and the easy axis. The field (H_k) required to magnetize thin film along its hard axis is related to its effective anisotropy (K_{eff}) and saturation magnetization (M_s), as given by the equation [14]:

$$\mu_0 H_k = \frac{2K_{eff}}{M_s} \tag{2.20}$$

Both of these relationships have been applied extensively in this thesis for the experimental characterization of magnetic properties and the modeling of chiral domain wall behavior.

2.3   Magnetic Domain Walls

2.3.1   Conventional Bloch Wall Properties

In ferromagnetic material, the interaction between all the magnetostatic energy terms results in the formation of magnetic domains and domain walls in an attempt to lower the total energy of the system. In a magnetic material, the magnetic anisotropy of the system attempts to lower energy by aligning all the individual spins along an easy axis. However, the demagnetizing energy will be at its largest in this configuration. In order to decrease the total energy, magnetic domains are formed to reduce the demagnetizing energy that would otherwise form in a single domain system, as seen in Fig. 2.5. The formation of a
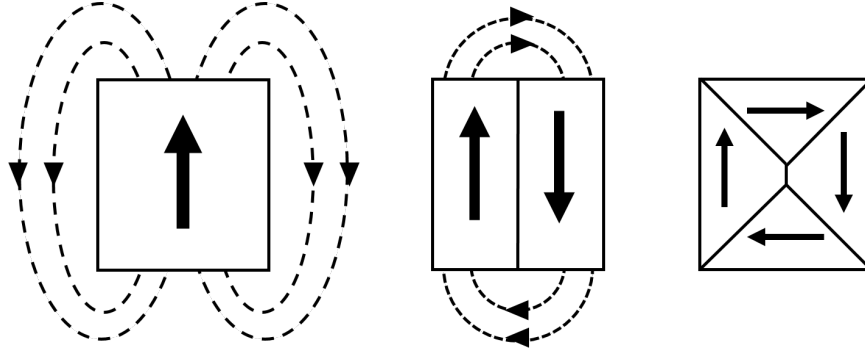
Figure 2.5: The transition from single domain state to multidomain configuration to lower the total energy in magnetic system.

magnetic domain introduces a region where magnetic spins transition from one orientation to the other. As expected, having a domain wall introduces an addtional energy term into the system because it works against the exchange interactions and the anisotropy energy. However, the reduction in demagnetizing energy makes this configuration much more favorable. Domain walls can can exist as a Néel wall or as a Bloch wall, depending on the physical characteristics of the magnetic system. A Bloch Wall describes a transition where intermediate spins rotate out of the plane and they align along the domain wall. The energy density of a Bloch wall transition is given by the following equation:

$$\sigma_{Bloch} = 4\sqrt{AK_{eff}} \qquad (2.21)$$

where exchange stiffness (A) corresponds to a constant related to the strength of the exchange interaction in the system. The domain wall width, or the length of the transition region is given by the equation:

$$\lambda_{Bloch} = \sqrt{\frac{A}{K_{eff}}} \qquad (2.22)$$

For lower dimensional materials like thin films, Néel walls energetically favorable. Néel walls describe a transition where the intermediate spins rotate in plane and they align perpendicularly to the domain wall (Fig. 2.6).

Figure 2.6: Ideal Bloch Wall and ideal Néel Wall Transitions.

2.3.2 Impact of DMI on Domain Walls

In a material that is uniformly magnetized, the Heisenberg Exchange dominates the system energetically and the antisymmetric exchange is unable to induce canting. However, at more localized domain walls, DMI has an effect on the equilibrium magnetization and energy on the spins. Domain walls are essentially boundaries between two magnetic domains (regions that contain uniformly oriented spins) pointing in different directions. Simply, a domain wall is a transition from one spin orientation to the next. The transition from one direction to another is determined by the competition between the isotropic symmetric exchange energy term (Heisenberg Exchange) and the anti-symmetric anisotropic energy term (DMI). This determines the most energetically favorable orientation for the spins to adopt during the transition. In thin films with no DMI and only symmetric exchange, it is energetically favorable to transition in the form of a Bloch wall because it lowers the demagnetizing field. In films with a Néel wall transition (Fig. 2.7), the direction of the DMI vector determines the direction of rotation, establishing chirality in the system. Essentially, all domain walls in the system are expected to maintain the same chirality. For a film with a negative DMI vector, it is energetically favorable to form a right-handed domain wall. A positive DMI vector results in a left-handed domain wall. As seen in Fig. 2.7, a right-handed domain wall transitions by rotating clockwise while a left-handed domain wall transitions by rotating counterclockwise for the same reference frame. Stable chiral domain walls have been examined using techniques like asymmetric domain wall motion, Brillouin light spectroscopy, Lorentz TEM, spin-polarized low-energy electron microscopy (SPLEEM), and NV Diamond Magnetometry [19, 20, 25–27]. The possibility of induced chirality in a magnetic system is a promising step forward for domain wall driven devices.
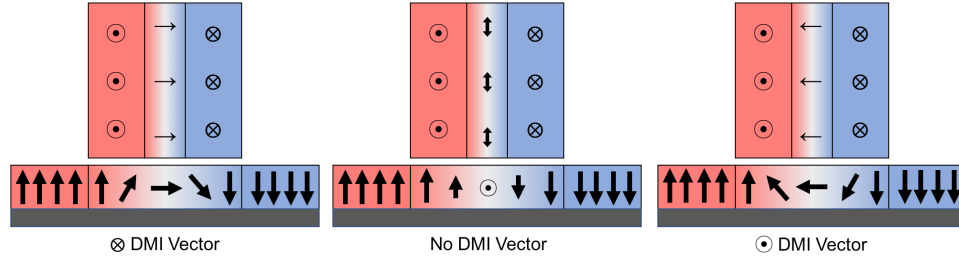
Figure 2.7: Top (top) and side (bottom) views of chiral domain walls. (1) DW Configuration with negative DMI, (2) DW Configuration with zero DMI, (3) DW Configuration with positive DMI

In particular, next generation computer memory and storage technologies will be able to incorporate stable exotic magnetic domain structures like skyrmions, helical phases, and chiral domain walls into their design. This work hopes to demonstrate the role of DMI induced chirality in fast, stable, and energy efficient domain wall motion for next generation technologies.

2.3.3   Chiral Domain Wall Energy

Magnetic properties of a system are used to characterize the energy which is relevant for characterizing the DMI. Properties relevant for our studies include effective uniaxial anisotropy (K_{eff}), domain wall width (λ), and domain wall energy density (σ_0). The effective magnetic anisotropy constant (K_{eff}) is derived in Chapter 2.2.2 and given by the equation:

$$K_{eff} = \frac{\mu_0 H_k M_s}{2} \tag{2.23}$$

The domain wall width can be calculated with the following equation:

$$\lambda = \sqrt{\frac{A}{K_{eff}}} \tag{2.24}$$

where A is the exchange stiffness constant. In this work, the exchange stiffness is assumed to be $A = 1 \times 10^{-11} J/m$. It is also common to see $A = 1.6 \times 10^{-11} J/m$ cited in similar studies. Finally, the Bloch domain wall energy density is given by the equation:

$$\sigma_0 = 4\sqrt{AK_{eff}} \tag{2.25}$$

The energy density of a chiral domain wall and the influence of DMI can be calculated by modifying Equation (2.25) into the following [28]:

$$\sigma_0 = 4\sqrt{AK_{eff}} - \pi|D| \tag{2.26}$$

where D is the DMI magnitude. Alternatively, in systems with DMI, the effects of DMI can also be accounted for by calculating the effective field generated by the DMI (H_{DMI}) and any external magnetic fields. In this case, the effective fields must overcome the energy given by Equation (2.27), transitioning a Bloch wall into a Néel Wall.

$$\mu_0 H_x + \mu_0 H_{DMI} > \frac{2K_D}{M_s} \tag{2.27}$$

The domain wall anisotropy constant K_D is used to characterize the energy difference between a Bloch wall and a Néel Wall and is given by the equation [29]:

$$K_D = \frac{\ln 2}{2\pi} \mu_0 M_s^2 \frac{t_f}{\lambda} \tag{2.28}$$

where t_f is the thickness of the magnetic layer. From Equations (2.27) and (2.28), the effective field from DMI required to transform the domain wall into a pure Néel is calculated. In a system with no external applied magnetic field, this also calculates the critical DMI required to form the pure Néel structure. For domain walls with DMI, these magnetic properties are necessary to calculate the total energy of the system using Equation (2.29) [30,31]. The energy is a function of Bloch Wall energy, domain wall anisotropy energy, and the Zeeman energy from the effective fields. In Chapter 4.4, we explore the energetics of chiral domain walls in more detail.

$$\sigma_{DW}(H_x) = \sigma_0 + 2K_D\lambda - \pi\lambda M_s|\mu_0 H_x + \mu_0 H_{DMI}| \tag{2.29}$$

2.4   Field Driven Domain Wall Motion

While the magentostatic energy terms are useful in predicting the energy landscape of magnetic systems, they are not as useful in understanding their dynamics. To understand
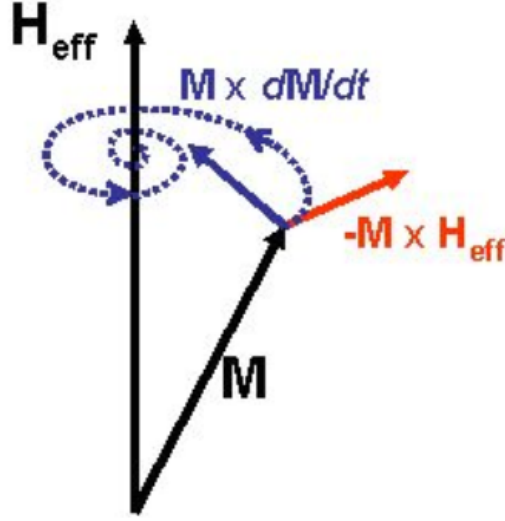
Figure 2.8: Diagram of the precession (red) and damping (blue) terms of the LLG equation.

how individual magnetic moments respond to external forces, the Landau-Lifshitz-Gilbert Equation is used to model their behaviors micromagnetically and is given by the equation:

$$\frac{\partial \overrightarrow{M}}{\partial dt} = -\gamma \overrightarrow{M} \times \overrightarrow{H}_{eff} + \frac{\alpha}{M} \overrightarrow{M} \times \frac{\partial \overrightarrow{M}}{\partial t} \tag{2.30}$$

where $\overrightarrow{M}$ is the magnetization vector, γ is the gyromagnetic ratio, μ_B is the Bohr magneton, α is the Gilbert damping constant, and g is the Lande g-factor. $\overrightarrow{H}_{eff}$ is the effective field determined by an external magnetic field, dipole field, anisotropy field, and exchange stiffness. The terms that make up the equation reflect the processes that occur when a magnetic moment switches, causing a change in orientation, as seen in Fig. 2.8. The first term describes the tendency for a magnetic moment to precess around the effective field. In the absence of energy disappation, the magnetic moment is expected to precess indefinitely. In reality, however, there is a loss of energy described by the damping term of the LLG equation, where the magnetic moment eventually aligns with the effective field. In domain wall dynamics, the LLG is important to consider in order to understand the propagation of domain walls through a material. The LLG relationship shows that when an external field is applied, a torque is produced to facilitate magnetization switching.
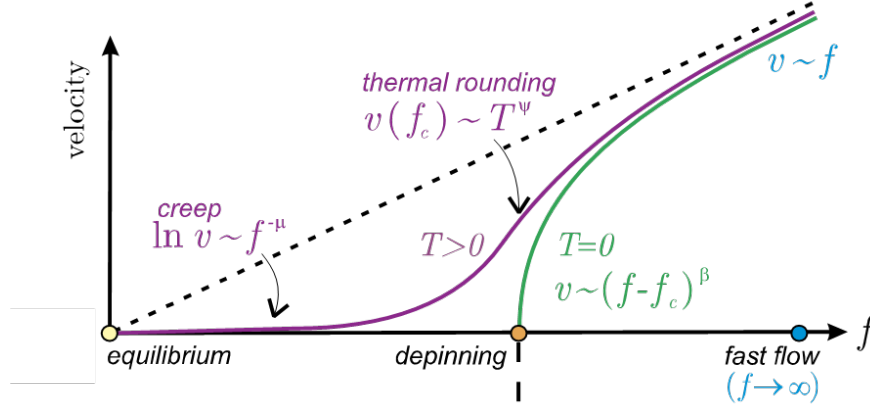
Figure 2.9: Plot of domain wall velocty as a function of the driving force (applied field), depicting the three regimes of domain wall motion [32].

2.4.1 Domain Wall Motion in the Creep Regime

Domain wall motion can primarily be classified into the two categories: the creep regime and the flow regime, as seen in Fig. 2.9 [32,33]. In the creep regime, the applied field is not sufficient to overcome the intrinsic pinning in a magnetic thin film caused by defects. The domain wall motion that occurs in this regime mainly comes from thermal fluctuations that allow the domain wall to reorient and reach metastable states. In this regime, the velocity is exponentially dependent on the driving force (applied field). At the film level studies of this thesis work, the field driven domain wall velocity will be evaluated as creep velocity.

2.4.2 Field Driven Domain Wall Velocity

Analyzing field driven domain wall velocity is the main approach to characterizing DMI in our systems. The mechanism for domain wall motion in a perpendicularly magnetized thin film is described by an Arrhenius (exponential) relationship given by (2.31).

$$v_{DW} = v_0 exp(-\alpha H_z^{-1/4}) \tag{2.31}$$

where H_z is the applied perpendicular field, v_0 is the characteristic velocity fitting parameter, and α is a parameter determined by the domain wall energy (Equation (2.29)). In Chapter 4.5, we will describe domain wall creep in more detail. We now turn our attention to discuss asymmetric growth in a bubble domain in order to show how domain wall creep

velocity is affected by domain wall energy.

The presence of interfacial DMI forces a domain wall to adopt a chirality in order to be energetically stable. The direction of the domain wall is then fixed around a nucleated bubble domain, as seen in Fig. 2.10. An applied in-plane field ($\mu_0 H_x$) is parallel to one side of the bubble and anti-parallel to the other. This configuration creates an anisotropic energy in the domain wall. In the absence of an external in-plane field, an applied perpendicular field creates an isotropic driving force for domain wall growth, as seen in Equation (2.29). However, because of the factor $|H_x + H_{DMI}|$, the difference in domain wall energy forces the wall to grow anisotropically [29, 30]. Because of the anisotropic domain wall energy, bubble domain growth is expected to exhibit asymmetric domain wall growth, as seen in Fig. 2.11. When the domain wall (H_{DMI}) and the external field (H_x) are parallel, the domain wall energy is lowered. However, when the domain wall and external field are anti-parallel, the domain wall energy is higher than in the parallel case. Therefore, one side is expected to grow much faster than the other. According to Equation (2.29), the domain wall energy is at its highest when H_{DMI} is the same magnitude as H_x and in the opposite direction. Therefore, it should result in a minimum domain wall velocity. The expected velocity curve is basically a isotropic domain wall velocity curve shifted along the x-axis as a result of the addition of anisotropic DMI energy (Fig. 2.11). Working backwards from the velocity behavior, one can determine the magnitude of the magnetic field generated by the DMI (H_{DMI}). When H_{DMI} is determined, the magnitude of the DMI vector (D) can be determined by the equation [29, 34]:

$$D = \mu_0 H_{DMI} M_s \lambda \tag{2.32}$$

In practice, however, the creep velocity behavior is much harder to predict. When combined with an external field ($\mu_0 H_x$), the domain wall energy of the bubble becomes highly anisotropic and elastic. This results in velocity profile features that cannot be explained by the conventional creep law. In Chapter 4.5, we will address those inconsistencies in greater detail.
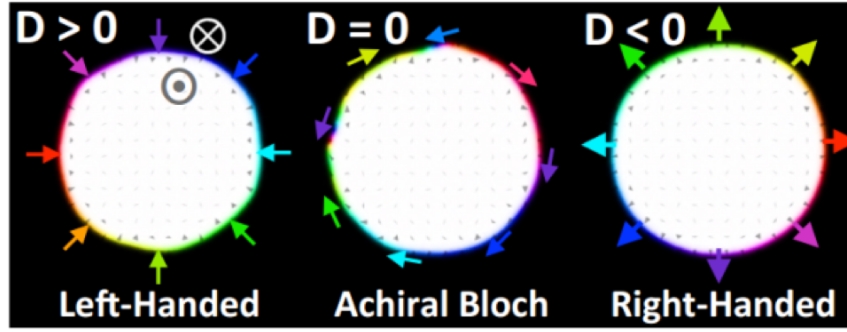
Figure 2.10: Chiral domain bubbles and direction of domain walls.
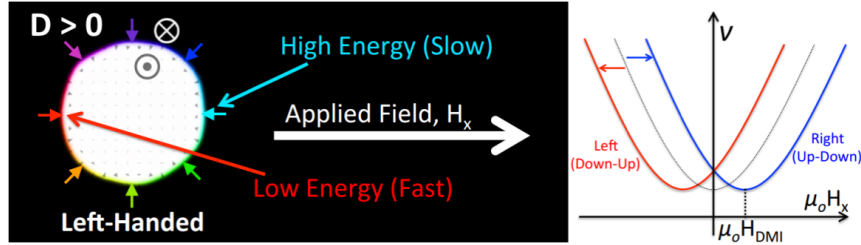
Figure 2.11: Asymmetric growth as resulting from anisotropic domain wall energy.

2.5 Current Driven Domain Wall Motion

2.5.1 Domain Wall Motion in the Flow Regime

Moving from film level characterization to device level characterization, our experimental results show that the current driven domain wall motion in devices is magnitudes higher than the field driven domain wall motion. This observation suggests that the velocity is transitioning from the creep regime, closer to the flow regime. As seen in Fig. 2.9, increasing the magnitude of the driving force past the critical unpinning field, drives the domain wall velocity into the flow regime. In the flow regime, the applied field overcomes the elastic energy and the pinning potential allowing the domain wall to effectively ignore the intrinsic film properties. As the result, the domain walls move with a steady-state velocity that approaches a linear relationship with the driving force, independent on the distribution of pinning potentials in the system.

2.5.2 Spin-Transfer Torque

The mechanism for moving domain walls through a magnetic material is the Spin-Transfer (Slonczewski) Torque (STT) [35]. The main principle behind STT is the conservation of

angular momentum as electrons travel through a medium. Spin-valves and magnetic tunnel junctions are common examples of devices that use STT in their operation. Conventionally, the device will have a fixed and a free magnetic layer. The fixed layer generates a spin-polarized current as discussed in the previous section. The spin-polarized electrons interact with the magnetic moments in the free layer as they pass through, imparting angular momentum. Collectively, the angular momentum is enough to switch the direction of magnetization in the free layer. Fig. 2.12 shows the principle behind STT devices. Spin-transfer torque is described by the Landau-Liftshitz-Gilbert-Slonczewski (LLGS) equation [36, 37]:

$$\frac{\partial \vec{M}}{\partial dt} = -\gamma \vec{M} \times \vec{H}_{eff} + \frac{\alpha}{M} \vec{M} \times \frac{\partial \vec{M}}{\partial t} + \tau \tag{2.33}$$

where γ is the gyromagnetic ratio, and α is a damping constant. The modified equation describes the micromagnetic behavior of a magnetic spin as it interacts with external fields and includes the effects of spin transfer torque. τ is a collective term that corresponds to spin-transfer torque in the system. The first term describes the precessing behavior of a magnetic spin about an external field. This is essentially the behavior of a spin as it approaches equilibrium. The damping term of the LLGS equation describes a torque that drives the spin towards equilibrium. The third term of is the Spin-Transfer torque which describes the torque experienced by the magnetic spin as the system conserves angular momentum. STT (or Slonczewski Torque) is given by the equation [36]:

$$\tau_s = -\frac{\gamma \hbar}{2eM_sV} m \times (m \times I_s) \tag{2.34}$$

where M_s and V are the saturation magnetization and the volume of the magnetic material, respectively. I_s corresponds to the spin current applied to the system. Fig. 2.13 is a representation of the LLGS equation and the net torque that occurs as a result as the competition between the damping torque and the spin transfer torque. The interaction between the three terms can result in the spin aligning with the effective magnetic field, or the stable precession of the spin about the effective field, or the switching of the magnetic spin, depending on which of the three terms dominate. In the case of spintronic devices, the direction of the behavior depends on the direction of current. Increasing the current magni-
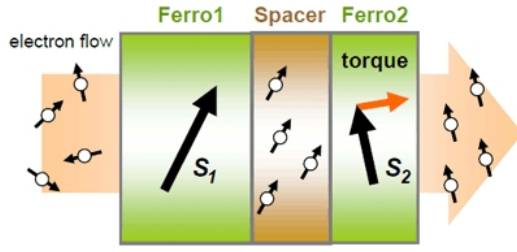
Figure 2.12: Schematic of a spin valve demonstrating spin filtering through spin-transfer torque. [38]
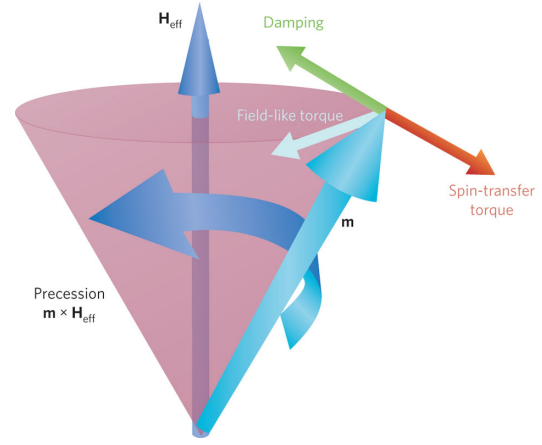
Figure 2.13: Magnetization dynamics illustrated by the Landau-Liftshitz-Gilbert-Slonczewski (LLGS) equation. [36]
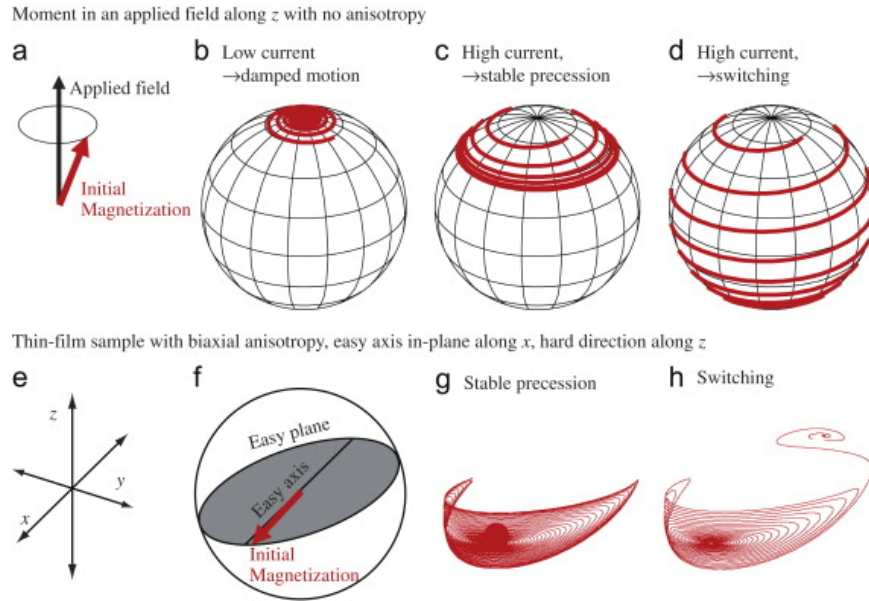
Figure 2.14: LLGS simulated dynamics of a magnetic moment as a function of current. [37]

tude takes the magnetic spins through the three states, and eventually switching (Fig. 2.14).

The possibility of applying STT in non-uniformly magnetized materials to move domain walls was first theorized by Luc Berger in the 1970s [39–41]. Understanding of current induced domain wall motion will be an important topic discussed in this study. As seen in Fig. 2.15, spin-polarized electrons traveling through a magnetic material will exert a torque on the individual magnetic moments that they travel past in order to converse angular momentum. Collectively, the torques exerted on the non-uniform magnetic moments force
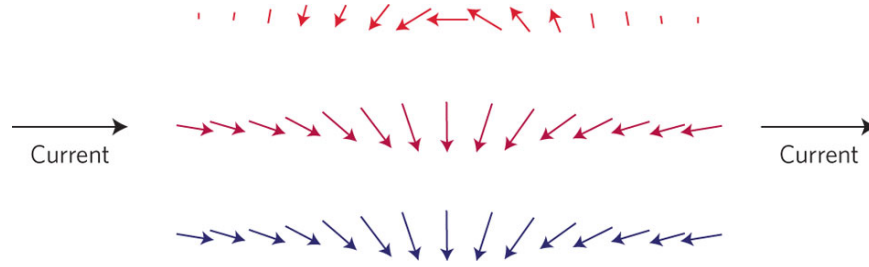
Figure 2.15: (1) Blue arrows represent the magnetization through a ferromagnetic material. (2) The red arrows illustrate the change in electron spin as it travels through the material and interacts with magnetic moments. (3) The orange arrows illustrate the torque transferred from the electron spins to the magnetic moments. [36]

a shift in the domain wall, moving it in the direction of the current. A single spin is shown to change directions as it interacts with the non-uniform magnetic moments. In order to conserve angular momentum, the spin must then exert a torque on each magnetic spin it passes. Finally, the torques will rotate the spins in a way that shifts the whole orientation one place to the right, including the domain wall (vertical magnetic moment). Domain walls will theoretically move when the critical current density [36] is applied.

2.5.3   Spin-Hall Effect

The following sections will be devoted to the background needed to understand another mechanism proposed for spintronic device operation, applying torque through the Spin-Hall Effect. While conventional electronics are powered by the charge of carriers, spintronic devices incorporate the spin of the carriers as well. From a quantum mechanical understanding of spin, electrons may only occupy one of two possible states ($+\frac{n}{2}$ or $-\frac{n}{2}$) described by the quantum number, s. Therefore, in a material with valence electrons, like transition metals, an applied current would transport both spin-up and spin-down configurations at an equal rate. However, functional spintronic devices require some way to generate a pure spin current, where one spin orientation is filtered resulting in a current with a uniform spin configuration (spin-polarized). Spin-polarization is the ratio between spin-up and spin-down electrons described by the following equation:

$$P = \frac{N_\uparrow(E_F) - N_\downarrow(E_F)}{N_\uparrow(E_F) + N_\downarrow(E_F)} \tag{2.35}$$

where $N(E_F)$ is described as the number of states (spin-up or spin-down) at the Fermi En-
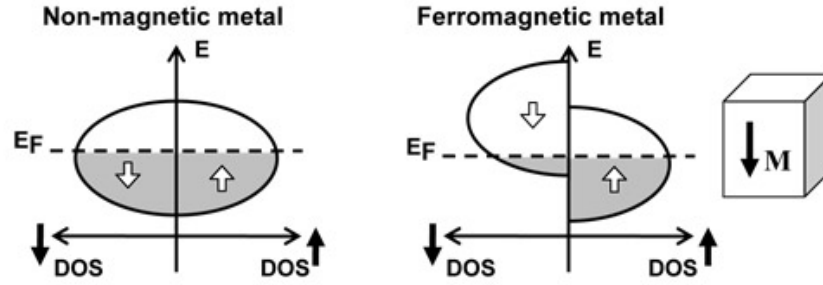
Figure 2.16: Spin-up and spin-down DOS of (1) a non-magnetic material and (2) a ferromagnetic material. [42]

ergy. Conventionally, a spin-current is polarized by passing current through a ferromagnetic material, as seen in GMR and TMR devices. The ferromagnetic material would filter out the minority spin electrons and allow majority electrons to pass through as a result of the different DOS (Fig. 2.16), which can be used to generate conventional Spin-Transfer Torque (STT).

For this study, the Spin-Hall Effect (SHE), a different method of spin-polarization is used for the same effect. The SHE is analogous to the Hall Effect and is similar in effect. The Hall Effect describes a phenomenon where a charge carrier moving through a metal experiences a Lorentz Force as a result of its charge and an external magnetic field. The force changes the direction of the traveling charge carrier and forces them to aggregate on one side of the metal. In the case of a current through a metal, the electrons are aggregated on one side creating a voltage differential perpendicular to the direction of the current. In the spin-dependent Hall effects, particles are segregated by their spin orientation rather than charge when they experience a Lorentz Force [43,44] (Fig. 2.17). The resulting transverse, polarized spin current is analogous to the voltage difference generated by the classical Hall Effect. The effect is somewhat analogous to the Magnus Effect, where a particle particles direction of travel gains a transverse component due to its angular momentum. The Anomalous Hall Effect describes the phenomenon of spin polarization in a ferromagnetic material (FM) where the Lorentz Force is the result of an internal magnetization. The SHE describes the same phenomenon of spin polarization in nonmagnetic materials. The pure spin current density ($\frac{\hbar J_s}{2e}$) that results from the SHE is described by the equation [45]:
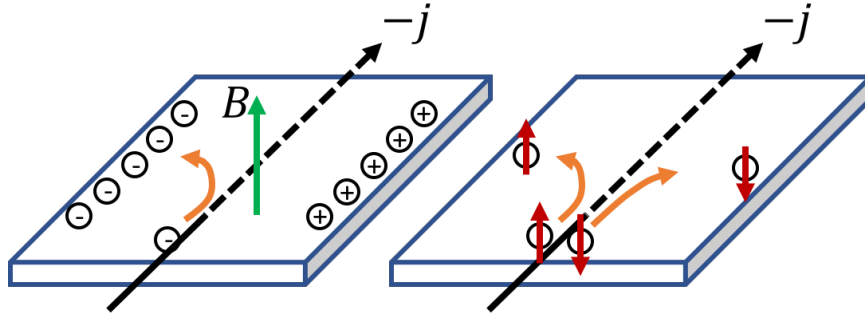
Figure 2.17: (1) Conventional Hall Effect (2) Spin-Hall Effect

$$J_s = \Theta_{sh}(\hat{\sigma} \times J_c) \tag{2.36}$$

where Θ_{sh}, J_c, and σ are the Spin-Hall Angle, charge current density, and spin moment respectively. The Spin-Hall Angle is a material property that describes the conversion efficiency from the charge current into a spin current and is described by the equation [45]:

$$\Theta_{sh} = \frac{|J_s|}{|J_c|} \tag{2.37}$$

Like DMI, the SHE is related to the magnitude of the spin-orbit interaction. The spin-orbit coupling effect is stronger for heavy (high Z) transition elements (Pt, Ta, Au, etc) and they are incorporated into the design of magnetic multilayers to facilitate spin-polarization in nanowires for current induced domain wall motion. However, different heavy metal layers are shown to move domain walls in opposite directions depending on its Spin-Hall Angle. As a result, the Spin-Hall Angles of different elements is a topic that is currently under heavy debate. The potential for the SHE to be a ubiquitous method for polarized spin transfer has generated a lot of interest in the field of spintronics. Multiple studies have been conducted on magnetic thin films to characterize the Spin-Hall Angle of different transition metals and different thin film compositions.

2.5.4 Spin-Transfer Torque and the Spin-Hall Effect in Magnetic Nanowire Devices

Recently, there has been a lot of attention on combining the Spin-Transfer Torque generated by the Spin-Hall Effect with chiral domain walls as a new method for inducing domain wall
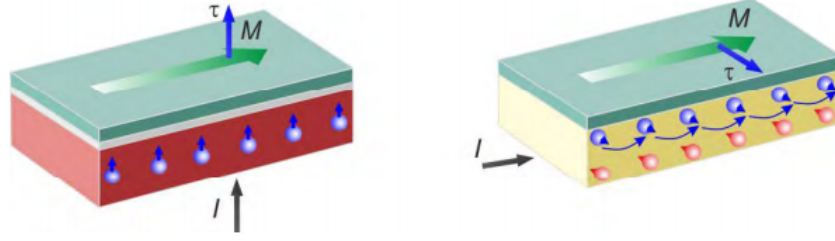
Figure 2.18: (1) Spin-Transfer Torque from spin filtering. (2) Spin-Transfer Torque from the Spin-Hall Effect [46]

motion [10, 11, 34, 47, 48]. The main advantage of the technique is the potential for less damage because the magnetic material itself is not exposed to the current. Instead of applying a current through the ferromagnetic material, the current is applied to a heavy metal under-layer (Fig. 2.18). Practically, the applied current flows through both layers resulting in some conventional STT applied to the system. However, the difference in resistances between the FM and HM layers directs the current through the underlayer, in theory. The principles of the SHE will spin-polarize the current and apply STT through the interface between the two layers. The resulting torque is proportional to the current density and the spin-hall angle. In contrast, the torque produced conventionally is proportional to the current density and the current polarization. The new method of spin injection requires modification to the spin-transfer torque component of the LLGS equation (Equation (2.34)). The modified torque term becomes:

$$\tau_s = -\frac{\hbar J_{NM}\Theta_{SH}}{2eM_s t_{FM}}\hat{m} \times (\hat{m} \times \hat{\sigma}) \tag{2.38}$$

where J_{NM} is the current density in the non-magnetic material, Θ_{SH} is the spin-hall angle, t_{FM} is the thickness of the ferromagnetic material, $\hat{m}$ is the magnetization direction, and $\hat{\sigma}$ is the direction of current polarization. Like the conventional technique, generated Slonczewski torque is shown to be effective in inducing domain wall motion [34]. The domain wall velocity is then proportional to the relationship:

$$v \propto \frac{H_{DMI}\Theta_{SH}}{H_k M_s t} \tag{2.39}$$
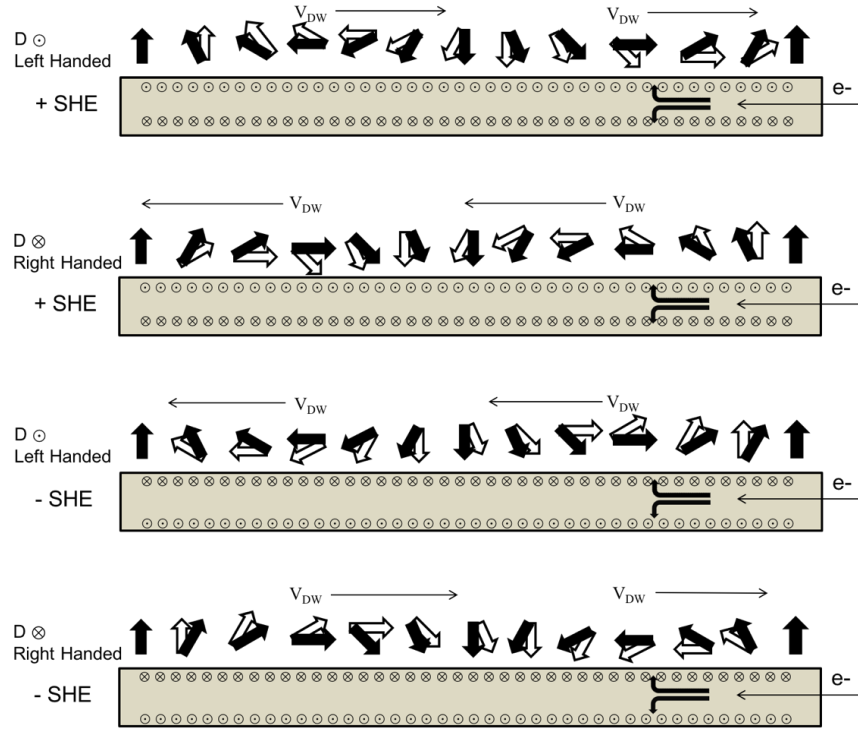
Figure 2.19: Possible combinations of spin-hall angle and chirality. Black arrows correspond to original spin orientation. White arrows correspond to spin orientation after spin-transfer torque.

where t is the thickness of the ferromagnetic layer. Interestingly, the fact that different materials have different spin-hall angles results in an additional advantage that the SHE technique has over the conventional technique. It has been shown, that materials with spin-hall angles in different directions will induce domain wall motion in opposite directions [34,47,49]. Unlike the conventional technique, which restricted the direction of domain wall motion in the direction of current, the underlayer selection determine the behavior of the domain wall. In combination with the chirality (DMI induced) of the magnetic material, the domain wall will either move in/opposite the direction of current. The figures Fig. 2.19 and Fig. 2.20 help visualize this phenomenon and summarize the possible outcomes from different combinations of DMI and spin-hall angle. Along with DMI, the ability to tune the SHE and STT theoretical energy efficiency make it a promising candidate for domain wall propagation and is a subject of interest in the spintronic community.

	Positive Spin Hall Effect	Negative Spin Hall Effect
Positive DMI Vector (Left-Handed)	With Current (Against e- flow)	Against Current (With e- flow)
Negative DMI Vector (Right-Handed)	Against Current (With e- flow)	With Current (Against e- flow)

Figure 2.20: Table summarizing spin-hall angle, chirality combinations, and resulting domain wall motion direction.

<div align="center">

CHAPTER III

</div>

<div align="center">

Experimental Methods

</div>

Here we elaborate on the techniques and methodology used produce and characterize magnetic thin film samples and magnetic domain wall devices. Background information relevant to the study is also included for each technique.

3.1 Characterization Techniques

3.1.1 Magneto-Optical Kerr Effect Microscopy (MOKE)

Kerr microscopy is a technique used to visualize the magnetic domain structure in a material (Fig. 3.1). A thin film is mounted onto the sample stage of an optical microscope with Magneto-Optical Kerr Effect capabilities. The microscope is also outfitted with a perpendicular and in-plane magnetic field generator to observe the effect of an external magnetic field on domain wall motion. In addition, the setup can be modified with electrical current probes in order to characterize current driven domain wall motion. The Magneto-Optical Kerr Effect describes the change in polarization and intensity when optical light is reflected from a magnetic surface (Fig. 3.2). The effect is described by generalized dielectric permittivity tensor [50]:

$$\boldsymbol{\varepsilon} = \varepsilon \begin{bmatrix} 1 & -iQ_v m_z & iQ_v m_y \\ iQ_v m_z & 1 & -iQ_v m_x \\ -iQ_v m_y & iQ_v m_x & 1 \end{bmatrix}$$

where m is the magnetization vector contribution of the sample, ε is the dielectric constant, and Q_v is the Voight material property that describes the strength of the Kerr Effect. The

<div align="center">

31

</div>
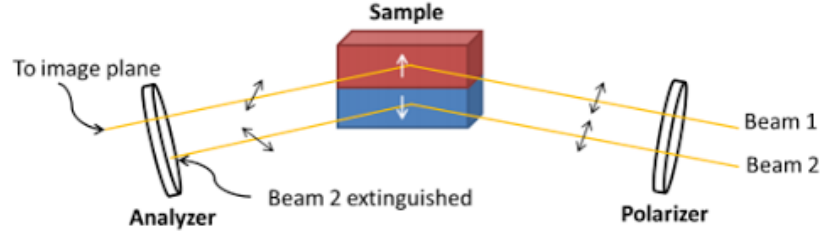
Figure 3.1: Basic operational principles behind Magneto-Optical Kerr Effect Microscopy

Kerr effect is given by the off-diagonal components of the tensor. It demonstrates that permittivity of a material is anisotropic, meaning the different magnetization contributions causes fluctuations in the phase of incident polarized light after reflection. The differences in the phase of reflected light is the key to differentiating between different magnetic domains in the sample. The change in polarization due to the Magneto-Optical Kerr effect can given by the equation [51]:

$$\phi_K = \theta_K + i\varepsilon_K \tag{3.1}$$

where θ_K is the Kerr rotation, and $varepsilon_K$ can be obtained from the dielectric permittivity tensor. The polar magneto-optical Kerr effect is used for characterization because it is used to detect magnetization that points along the surface normal. The polar mode is ideal for testing materials with perpendicular magnetic anisotropy (PMA), where the easy axis of a material points along the surface normal. A Lorentz force between the magnetization and electromagnetic wave, which is proportional to $(m \times E)$, generates a Kerr amplitude perpendicular to the incident light causing a rotation in polarization as shown in Fig. 3.2. Opposite magnetizations result in a Lorentz force that points in the opposing directions providing the contrast to visualize the domains in the thin film and nanowire samples. Incident light with a certain polarization is directed at the surface of a magnetic thin film at an angle given by v_0. In the case of the polar configuration, the incident light is perpendicular to the sample normal. When the light is reflected, the polarization is shifted away from the original orientation (R_N) by an amplitude of R_K, or the Kerr amplitude. The contrast is created when an analyzer on the Kerr Microscope is adjusted to filter out the signal for a polarization rotation in one direction while allowing the other. Fig. 3.3 shows a typical

polarizer/analyzer setup for the Kerr microscope. The signal of the resulting Kerr signal amplitude as it is detected by the analyzer is given by the equation:

$$A_{tot} = -R_p \cos \Psi_p \sin \alpha_s + R_s \sin \Psi_p \cos \alpha_s + R_K^{pol} \cos \left(\alpha_s - \Phi_p\right) m_{pol} \qquad (3.2)$$

where Φ is the set angle of the polarizer, α is the set angle of the analyzer, R_p and R_s are optical constants from the reflection of light, R_K^{pol} is the Kerr amplitude from the polar contribution, and m is the magnetization of the sample [50]. Other terms that account for the transverse and longitudinal Kerr setups were ignored. By adjusting the orientations of the polarizer and analyzer, the signal amplitude from a thin film sample can be enhanced. Equation (3.2) can be written in the form:

$$A_{tot} = A_N \pm A_K \qquad (3.3)$$

where A_N corresponds to the terms for the optical reflection and A_K corresponds to the term for the Kerr amplitude. The Kerr rotation, described in Equation (3.1), is calculated from the relationship:

$$\theta_K = \frac{A_K}{A_N} \qquad (3.4)$$

By setting the analyzer to the same orientation as the Kerr rotation, the signal from that particular magnetic domain is effectively extinguished, while a domain in the opposite orientation becomes more visible from the contrast.

Kerr Microscopy technique is an optical technique and is limited by its inability to extract domain configurations for the interior of sample. This means that the technique is mainly useful for characterizing the domain configuration from the surface down to $\sim 10nm$. The resolution is limited to domains larger than $0.15\mu m$, corresponding to an optical resolution of $\sim 0.3\mu m$ [50]. Nevertheless, Kerr Microscopy will be the main technique used to image domains and characterize effects of DMI on domain wall behavior because magnetization can be observed directly and easily without changing the moments or damaging the sample.
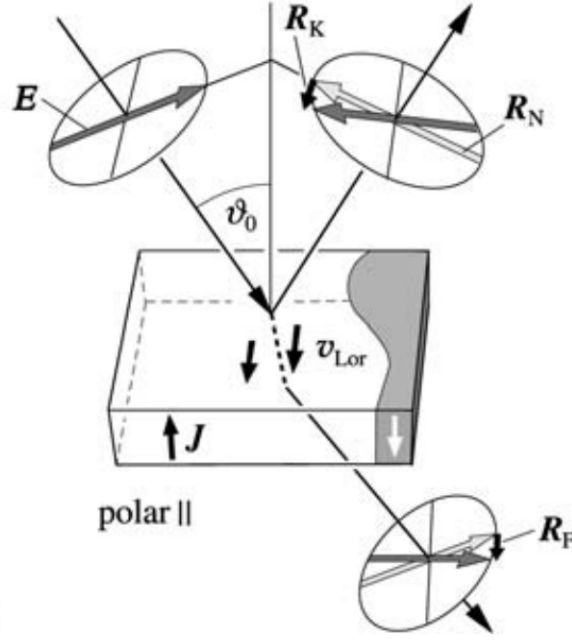
Figure 3.2: Physics of Polar Magneto-Optical Kerr Effect (R_K). The Faraday Effect causes a similar change in polarization (R_F) when light is transmitted through the sample. [50]
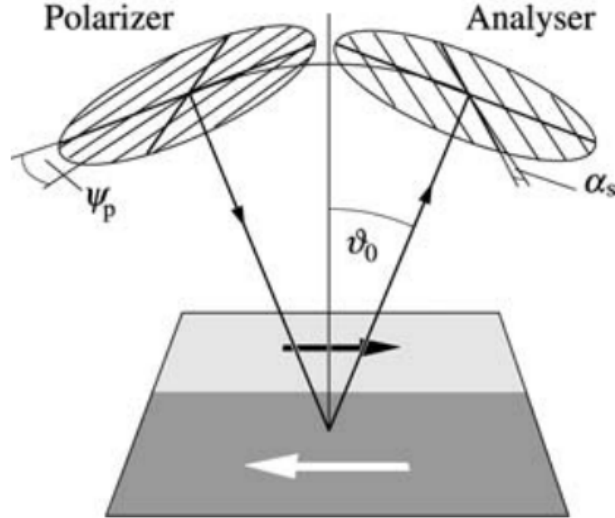
Figure 3.3: Orientation of polarizer and analyzer on Kerr Microscope setup. [50]

3.1.2 Alternating Gradient Field Magnetometry (AGFM)

Magnetic properties of magnetic thin films are characterized using Alternating Gradient Field Magnetometry (Fig. 3.4). In order to characterize the magnetic properties of the prepared samples, the thin film is mounted onto a sample holder that is connected to a

piezoelectric crystal and free to vibrate. The sample is subjected to a DC field and an alternating field gradient which causes the sample to oscillate from the force generated by the alternating field. The frequency of oscillation is tuned to match the resonant frequency of the system which increases the amplitude of the signal. Without tuning, the signal of the magnetic film is too weak to overcome the diamagnetic signal of the sample holder due its ultrathin thickness. The oscillation is the effect of the force generated by the alternating field:

$$\overrightarrow{F} = m_x(H_{DC}) \cdot \frac{\mathrm{d}}{\mathrm{d}x}(H_{DC}) \tag{3.5}$$

with the magnetic moment in the x-direction a function of the static magnetic field. The frequency of oscillation is tuned to match the resonant frequency of the system which results in an increased vibrational amplitude. When the frequencies match, the amplitude is increased by a factor equal to the quality factor of the system (Q). The amplitude is detected by the piezoelectric crystal which generates a voltage proportional to the magnetic moment of the sample. A magnetic hysteresis loop is generated by varying the strength of the alternating field. For this particular study, the films were characterized along both the easy and hard axis of magnetization from -13kOe to 13kOe. The coercivity (H_c) and anisotropy saturation field (H_k) are obtained giving an accurate description of the PMA of the samples. The technique has a sensitivity limit of about 10^{-6} emu, making it ideal to detect the small moments of the thin film samples. On the other hand, the technique is not ideal for characterizing the exact magnitude of magnetic moments because the signal is affected by the frequency tuning. Therefore, characteristics such as saturation magnetization values are obtained using other methods such as Vibrating Sample Magnetometry. However, AGFM is still valuable in tuning the PMA of magnetic samples in order to get the ideal conditions for magnetic domain studies.

3.1.3 Vibrating-Sample Magnetometry (VSM)

For more precise measurements of magnet moments, the Physical Property Measurement System (PPMS) by Quantum Design, Inc is used in the VSM mode. Unlike, the AGFM,
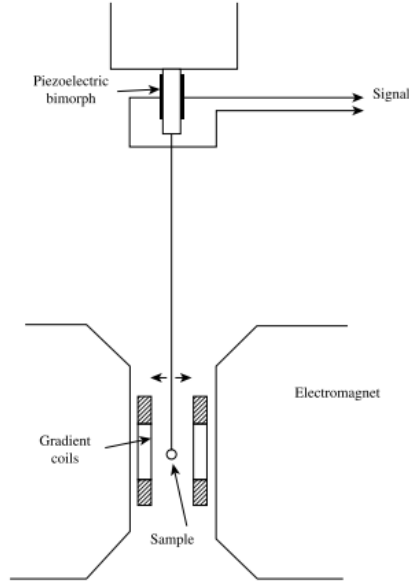
Figure 3.4: Basic Operation of Alternating Gradient Field Magnetometer [14]
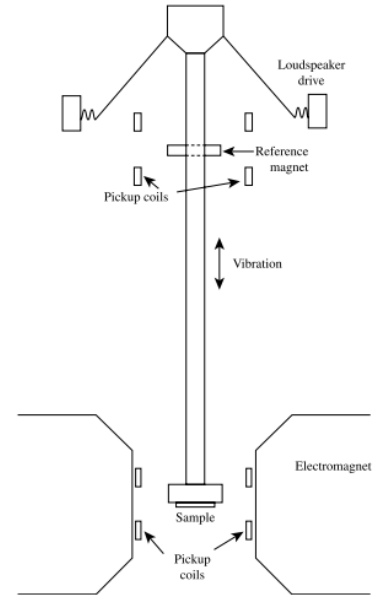
Figure 3.5: Basic Operation of Vibrating Sample Magnetometer [14]

the VSM measures the magnetic moment based on the change in flux of a sample being vibrated at a known frequency. As shown in Fig. 3.5, a sample is attached to the end of a non-magnetic rod and lowered in between an electromagent. A motor at the other end is used to vibrate the rod up to 40Hz. The movement of the sample creates an oscillating magnetic field which induces an alternating electromagnetic force (emf) in the detection coils. The magnitude of the emf is proportional to the magnetic moment of the sample. The VSM must be calibrated with a sample of known magnetic moment in order to have a point of reference for precise measurements. The VSM can detect a moment of about 10^{-5} emu more precisely than the AGFM. In addition, the VSM can apply much larger fields (above 7T) to a sample compared to the AGFM. However, the technique can be more time consuming than using an AGFM, limiting its use to occasions that require saturation magnetization meaasurements, larger applied fields, and temperature studies.

3.1.4 X-Ray Diffraction (XRD)

The magnetic multilayer thin film devices in this study require specific crystallographic texture in order to promote perpendicular magnetic anisotropy. X-ray diffraction is a high throughput method that will be used to characterize texture primarily for the purpose of

tuning deposition conditions in order to achieve optimal PMA in magnetic multilayer films. The technique involves directing monochromatic and collimated x-rays at a sample and analyzing the intensity of reflected x-rays. In the case of the thin films in the study, out-of-plane scans are mainly used for characterization. The x-rays are diffracted by lattice planes parallel to the surface. When the diffraction planes fulfill the Bragg condition, the incident x-rays undergo constructive interference. For this thesis work, XRD is performed using Cu-kα x-rays which have a wavelength of $\lambda = 1.504\text{\AA}$. The Bragg equation is used to characterize XRD peaks and calculate the d-spacing in each layer:

$$n\lambda = 2d\sin\theta \tag{3.6}$$

$$d = \frac{a}{\sqrt{h^2 + k^2 + l^2}} \tag{3.7}$$

The sample is scanned through a range of incident and detector angles to find characteristic peaks that is used to determine the texture of the film. In the case of Co/Ni multilayers, PMA is achieved when films are deposited with (111) texture. Using XRD, the (111) peaks for Co, Ni, Pt, Au, Ta (BCC), and a range of heavy metals are expected to be seen at 2θ = 44.28°, 44.49°, 39.75°, 38.19°, and 47.67°(BCC), respectively, when Cu-Kα x-rays are used. The quality of the texture is determined by obtaining rocking curves of the (111) peaks. The incident and detector are set to the angles that produce the (111) peaks while the tilt of the sample is varied. The FWHM of the resulting curve is characteristic of the quality of the texture, with a lower FWHM indicating a better texture. A larger range of intensities (higher FWHM) indicates that a larger number of (111) planes in the sample are not parallel with the sample surface. As the texture improves, more (111) diffraction planes are aligned with the film surface which means most of the intensity will occur when the sample has zero tilt, resulting in a much sharper peak. Unlike powder XRD, thin films require no additional processing in order to be characterized, making the technique valuable for tuning deposition conditions to achieve PMA in Co/Ni thin films.

3.1.5 Transmission Electron Microscopy (TEM)

For more detailed studies of the crystallographic properties of the thin film samples, transmission electron microscopy (TEM) is used. In the case of thin films, high resolution imaging is performed on cross-sectional TEM samples. A sample is loaded into the TEMs electron column, directly below the electron filament. Electrons are accelerated at the sample giving them enough kinetic energy to pass through a sample that has been thinned. In the case of thin films, there is more interest in the crystallographic orientations of individual layers rather than surfaces. Extra processing is required beyond thinning and polishing the surface of the substrate. Two pieces of the thin film are cemented together and the thinned by grinding and polishing one edge. This produces an electron transparent sample ($\sim$10nm - 100nm) that displays individual layers in a thin film. Magnetic lenses are used to focus the beam and the sample is adjusted to ensure that it is lined up along a recognized zone axis. When electrons interact with the sample atoms, they are diffracted at very small angles. The amount of diffraction determines the contrast in the TEM image. A bright region indicates electron beams passing through without interaction. A darker region indicates a column of atoms at that location. The Technai in the CMU Characterization Suite is used in bright field- high resolution mode at 200kV to image cross sectional samples. The technique will mainly be used to confirm the (111) texture of individual layers and verify the quality of the deposition. The technique is more crucial when optimizing domain wall device fabrication and checking for pinholes, defects, and roughness issues. It is less important for verifying crystallographic texture, because XRD is a simpler and high-throughput technique that requires less sample processing.

3.1.6 Brillouin Light Scattering Spectroscopy

Brillouin Light Scattering (BLS) Spectroscopy is a characterization technique used to determine the magnitude and direction of the DMI vector in our thin film samples, independent from the studies on chiral domain walls. The technique was performed by collaborators at NIST (Boulder, CO) as a way to further verify the results in this thesis work. Brillouin light scattering describes the interaction between an electromagnetic wave and a density wave. Phonon-phonon interactions in a material, caused by thermal vibrations, lead to
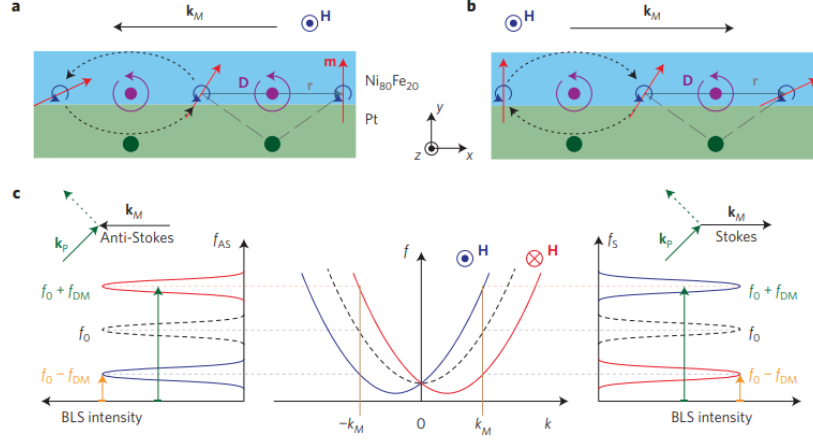
Figure 3.6: (a) Damon-Eshbach spin wave propagating in -x direction corresponding to a left-handed chirality. (b) Damon-Eshbach spin wave propagating in +x direction corresponding to a right-handed chirality. (c) BLS intensities generated from frequencies detected at different wavevector (k) magnitudes for Stokes/anti-Stokes events. [52]

density variations in the the material. In turn, the interaction electromagnetic waves and the density variations result in inelastic scattering. A Stokes event refers to the loss of energy to create a phonon. An Anti-Stokes event refers to the energy gained by the absorption of a phonon. Materials properties such as elasticity can be obtained by observing the photon frequency shift after the interaction and relating it to the energy of the phonon generated/absorbed, given by this equation:

$$\Delta\omega_B = \pm\frac{4n\pi}{\lambda_0}v\sin\frac{\theta}{2} \tag{3.8}$$

where ω is the frequency shift of the scattered light, n is the refractive index of the material, $lambda$ is the wavelength of the incident light, θ is the angle between the incident and scattered light, and v is the phase velocity of the acoustic wave.

This technique has been adapted for the characterization of interfacial DMI in magnetic thin films. Instead of the interaction between electromagnetic waves and phonons, this technique characterizes the interaction between incident light and spin-waves that exist because of DMI in the system. In perpendicularly magnetized materials, (spin-waves) that propagate in the -x direction will have left handed chirality, while spin-waves that propagate in the +x direction will have a right handed-chirality (Fig. 3.6). However, in materials

that have DMI, the chirality of the spin-waves is dictated by the direction of the DMI vector. Therefore, when incident electromagnetic waves interact with quantized spin-waves in a material (generating a Stokes/anti-Stokes event), the change in energy and frequency uniquely identifies the direction of the DMI vector. The presence of DMI in a system changes the spin-wave frequency by this equation:

$$f_m = f_0 + \Delta f_{DMI} \tag{3.9}$$

For this technique, the material is magnetized in opposite directions in order to characterize the Stokes (generation of magnon) and anti-Stokes (annihilation of magnon) events to obtain and compare the spin-wave frequencies from both events (Fig. 3.6). The change in frequency (Δf_{DMI}) is used to characterize the DMI direction and magnitude in the system using the equation [52]:

$$\Delta f_{DMI} = \left| \frac{g^{\parallel} \mu_B}{h} \right| sgn(M_z) \frac{2D_{DMI}}{M_s} k_x \tag{3.10}$$

where $g^{\parallel}$ is the in-plane spectroscopic splitting factor and k is the wavevector of the spin-waves.

3.2 Thin Film Samples and Device Fabrication

3.2.1 Thin Film Deposition - Sputtering

Magnetic samples are prepared using sputtering a method that involves the use of high energy ions in plasma to deposit monatomic layers of materials on a substrate. DC sputtering is the primary method for depositing conductive layers, which make up the composition of the magnetic systems to be tested. In DC sputtering (Fig. 3.7), an inert gas (Ar) is pumped into a chamber under vacuum. A voltage is applied to the target, which acts as a cathode in the system. Argon atoms are ionized and accelerated at the cathode, transferring momentum, and causing the target to release atoms. The ejected atoms move from the cathode to the anode (substrate) and is deposited on the surface. The studies described in this proposal are of magnetic multilayer systems deposited using a 5-target deposition system. The tool is custom built to house five targets with a rotating substrate table as well as target
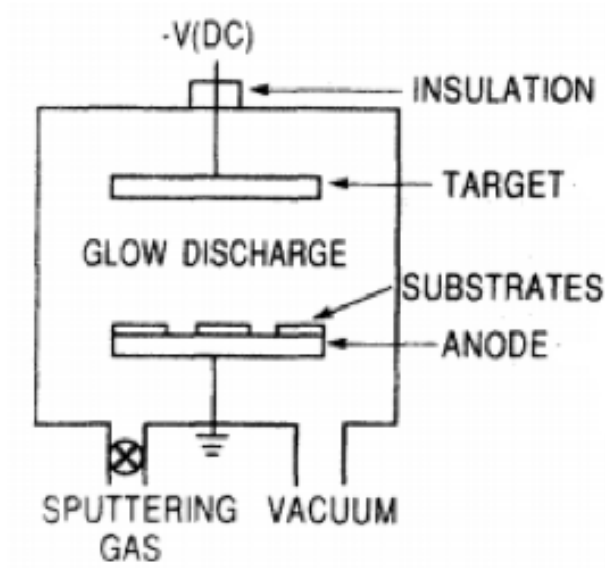
Figure 3.7: Basic schematic of DC sputtering deposition

shutters as required to fabricate appropriate test samples. In this setup, the targets face the substrate table directly. In addition, the system has a load lock to increase the throughput of the samples. Deposition conditions for each material will be summarized and tabulated in more detail below. The base pressure of the tool is extremely important to the quality of the samples produced. When base pressure is low, more material will be deposited on the wall chamber than preferred and ionization cannot be sustained. However, if the pressure is too high, target atoms have more collisions leading to poor deposition. The base pressure of the 5-target system is capable of reaching below 5×10^{-7} Torr. Films deposited at this base pressure have been shown to have the (111) crystallographic texture, which is necessary to achieve perpendicular magnetic anisotropy (PMA) in magnetic multilayers.

3.2.2   Thin Film Deposition Techniques

Thickness Gradient - Wedge Technique

In addition to normal sputter deposition, wedge techniques will also be employed to create thin films where a chosen layer will be deposited as a thickness gradient across the wafer (Fig. 3.8). This technique makes the process of testing thickness effects on a thin film more convenient and less prone to variability because it eliminates the need to do separate runs

for different thicknesses. The substrate is moved forward into the plasma and removed in the reverse direction creating a layer with variable thickness. The leading edge spends more time in the plasma path, while the trailing edge spends less time the plasma path. Because the travel of the substrate is kept at a constant RPM, a layer with a linear thickness gradient is deposited. Using this method we can characterize the effect of thickness on the induced interfacial DMI in the thin film system.

Composition Gradient - Wedge Technique

The wedge technique can also be expanded to deposit composition gradients important for investigating alloying in magnetic multilayer films (Fig. 3.8). It is similar to the wedge technique where a substrate enters a plasma and reverses out. Unlike the thickness gradient technique, it requires multiple plasmas and higher substrate speeds. Increasing the speed of a substrate through two (or more) plasmas repeatedly will deposit alternating monolayers (or smaller) of each plasma target. Like the wedge technique, the monolayers vary in thickness across the substrate. After many cycles, the resulting layer is made up of several monolayers deposited on top of each other. Ideally, the technique promotes intermixing of two materials creating a layer with a two-component alloy. Using this technique it is possible to characterize the effect of composition on the induced interfacial DMI in the thin film system.

Composition Gradient - Aperture Technique

More precise alloying deposition is achieved by installing custom apertures in the 5-target system. The shutters are designed to vary the deposition rate of the target material in a predetermined direction on the substrate more precisely than the wedge deposition technique. As seen in Fig. 3.9, the substrate moves continuously through a plasma without stopping. The apertures restrict deposition in certain parts of the substrate while promoting deposition in others. Combining this technique with multiple co-sputtering targets allows for multi-component alloying in addition to improving the precision of deposition, as seen in Fig. 3.10. With each point on the substrate corresponding to a different film composition, this technique is invaluable as a high-throughput method to test the effects of composition
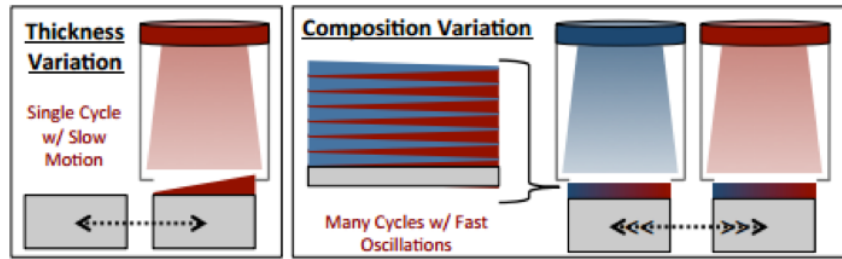
Figure 3.8: (1)Variational Thickness Technique and (2)Variational Composition Technique
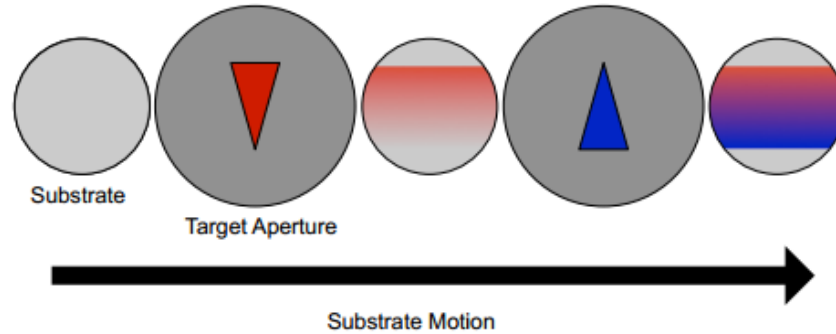
Figure 3.9: Varying Thickness Deposition using Custom Apertures
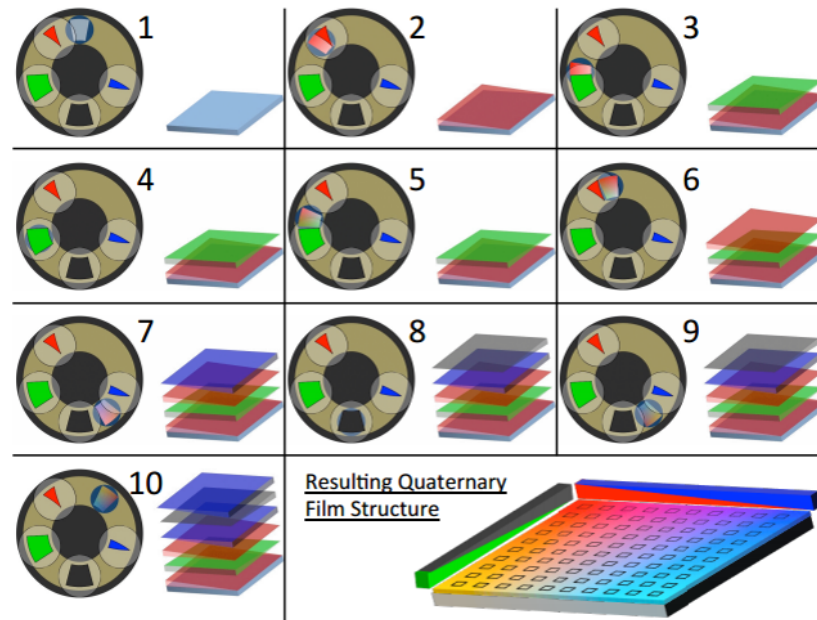
Figure 3.10: Quaternary Film Deposition using Four Custom Apertures

on DMI.

3.2.3 Domain Wall Device Patterning

In order to observe domain wall velocity as a function of current density, nanowires are fabricated from the film stacks made from sputter deposition. The wires will have a length of $\sim 30\mu$m and widths between 2-4μm. Due to the dimensions, the main technique for patterning will be photolithography. Wire widths smaller than 2μm, will require electron beam lithography. The process flow for nanowire patterning is depicted in Fig. 3.11. First, AZ-4110 photoresist is spin-coated on the surface of a sputter deposited magnetic thin film. The photoresist is exposed and developed to form a mask for the etching of individual nanowires. The deposited photoresist is a positive photoresist, so the portions exposed to the UV light are removed when the substrate is submerged in the AZ-400K developer solution. The substrate is placed in an ion mill (Chapter 3.2.4) to etch away all of the magnetic thin film except the portions masked by photoresist, leaving the patterned nanowires. Several photoresist exposure and development steps are required to pattern the metal contact structures, as seen in Fig. 3.12. The metal contacts are constructed so probe stations can inject current into nanowires for domain wall motion and domain wall creation. The photoresist AZ4210 is spin-coated onto the substrate, exposed, then developed to form a mask for the metal contacts. Gold is then deposited directly onto the substrate which is then followed by a lift-off process. During the lift-off procedure, the substrate is submerged in acetone in order to dissolve the photoresist. The gold film that was deposited directly on the photoresist is removed, leaving the gold film that was deposited directly onto the substrate as our contacts. Multiple chips with many nanowires can be fabricated from a single 3-inch silicon dioxide (SiO_2) substrate.

3.2.4 Ion Milling

The process to create nanowires involves ion milling, a physical etching process that involves accelerating neutral atoms (Argon ions) at the surface of a sample in order to physically remove atoms from the surface. Argon gas is ionized in a chamber then passed through a grid and a neutralization filament to form collimated ion beams which strikes the sample at a low chamber pressure (10^{-4} - 10^{-3} Torr). The ion milling technique is an anisotropic process that has a lower etch rate (compared to other etching techniques) and low selectivity.
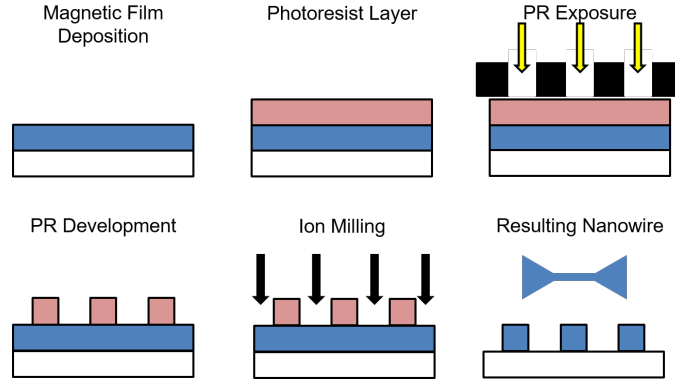
Figure 3.11: Process flow for magnetic domain wall device patterning.
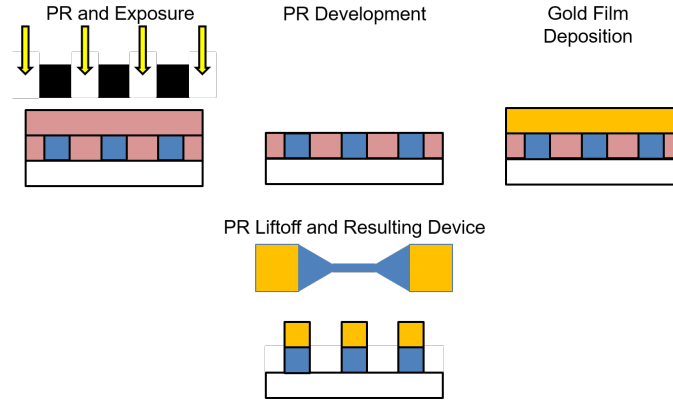
Figure 3.12: Process flow for fabrication of metal contacts for domain wall devices.

Compared to chemical etching (isotropic process), there is little undercutting of the thin film beneath the photoresist. The low selectivity means that all materials exposed to the ion beam will etch away at different rates. With the use of an endpoint detector, it is possible to track the ion milling process and stop it when the desired layer in the film stack is reached. In this case, the endpoint detector was monitored to stop the ion milling after the sample was milled all the way to the substrate.

3.3 Film and Domain Wall Device Testing

3.3.1 Magnetic Film Testing

Thin film studies are done to observe domain wall velocities as a function of in-plane magnetic fields. The Kerr Microscope (Fig. 3.13) is outfitted with a sample stage with an electromagnet to induce a perpendicular magnetic field. The electromagnet is custom machined brass rod, machined to fit in the Kerr Microscope. In addition, there is also a controllable

in-plane magnetic field produced by two iron pole pieces. The Kerr Microscope, a product of Evico-Magnetics, is a wide-field, polar-sensitive (Kerr effect), white light microscope out-fitted with a CCD. The software suite is capable of performing real-time difference imaging of domain walls. Both the in-plane magnet and the perpendicular magnets are powered with a KEPCO power source, capable of delivering about 6A of current to power the electromagnets. Domain wall velocity can be measured using a 20X objective to observe bubble domains and large infinite domain walls. Thin film samples are irradiated at predetermined spots in order to create a point of lower magnetic anisotropy. Essentially, the manufactured defects are points where bubble domain will nucleate. The samples are irradiated using a focused ion beam (FIB) by pulsing a 300ns beam at 5.0kV and a current ranging from 12.0pA to 1.0nA (depending on the thin film composition). A perpendicular field is applied to saturate the entire film in one direction (down), and then a smaller pulse is applied in the opposite direction to create a region on the film with the opposite magnetization (up). Domains are grown by applying pulses of perpendicular magnetic field pointing out-of-plane. Asymmetric growth is observed when an in-plane field is applied, a direct result of asymmetric velocities caused by a combination of the in-plane field and Neel wall chirality, giving insight into domain wall behavior.

3.3.2 Domain Wall Device Testing

Nanowire tests are done to observe the domain wall velocity as a function of current density. Testing the nanowire devices require a 100X objective on the Kerr Microscope. The Kerr microscope is outfitted with a larger perpendicular magnet with a sample stage. In addition, electrical probes (GS probes) are setup to be in contact with the devices. Using a LabView controller, electrical pulses can be sent through the probes from an AVTECH pulse generator and monitored by a connected oscilloscope (LeCroy). A Keithley sourcemeter is also used to obtain the total resistance of an individual nanowire device. For domain wall characterization, the device is first saturated in-plane, using a large perpendicular field. Like the film level studies, domain nucleation sites are created on the larger pads pictured, using the Ga+ Ion Fib Procedure explained above. The conditions for Ga+ ion irradiation
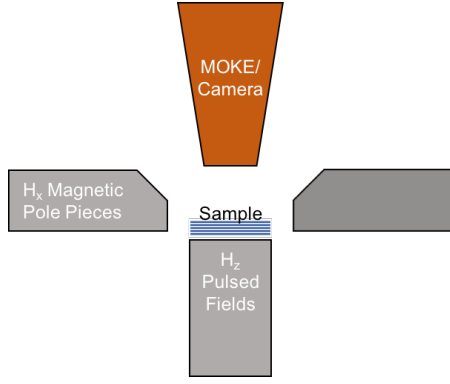
Figure 3.13: Schematic of field level DW characterization
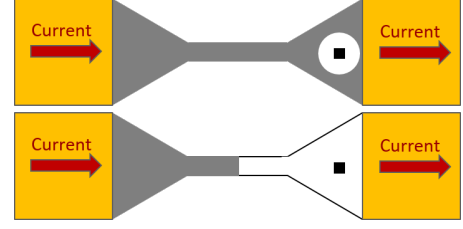
Figure 3.14: Schmatic of device level DW characterization. Red arrows depict the induced magnetic field.

are 50ns at 30.0kV and a 1.0nA beam current. By applying a smaller perpendicular field out-of-plane, a domain nucleates and expands into the nanowire structure of interest. As seen in Fig. 3.14, current is applied through the leads in order to move the domain wall. The direction of the wall motion is controlled by the positive or negative voltage applied to the system. Similar to the film characterization, the wall displacement is measured, giving insight to the magnetic thin films current induced domain wall motion capabilities.

CHAPTER IV

Characterization of DMI in the Pt/[Co/Ni] System

It has been suggested that a magnetic system with perpendicular magnetic anisotropy is ideal for commercial domain wall motion devices, in terms of stability and storage density. There have been many studies that examine other systems such as the Pt/Co multilayers, but the Co/Ni multilayer system was chosen as the representative magnetic structure for all our studies investigating interfacial DMI in a thin film. After optimization of the fabrication process, the Co/Ni system has been shown to exhibit PMA and a high anisotropy field [24], making it ideal for field driven domain wall tests. This is demonstrated by early work on magnetic racetrack memory done on the Co/Ni systems, making it an suitable test system [2, 4, 6, 7, 7, 9–11]. This thesis work will focus on variations of the $SiO_2/TaN/Pt/[Co/Ni]_2/Co/TaN$ filmstack in order to study the effects seedlayer engineering on interfacial DMI.

4.1 Pt/[Co/Ni]/Co/Ta Magnetic Multilayer

The Pt seedlayer was initially chosen because it has been theorized to have the highest DMI magnitude among possible transition metal seedlayers [11, 20, 27, 33]. Under certain deposition conditions, a platinum seedlayer is also conducive for getting the ideal perpendicular magnetic structure. Furthermore, the $Pt(111)/Co(111)$ interface has been studied extensively in literature because of its potential to induce a high perpendicular magnetic anisotropy. That makes the $Pt/[Co/Ni]$ structure ideal for studying the effects of DMI. However, our initial studies on $TaN/Pt/[Co/Ni]/TaN$ system showed less than ideal behavior in terms of magnetic characteristics and domain formation. The measured anisotropy
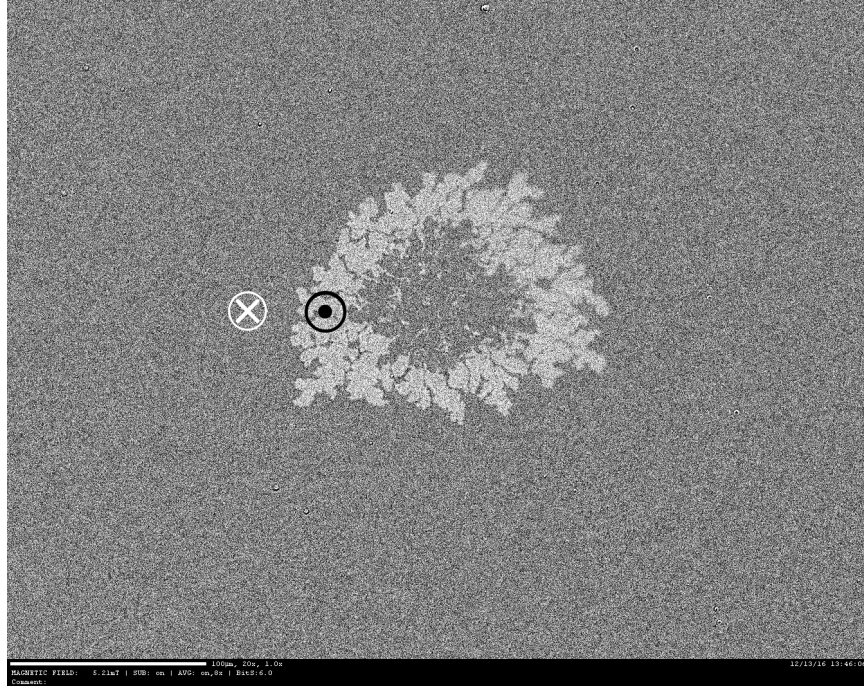
Figure 4.1: Dendritic sample formation of $Pt/Ir/[Co/Ni]_4/Co$ (4.5 repeats) with known low anisotropy.

(H_k) was lower than ideal, making the domain structure appear more dendritic than uniform. In materials that demonstrate a higher effective anisotropy, the energy required to for a domain wall to form is much higher. Therefore, in films that have low effective anisotropy, it is energetically favorable to create more interfaces (appearing more dendritic) to lower the total energy of the system [53–55]. In films with higher effective anisotropy, it is energetically favorable to form short and smoother interfaces in order to reduce the total domain wall energy in the system. Optimization of the deposition procedure included increasing the thickness of the Pt seedlayer, increasing the thickness of the magnetic Co and Ni layers, and also increasing the number of repeats attempting to improve the magnetic characteristics of the film [56,57]. As seen in Fig. 4.1 and Fig. 4.2, films with a low H_k exhibit dendritic domain formation making it difficult to extract consistent velocity data. In turn, the domain wall behavior makes extraction of DMI from the sample difficult.

It was suggested that the fabrication procedure was flawed during the capping layer deposition. TaN was originally chosen as a capping and underlayer material because of its insulating properties, ideally directing the applied current in a domain wall device through
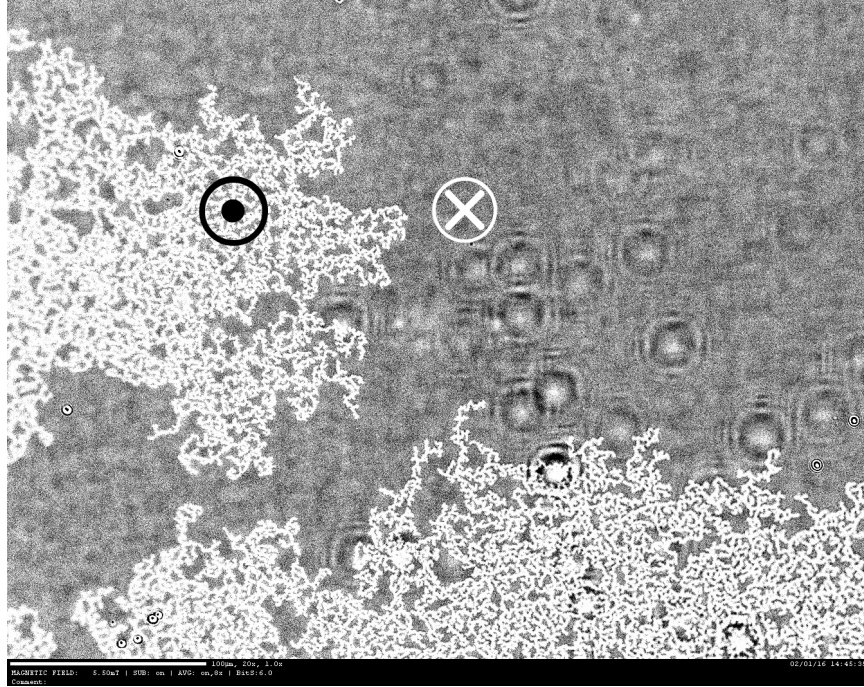
Figure 4.2: Dendritic sample formation of $Pt/Ir/[Co/Ni]_6/Co$ (6.5 repeats) with known low anisotropy. Circular regions are artifacts caused by particles on the objective lens.

the more conductive seedlayer. However, the addition of N_2 gas in the plasma to produce TaN directly on top of the magnetic repeats could interfere with the Ni, adversely affecting its magnetic properties. We introduce an additional deposition of Ta, separating the magnetic repeats from the N_2 deposition of TaN, which addresses this concern. As seen in Fig. 4.3, the thickness of the Ta does not affect the anisotropy of the film during AGFM measurements, suggesting that the H_k value is stable with Pt and Ta seed and cap layers. A more in-depth study (Fig. 4.3) performed by Jaris et al suggests that the anisotropy and the damping characteristics of the film is affected by Ta capping layer thickness [58]. Using their work, an ideal thickness is found in the range of 0.5nm - 0.8nm in order to produce a film for DMI characterization. In addition to the cap, the seed and the thickness of the Co/Ni repeats have been optimized for this study, striking a balance between the magnitude of the magnetization and the anisotropy direction. More Co/Ni repeats results in an increased magnetic signal. However, if the magnetic film becomes too thick, the DMI inducing effects of the Pt/Co interface diminishes and we also observe the formation of dendritic domain walls. The optimal thickness for a strong mag-
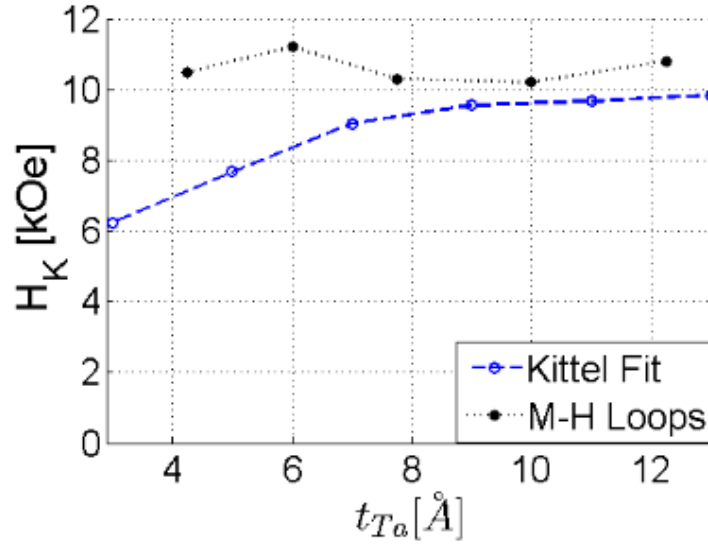
Figure 4.3: Comparison of H_k values evaluated using (1) Alternating Gradient Field Magnetometry (CMU) and (2) Time-Resolved MOKE Spectroscopy (UCSC) [58].

netic signal and a perpendicularly magnetized film was 2.5 $[Co/Ni]$ repeats and a Pt seed-layer [56,57,59], where the Co and Ni are 0.2 and 0.6 nanometers thick, respectively. As seen in Fig. 4.4, most of the samples studied in this thesis work has the following composition: $TaN(3nm)/Pt(2.5nm)/[Co(0.2nm)/Ni(0.6nm)]_2/Co(0.2nm)/Ta(0.5nm)/TaN(6nm)$. The initial TaN layer serves as an adhesion layer that has some electrical resistivity. The Pt seedlayer induces the interfacial DMI in the system and is also the source of the spin-transfer torque (through the spin-hall effect) for nanowire devices. The $[Co/Ni]$ multilayers serve as the magnetic layer in the filmstack. The additional Ta layer is added to reduce the harmful effects of N_2 gas on magnetic properties during the deposition process, increasing the anisotropy in the system. Finally, TaN serves as a capping layer to prevent oxidation.
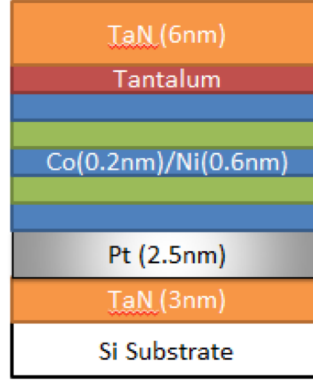
Figure 4.4: Proposed study system: TaN/Pt/[Co/Ni]/Ta/TaN.

4.2 Film Morphology and Magnetic Characterization

4.2.1 X-Ray Diffraction (XRD) Characterization

X-ray diffraction is the primary characterization technique used to determine the crystallo-graphic orientation of the films. It is known that Co/Ni multilayers will exhibit perpendic-ular magnetic anisotropy when grown in the (111) orientation [8,20,60]. XRD is used in this study during the sputtering optimization process in verify the texture and the quality of the film being deposited. A film of the composition $TaN(3nm)/Pt(2.5nm)/Co(x)/TaN(6nm)$, with x ranging from $1.5nm$ to $10.0nm$, is constructed to observe the change in orientation as the Co layer increases. The Co layer is deposited as a linear gradient from a thickness of $1.5nm$ to $10.0nm$. Fig. 4.5 shows the result of the XRD characterization on a pure Pt seedlayer. The peak around $2\theta = 39.75°$ suggests that the conditions are appropriate for deposition of a Pt (111) thin film. The film quality was also characterized by observing the XRD rocking curve at $2\theta = 39.75°$. Fig. 4.6 shows that the full width half max (FWHM) is reasonably small suggesting good film quality, texture, and roughness. Ideally, the de-posited Pt film will serve as a template for the growth of the magnetic films in the (111) orientation. According to calculations using Equations (3.6) and (3.7), the Pt (111) peak should appear at $2\theta = 39.75°$ and the Co (111) peak is expected to appear at $2\theta = 44.28°$. The TaN is expected to be amorphous, where no peaks are visible. As seen in Fig. 4.7, both the Pt and Co peaks are present as expected. The Pt remains at $2\theta \sim 39.75°$ for all points the samples tested, which suggests a uniform deposition of the desired Pt texture across
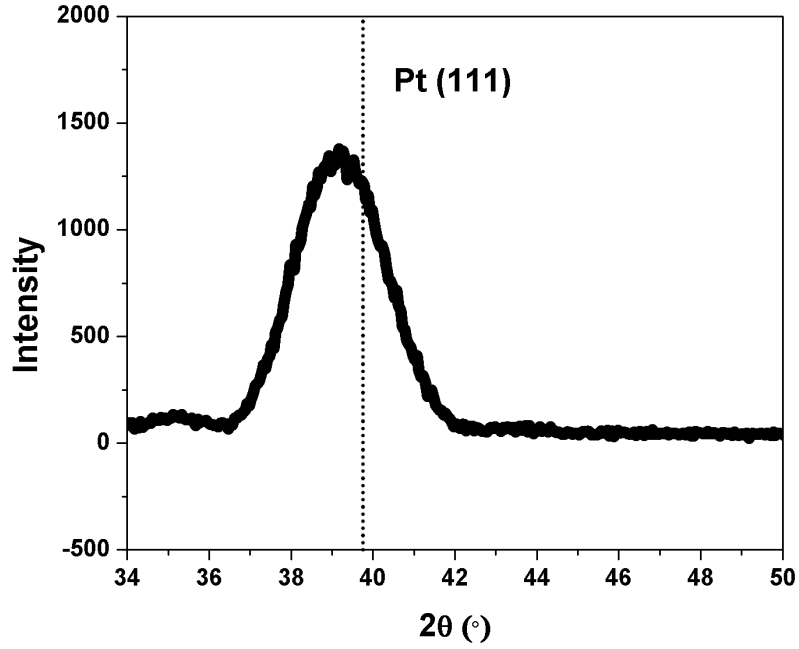
Figure 4.5: XRD spectra characterizing a Pt (111) thin film. Theoretical Pt (111) peak indicated.

the substrate. However, as the thickness of the Co layer increases, the Co peak is shown to shift to larger 2θ values. Although the reason is not immediately obvious, the shift in 2θ is indicative of a decrease in lattice spacing. This suggests that there is some stress acting on the deposited Co layer. The cause for this shift has not been further explored, but the study is able to confirm the deposition conditions for growing a (111) magnetic multilayer system.

4.2.2 Transmission Electron Microscopy Characterization

TEM characterization in Fig. 4.8 shows a cross-sectional $Pt/[Co/Ni]_2/Co/Ta$ sample. The characterization was done in order to verify the relative layer thicknesses and the interfacial structure in the system. The image is divided into the different sections and interfaces expected in the system. The sample is deposited in a 3×10^{-7} Torr vacuum environment. The low pressure is required for ideal deposition of layers with minimal surface roughness. The Ar gas pressure required for sputtering is 2.50 mTorr. For the TaN underlayer and
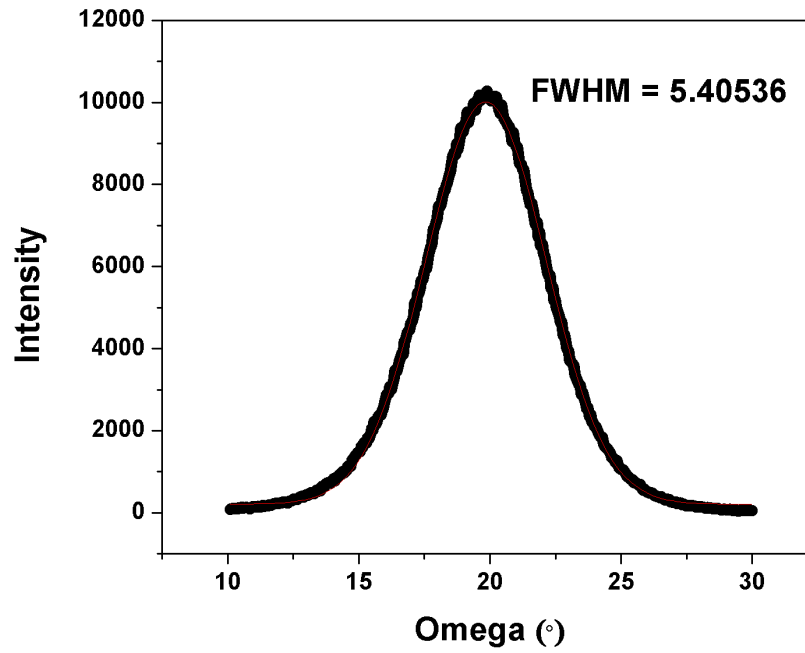
Figure 4.6: Omega rocking curve at $2\theta = 39.75°$ and the observed FWHM.
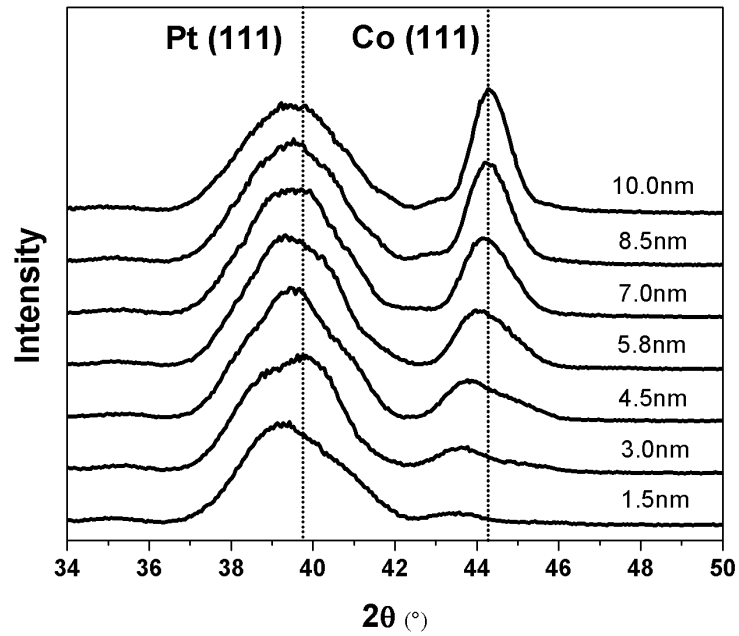
Figure 4.7: Offset XRD spectra characterizing the Pt/Co structure as a function of Co thickness.

capping layer, an additional 0.50 mTorr of N_2 gas is flowed into the system. Lattice fringes can be seen for Si, Pt, and $[Co/Ni]$ layers, indicative of a crystalline structure. Ta and TaN are amorphous as expected and cannot be easily distinguished. Lattice fringes are calculated to roughly confirm of crystal orientation. The deposition conditions were optimized in order to produce a $[Co/Ni]$ layer with (111) crystal orientation, which is an indicator of perpendicular magnetic anisotropy. Pt with a FCC (111) orientation is expected to have a d-spacing of $d = 2.26\mathring{A}$. A rough measurement from the TEM study produces a value of $d_{measured} = 2.24\mathring{A}$. The Pt layer has another function in the system as the seedlayer - to promote (111) crystal growth in the layers deposited on top of it. Depositing Co and Ni on top of TaN is ineffective at producing the desired texture. However, having the Pt seedlayer promotes the (111) texture in the ferromagnetic layers of the system. Co and Ni layers are harder to distinguish because the expected d-spacing is almost the same but the crystal orientation appears to be FCC (111) for Co and Ni. Both Co (111) and Ni (111) are expected to have similar d-spacings of $d \sim 2.04\mathring{A}$ and from rough analysis a value of $d_{measured} = 2.04\mathring{A}$ was obtained. The d-spacing for the Si layer is measured to be about $d = 3.14\mathring{A}$. Si (111) is expected to have $d = 3.14\mathring{A}$. The discrepancy can be explained by the drift in the electron beam during imaging. The TEM gives a rough idea of the interfaces and layer thicknesses in the system and helps verify the expected structure of the system. More intensive TEM studies may be conducted in the future in order to quantitatively verify the surface roughness and the chemical composition of each layer. Extra effort in the TEM characterization will result in a better understanding of the how chemical composition and interface quality plays a role in DMI.

4.2.3 Alternating Gradient Field Magnetometry Characterization

AGFM is the primary technique used to determine relevant magnetic characteristics of deposited thin films. Samples with varying tantalum thicknesses were tested as part of the thickness gradient wedge structure. show the out-of-plane magnetization curves for a sample with a Ta thickness around 0.5nm. The out-of-plane curve shows a square hysteresis loop, which indicates that the easy axis of magnetization is perpendicular to the film nor-
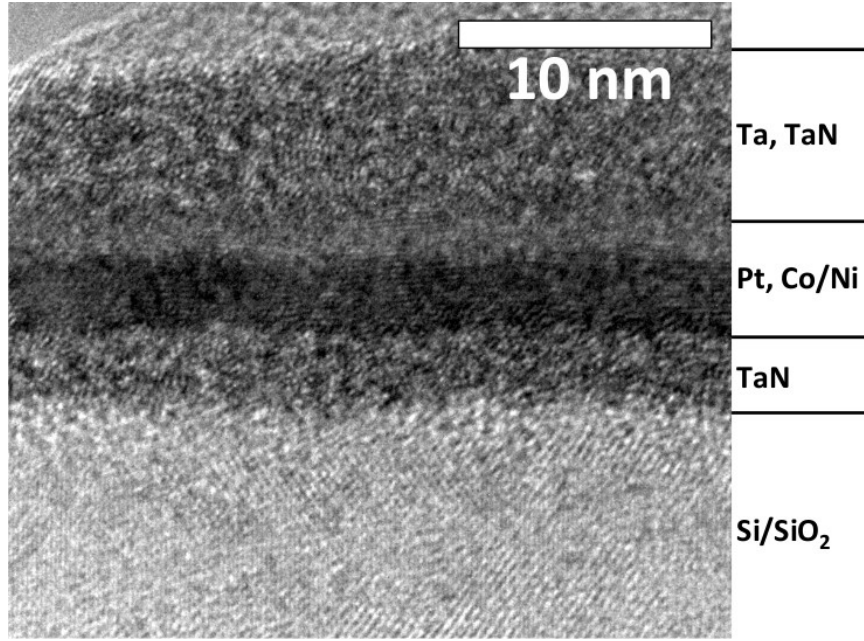
Figure 4.8: Pt/[Co/Ni]/Co/Ta Cross sectional TEM sample.

mal. The films clearly exhibit perpendicular magnetic anisotropy. Also, the measured coercivities (H_c) for the sample is ~ 100 Oe. The saturation magnetization (M_s) is determined through VSM to be $M_s \sim 600kA/m$. The anisotropy field (H_k) is $\sim$11kOe (Fig. 4.9) for all samples tested. The hysteresis loops are almost square which suggest that the entire film magnetically switches when the external magnetic field is equal to the domain nucleation field. The switching mechanism, in this study, is through domain wall motion allowing us to observe domain wall behavior. The coercivity field is shown to be around $\sim 100Oe$ (Fig. 4.10), which determines the magnitude of the field that we will use for the field driven domain tests. Since the film switches when magnetization is above $100Oe$, field driven tests will pulse perpendicular magnetic fields at $\sim$4.25mT ($42.5Oe$) and approaching $10.0mT$ ($100Oe$). The hysteresis loops of all the samples show a square loop, which helps confirm good texture (Mr/Ms ~ 1).

AGFM measurements are also used to characterize properties of the magnetic system such as effective uniaxial anisotropy (K_{eff}), domain wall width (λ), and domain wall energy density (σ_0), which are important values for describing domain wall motion [30, 31] and energetic mechanisms of our system. The values are then used to fit domain wall veloc-
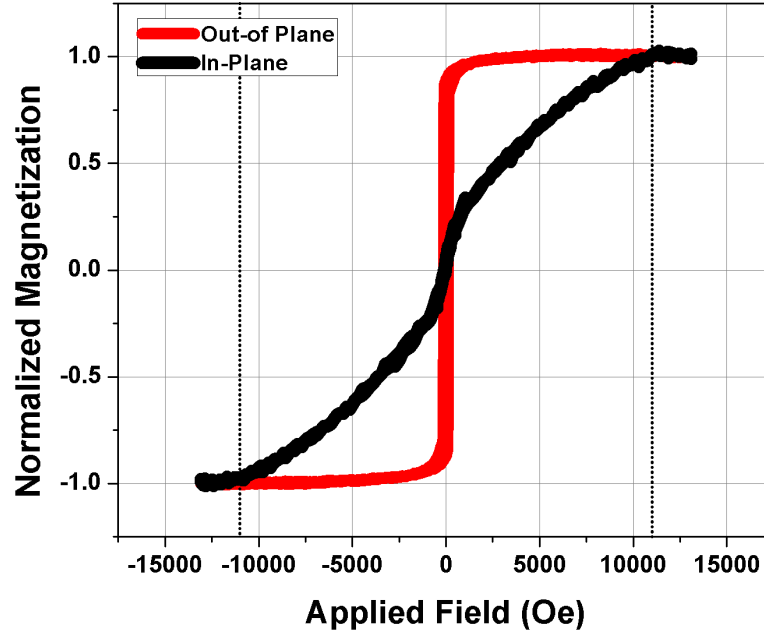
Figure 4.9: Magnetization loops along easy (red) and hard (black) axes of TaN / Pt / [Co/Ni] / Co / Ta / TaN filmstack. Measured anisotropy field of $H_k \sim 11kOe$.

ity and behavior models discussed later in this document. In the case of the deposited TaN/Pt/[Co/Ni]/Co/Ta/TaN films, the value is calculated to be $K_D \sim 3 \times 10^4 J/m^3$. The measured coercivity and anisotropy fields are $\mu_0 H_c \sim 10mT$ and $\mu_0 H_k \sim 1T$ The uniaxial anisotropy constant is calculated to be $K_{eff} \sim 3 \times 10^5 J/m^3$. The domain wall width is found to be $\lambda \sim 6 \times 10^{-9} m$. The resulting Bloch wall energy density is estimated to be $\sigma_0 \sim 0.017 J/m^2$.
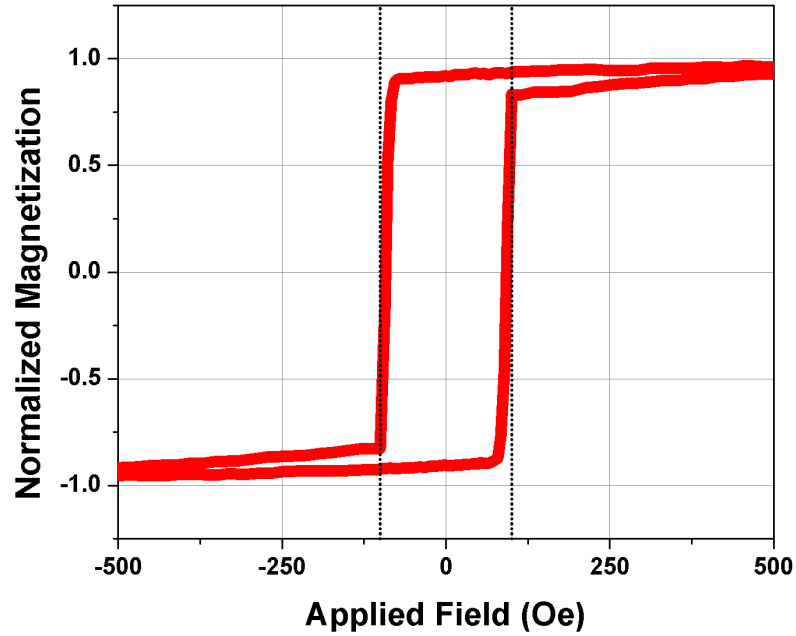
Figure 4.10: Magnetization of TaN/Pt/[Co/Ni]/Co/Ta/TaN filmstack along easy axis. Measured coercivity of $H_c \sim 100Oe$.

4.3   DMI Characterization using Kerr Microscopy

In Chapter 2.3.2, the common techniques used to characterize DMI were introduced and briefly discussed. The focus of this thesis work will be to use asymmetric field driven domain wall growth as the main method to characterize DMI. The reason this technique was chosen is because it requires very little sample preparation. Most of the characterization is performed with a MOKE microscope, essentially an optical microscope. For film level characterization, field driven domain wall motion is advantageous because the technique does not require patterning domain wall devices, which are primarily driven by current. Combined with MOKE microscopy, studying asymmetric domain wall growth is a high throughput method that can be used to evaluate DMI for samples with a variety of compositions and film structures. However, there are some drawbacks to the technique, mainly in the interpretation of the experimental results, to be discussed later in the document. Regardless, the advantages of this technique is its simplicity in set up and execution. A sample is loaded into a MOKE microscope outfitted with a perpendicular magnetic source

and a in-plane magnetic source. The sample is positioned directly above the perpendicular field and parallel to the in-plane field, as seen in Fig. 3.13. As explained in 3.3, a initial bubble domain is nucleated by pulsing the perpendicular field at a pre-determined spot with a lower domain nucleation energy [61]. Velocity data is then recorded after pulsing a constant perpendicular field in the presence of in-plane fields of various magnitude and directions [26, 31, 62]. Alternatively, the magnitude of the in-plane field is kept constant while the perpendicular field is varied in order to obtain characterize the relationship between the driving force (H_z) and velocity in the creep regime. Chiral Domain wall motion driven by an external field has been shown to operate in the creep regime [27, 33] and the velocity behavior characterized in this thesis will be modeled and fit to an Arrhenius relationship given by Equation (2.31).

4.3.1 Chiral Domain Wall Behavior in the Creep Regime

In Chapter 2.4.2, the effect of DMI on magentic domain walls was discussed to set the framework for characterizing chiral domain wall motion. Using the conventional model of domain wall behavior, we now focus our attention on field driven domain wall velocity data gathered from experiments with the $Pt/[Co/Ni]_2/Co/Ta$ system. Fig. 4.11 shows representative Kerr images of domain bubbles that form in response to the applied $\mu_0 H_x$ fields and $mu_0 H_z$ pulses. The chirality and the DMI direction in the magnetic system can be obtained qualitatively by observing the asymmetric domain wall growth from the Kerr images. In Fig. 4.11, the bubble domains show asymmetric growth in the direction opposite of the applied H_x field. Based on Fig. 4.11b, the observed growth points to a left-handed chirality and a negative DMI vector. As shown in Fig. 4.12b, the moments rotate counterclockwise when they transition from down to up or up to down, resulting in a domain wall that points towards the center of the bubble. We can also infer the direction of the DMI based on the splitting of the domain wall velocity profiles.

Fig. 4.12 shows velocity profiles plotted from domain walls displaced by pulsing H_z fields (driving force for domain wall motion) in the presence an applied in-plane field (H_x). The
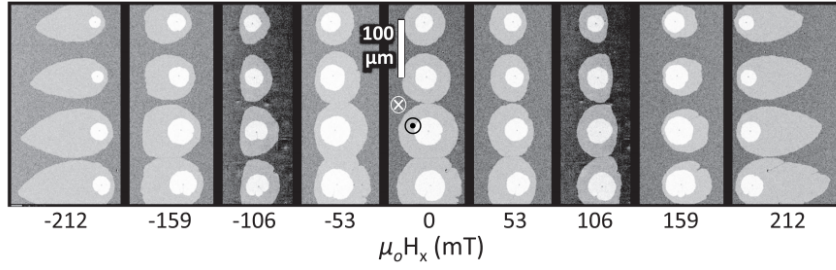
Figure 4.11: Representative bubble domains after $\mu_0 H_z = 4.25mT$ field pulses for selected values of $\mu_0 H_x$ from group of 4 nucleation sites.

experiment was repeated using different magnitudes of H_z pulses to show reproducability. In addition, Fig. 4.12c demonstrates that the domain walls are traveling in the creep regime. Observed domain wall velocities at different H_z pulses were fit to an Arrhenius relationship with reasonable accuracy, which means the domain wall velocity can be explained by the creep regime dynamics and used to extract information about the DMI (Chapter 4.5). Domain wall velocity is a function of domain wall energy due to the energy prefactor in the creep law. The effect of DMI can be characterized by observing the velocity profile directly, extracting the domain wall energy and isolating the DMI magnitude. The velocity profile of both domain walls reach a minimum when $\mu_0 H_x \sim 50mT$, which suggests that $\mu_0 H_{DMI} \sim 50mT$. Using the extracted $\mu_0 H_{DMI}$ and the magnetic properties characterized in Chapter 4.2, the magnitude of the DMI vector can be calculated using Equation (2.32). The resulting DMI vector is $D = -2.025 \times 10^{-4} J/m^2$, with the negative value correpsonding to a left-handed chirality.

Although the velocity curve shift is identified in the plot as expected, the plot has additional features that cannot be explained by the conventional creep law understanding. In addition to the shift, the plots are also asymmetric about the minimum. The conventional creep law only predicts a translational change in the velocity behavior. In addition, there is also a crossover point in the velocity behavior at larger in-plane fields. At $\mu_0 H_x \sim \pm 150mT$, the direction of preferential growth of the bubble domain appear to reverse. Qualitatively, this implies that at a characteristic magnetic field, the domain wall configuration predicted to have higher energy moves moves faster than the low energy configuration, a phenomenon
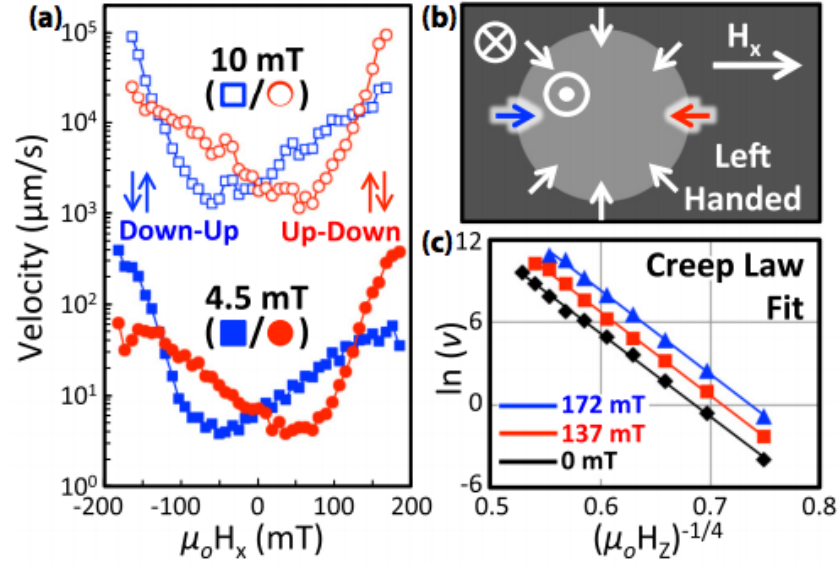
Figure 4.12: (a) Domain wall velocity as a function of $\mu_0 H_x$ for $\mu_0 H_z = 4.25 mT$ and $\mu_0 H_z = 10.0 mT$. (b) Chirality of sample inferred from velocity plots. (c) Domain growth as a function of H_z fit to the creep law.

that cannot be modeled using the conventional creep law. Along with the crossover, the bubble domain also transitions into a different shape at the characteristic field (Fig. 4.11). Fig. 4.13 - Fig. 4.15 show bubble domain growth in response to different values of $\mu_0 H_z$, $\mu_0 H_x$, and starting domain size. These results are evidence that the domain growth behavior is independent of starting size and $\mu_0 H_x$ for different driving fields (H_z). Applying larger magnitudes of $\mu_0 H_z$ simply provides a larger driving force for domain wall motion, but the overall trends in domain shape are unaffected. However, increasing the starting size of the bubble appears to influence the final shape, an indication that domain wall behavior is affected by the magnetostatic interactions in the domain wall. This is further evidence that the anomalous asymmetric growth behavior seen in the bubbles and velocity curves are still governed by the initial domain wall energy, which in turn, is affected by external forces. These observations make it necessary to re-evaluate the role of energy in chiral domain wall behavior. The remainder of this chapter will be be a discussion of the anomalous features and their relation to the mechanisms of chiral domain wall behavior.
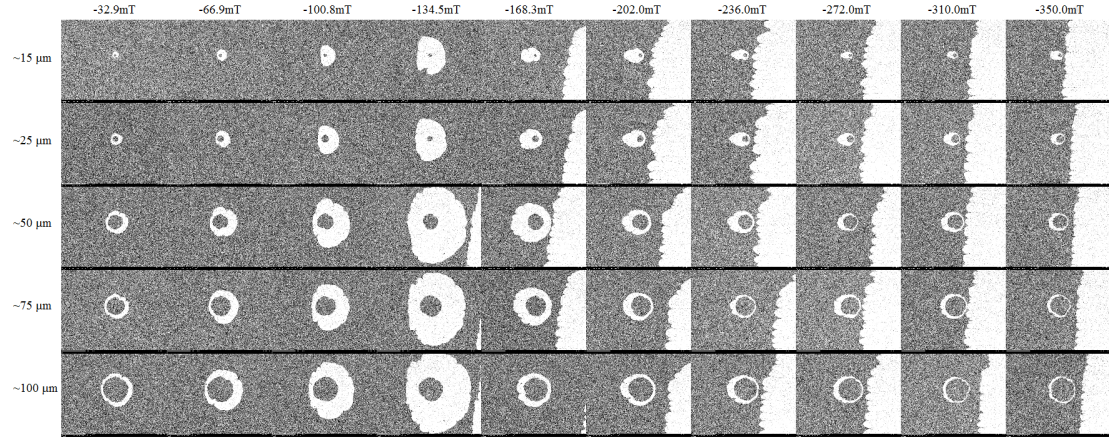
Figure 4.13: Bubble domains grown with $\mu_0 H_z = 4.25mT$ field pulses and applied $\mu_0 H_x$ for different starting domain diameters.
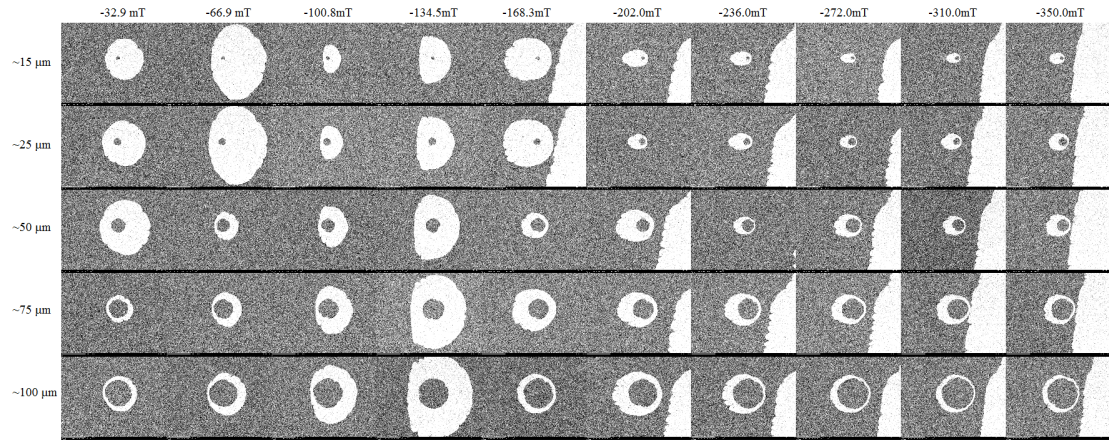
Figure 4.14: Bubble domains grown with $\mu_0 H_z = 6.50mT$ field pulses and applied $\mu_0 H_x$ for different starting domain diameters.
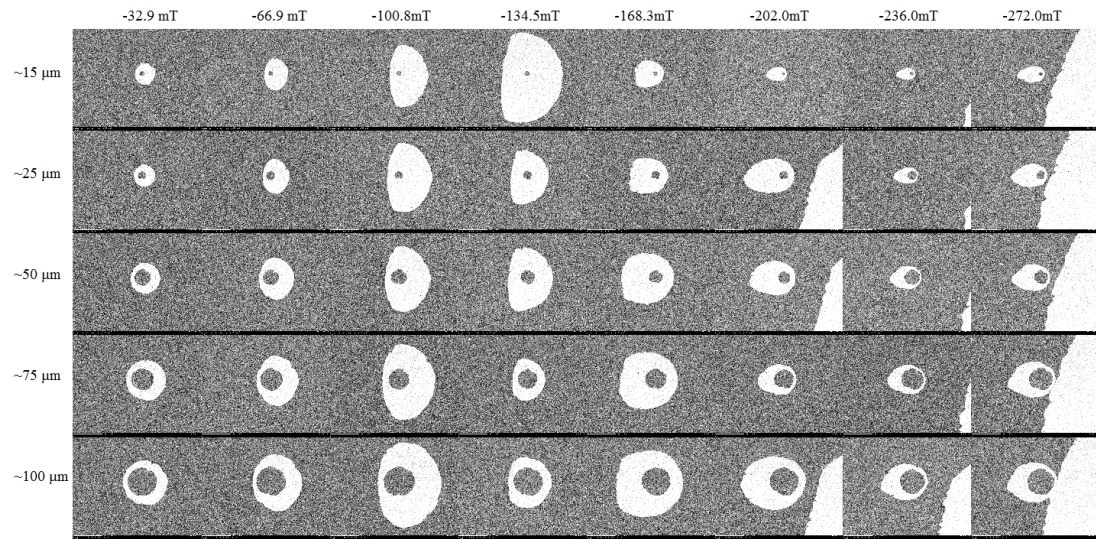
Figure 4.15: Bubble domains grown with $\mu_0 H_z = 8.50mT$ field pulses and applied $\mu_0 H_x$ for different starting domain diameters.

4.4 Driving Force on Equilibrium Bubble Domain Shape

In order to make sense of the anomalous velocity curves, it is important to explain the formation of the non-elliptical domain bubbles that form in response to applied in-plane fields and perpendicular field pulses. The teardrop shapes have been described in literature, but until recently, not frequently enough to warrant further exploration [26, 28, 62]. The resulting shape of the bubble is determined by the anisotropic driving force from the domain wall energy forcing the domain wall towards an equilibrium orientation [63]. Starting with the conventional equation for domain wall energy discussed in 2.3.3, Je et al and Kim et al show that the equation (the conventional domain wall energy equation) can be expanded to Equation (4.2) [29–31, 64] to account for a different coordinate system (seen in Fig. 4.16a)..
In this case, the domain wall energy equation becomes a function of the orientations of the magnetization vector ($\vec{M}$) and the externally applied field ($\vec{H}_x$), both with respect to the domain wall, allowing the domain wall profile to be modeled at each point.

$$\sigma_{DW}(H_x) = \sigma_0 + 2K_D\lambda - \pi\lambda M_s|\mu_0 H_x + \mu_0 H_{DMI}| \tag{4.1}$$

$$\sigma_{DW}(\varphi,\Theta) = \sigma_0 - \pi\lambda\mu_0 H_x M_s \cos(\varphi + \Theta) - \pi\lambda\mu_0 H_{DMI} M_s \sin(\varphi) + 2\lambda K_D \sin^2(\varphi) \tag{4.2}$$

where λ in this case, is the domain wall width. The terms in the modified energy equation are the Bloch Wall energy term, the Zeeman field term from external $\mu_0 H_x$, the Zeeman field term from $\mu_0 H_{DMI}$, and the anisotropy energy term, unchanged from the conventional energy equation. The minimum in domain wall energy is found as a function of magnetization direction, φ, for all possible angles between the domain wall and external applied field (Θ). The equilibrium magnetization direction (equilibrium orientation of the magnetic moment) is determined by finding the orientation that corresponds to an energy minimum at every location along the domain wall. By fixing Θ (which fixes the location along the domain wall), the orientation (φ) that corresponds to the lowest energy configuration is found by minimization, as seen in Fig. 4.16b,c. This energy minimization is used to construct
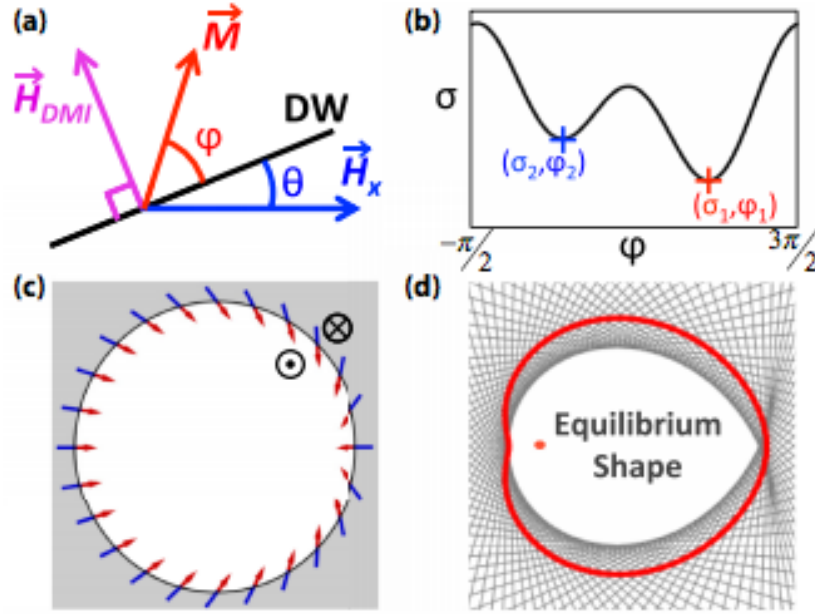
Figure 4.16: (a) Coordinate system used for domain wall energy (Equation (4.2)). (b) Energy minimization for a fixed Θ. (c) Example of equilibrium magnetic moment configuration. (d) Polar energy plot (red) and resulting Wulff construction (gray) of the equilibrium moment configuration. The red dot indicates the origin of the polar energy plot.

of polar plot of minimum domain wall energy as a function of Θ. The polar energy plot can then be used to plot a Wulff construction which theoretically predicts the equilibrium shape of the bubble. The Wulff construction is a classic materials science technique used to determine the equilibrium shape of a particle from the interfacial energy of grain boundaries [65,66]. It has been applied to this work because domain wall energy can be considered analogous to the interfacial energy between grains. Fig. 4.16d demonstrates this technique for a magnetic system with $\mu_0 H_x = 240mT$, $\mu_0 H_{DMI} = 300mT$, $A = 1 \times 10^{-11} J/m$, $M_s = 600kA/m$, and $K_D = 3 \times 10^3 J/m^3$. Starting with the polar energy plot, a radial line, of angle Θ, is drawn from the origin to the magnitude of the domain wall energy. A normal line is then drawn at the point. After repeating this procedure for every value of Θ the equilibrium shape of the bubble domain is formed by the minimized area between all the intersecting normal lines. Using this technique, the anomalous teardrop bubble domains have been modeled as a function of domain wall energy. These findings are evidence of the role of the magnetostatic dependent driving force towards the formation of an equilibrium shape.
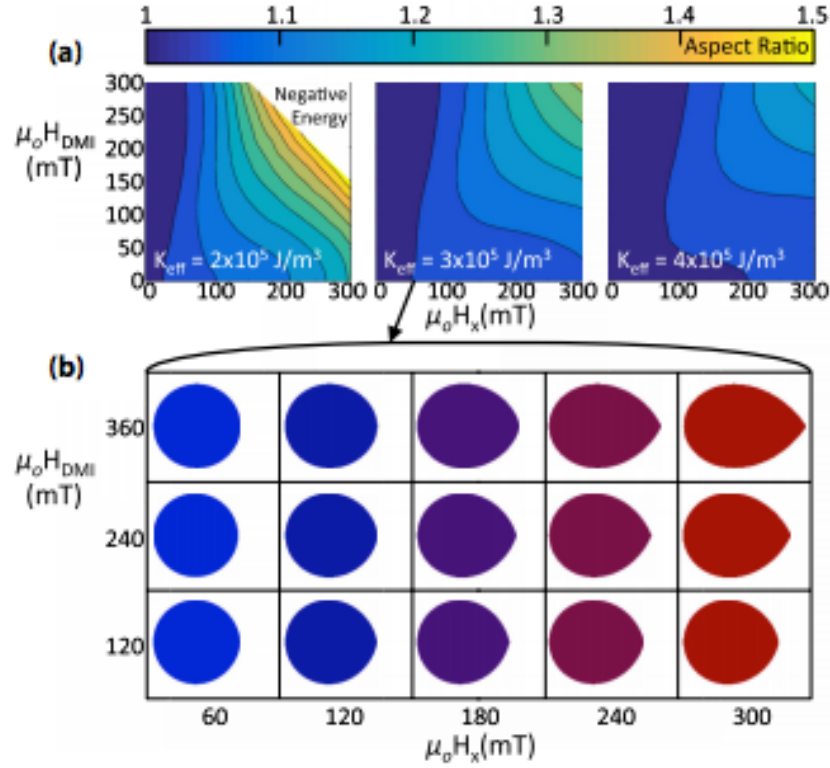
Figure 4.17: (a) Contour plots generated from equilibrium domain shapes as a function of K_{eff}, $\mu_0 H_x$, and $\mu 0 H_{DMI}$. (b) The transition from a bubble domain to a teardrop domain for a simulation with K_{eff} fixed at $3 \times 10^5 J/m^3$.

The equilibrium shape calculation was also performed at different conditions that correspond to different film properties found in literature. Most notably, the effective anisotropy (K_{eff}) has the largest contribution to the bubble shape transition. Compared to other films reported on in literature, the K_{eff} of the films in this study are noticeably smaller. We believe the smaller magnitude decreases the Bloch wall energy (σ_0) and increases the domain wall width (λ). According to Equation (4.2), the Zeeman energy terms have a bigger contribution to energy while making the Bloch wall energy and anisotropy energy term less significant. Fig. 4.17 shows the domain equilibrium shape at different magnitudes of K_{eff} and Zeeman fields ($\mu_0 H_x$ and $\mu_0 H_{DMI}$). The contour plots show the aspect ratio of the predicted equilibrium shape as a function of K_{eff}, $\mu_0 H_x$, and $\mu_0 H_{DMI}$. Aspect ratio values of 1 correspond to a circular domain while values of 1.5 correspond to a teardrop shape. The aspect ratio is shown to increase when $\mu_0 H_x$ and $\mu_0 H_{DMI}$ increase together. However, the simulations also show that only systems with lower effective anisotropies are expected

to exhbit the teardrop shape, even at high Zeeman energies.

The flattened bubble domain shapes that form at low magnitudes (Fig. 4.11) of applied in-plane fields can be expressed with modifications to the Wulff construction energy minimization technique. As shown in Fig. 4.16, the energy minimization results in two local energy minima at some Θ values. Originally, the minimization technique assumed that each orientation had an equal chance of occurring, resulting in a smooth polar energy plot. The minimization technique is modified to take the average energy of the two possible orientations and to take that value as a "pseudo-equilibrium" to be plotted in the polar energy curve. Fig. 4.18b shows that the polar energy plot exhibits a region where domain walls are expected to be metastable, evidenced by sharp changes in domain wall energy. In those metastable regions, multiple orientations of the domain wall are supported, which results in faceting. Along the side of the domain wall where this occurs, this leads to a seemingly flat region. Applying the Wulff Construction shows that the metastable domain wall energy gives rise to the flattened feature seen in the bubble domains at low H_x. As H_x increases, the region of metastable domain wall energy decreases, eventually returning to the smooth polar energy plot seen in Fig. 4.17. The trend is mirrored in the experimental results, where the domain shape has a flattened side at low values of H_x, but transitions into the teardrop shape above some H_x field. However, the anisotropy constant ($K_D > 6 \times 10^4$) required to simulate the shape transition trend is too high to be realistic. Although the teardrop shape can be explained relatively accurately, the formation of a flattened domain requires a more complicated explanation. We have shown, however, that an examination of the equilibrium domain wall energy is potentially more important for DMI characterization than previously considered. This work suggests that the domain wall velocity is the combined affect of thermally activated creep and the energetic relaxation of the domain wall towards an equilibrium shape, requiring a refined model of domain wall motion in the creep regime.
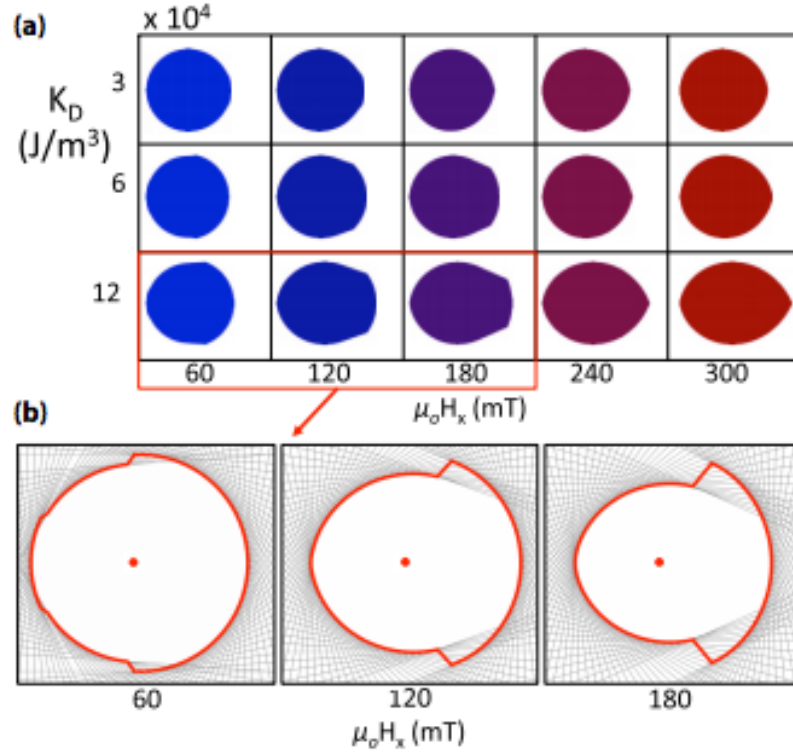
Figure 4.18: (a) Equilibrium domain shapes calculated with metastable energy considerations for $K_{eff} = 3 \times 10^5 J/m^3$.(b) Polar energy plots and Wulff Constructions showing the transition from a flattened bubble to teardrop equilibrium shape.

4.5 Dispersive Stiffness Model for Domain Wall Creep

A proposed mechanism for the modeling chiral domain wall velocity will be explored in this section by starting with the mechanisms described in the conventional creep regime model and then describing the refinements and considerations to account for anomalous behavior described in Chapter 4.4.

4.5.1 Conventional Model for Domain Wall Motion in the Creep Regime

As described earlier in Chapter 2.4.1, domain wall motion is classified in three regimes: creep, depinning, and fast flow. The three regimes are classified by the driving force applied to move the walls, relative to the critical energy barrier of the system. Like all materials magnetic films contain defects like point defects, grain boundaries, or physical surface damage. These defects become regions where domains can nucleate and domain walls will be pinned due to a lower anisotropy energy. When considering Equation (4.2), it is clear

that the total energy of a domain wall is lower when anisotropy energy is reduced. Therefore, it is energetically favorable for domain walls to stay at regions that have a lower local anisotropy or contain defects, creating a pinning effect. When a domain wall is pinned, there is a critical field (f_c), where some external driving force (magnetic field or spin current) or temperature must overcome in order to induce domain wall motion. The domain wall creep describes the regime where the applied field is lower than the critical field. The depinning state describes the regime where the applied field is equal to the critical field, depinning the domain wall from the defect sites. The fast-flow regime occurs when the applied force is much larger than the critical field, leading to the fastest domain wall motion of the three. The magnetic system in this work are tested in the creep regime, where the domain wall is in an equilibrium (ignoring thermal fluctuations) in the absence of an applied field. Thermal fluctuations and applied external fields introduce motion where the domain wall reorients in its equilibrium state until it reaches a saddle point in energy configuration. Domain walls experience a translational motion when the domain walls move from a intermediate saddle configuration into a new stable configuration [32]. Conventionally, the process is modeled with a general Arrhenius relationship given by the equation [33]:

$$v = v_0 exp(-\zeta(\frac{f}{f_c})^\mu) \tag{4.3}$$

where ζ is a constant related to the pinning potential and μ has been defined as $-1/4$ for magnetic systems with an externally applied magnetic field. Particularly, for domain walls moving in the creep regime, where motion is mostly thermally activated, the general equation can be modified to be a function of temperature, given by the equation:

$$v = v_0 exp(-(\frac{U}{kT})) \tag{4.4}$$

In this case, the activation energy, U, is the energy required to overcome a combination of domain wall elasticity and pinning forces. It has been shown that the elastic forces in a domain wall dominate at small length scales and work to maintain a shorter interface by reducing curvature. At longer length scales, pinning forces dominate domain wall creep behavior causing the roughening of domain wall profiles due to an inhomogeneous distribution
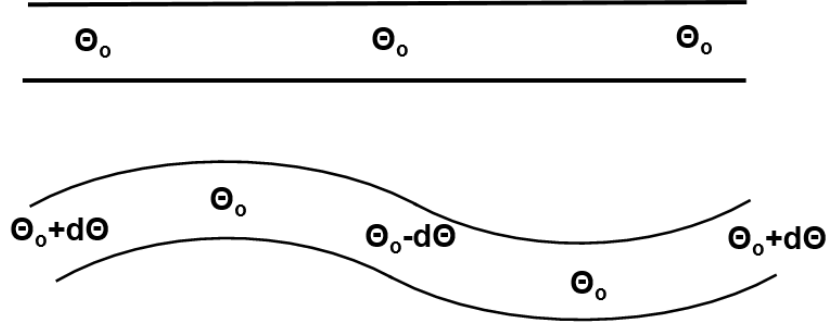
Figure 4.19: The change in equilibrium orientation along chiral domain wall due to anisotropic energies.

of pinning potentials. At these length scales, domain wall motion is defined as transitions from metastable states of low energy. As a result, the energy barrier for domain wall creep is a function of interfacial magnetic properties:

$$U \propto \frac{\lambda^{\frac{3}{4}} \varepsilon^{\frac{1}{4}} \gamma^{\frac{1}{2}} t_f^{\frac{3}{4}}}{f^{\frac{1}{4}}} \tag{4.5}$$

where *lambda* corresponds to domain wall width, ε is energy from elastic forces, γ is the energy from collective pinning forces, t_f is film thickness, and f corresponds to the driving force for domain wall motion (H_z) [67]. Since the magnetic properties are functions of static domain wall energy, the creep velocity function can be rewritten as a familiar function of domain wall energy given by Equation (4.6). [30, 63]

$$v_{DW} = v_0 exp(-\alpha H_z^{-1/4}) \tag{4.6}$$

where v_0 is the characteristic velocity fitting parameter and α is proportional to the domain wall energy parameter determined by the equation:

$$\alpha \propto \alpha_0 \left(\frac{\sigma(H_x)}{\sigma_0} \right)^{1/4} \tag{4.7}$$

where α is conventionally assumed to be proportional to the elastic energy of the domain wall [68, 69], as seen in Equation (4.7).
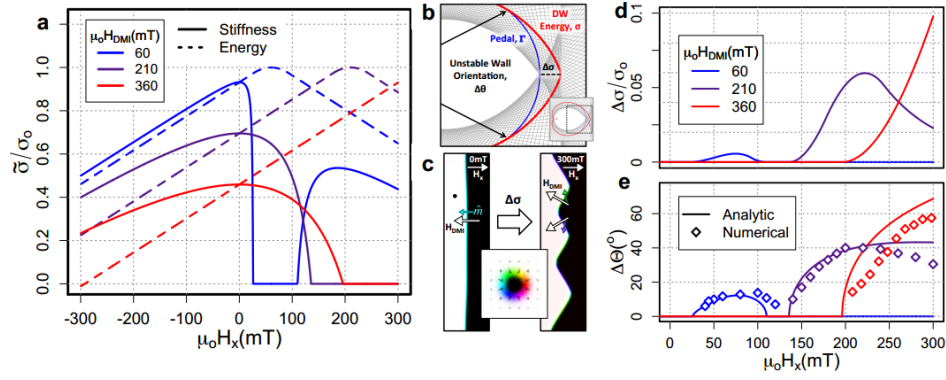
Figure 4.20: a) Comparison of domain wall surface stiffness and isotropic domain wall energy for different magnitudes of DMI. b) Wulff construction demonstrating the driving for for faceting domain wall. c) Micromagnetic simulations of the transition from a planar profile to a faceted profile as a function of applied in-plane field. d) Plot of the calculated driving force for faceting for different magnitudes of DMI in the magnetic system. e) Analytically predicted angle of faceting supported by numerical calculations. [70]

4.5.2 Dispersive Stiffness in Dzyaloshinskii Domain Walls

In conventional models, α is related to the total domain wall energy, after making the assumption that the energy is isotropic. However, with the introduction of DMI and an external magnetic field to the system, the domain wall energy is dependent on wall orientation so the isotropic assumption can no longer be made. Instead, the wall energy becomes dependent on the orientations of the local magnetic moments along the wall, making it necessary to incorporate a surface stiffness term. Pellegren et al show that the elastic energy (ε) must account for the changes in orientation along the domain wall($\tilde{\sigma}$) by applying following relationship [70] (Fig. 4.19):

$$\tilde{\sigma}(\Theta) = \sigma(\Theta) + \sigma''(\Theta) \tag{4.8}$$

where Equation (4.8) is a function of the azimuthal angle of the domain wall normal. α is then modified to account for surface stiffness:

$$\alpha \propto \left(\frac{\tilde{\sigma}}{\tilde{\sigma}_{H_x=0}}\right)^{1/4} \tag{4.9}$$

resulting in a modified creep law velocity relationship that accurately describes the velocity profile features that cannot be explained conventionally. As a consequence of the

anisotropic domain wall energy, the domain wall surface stiffness predicts sharp decreases near H_{DMI} even though domain wall energy remains symmetric, as seen in Fig. 4.19a. The negative values of stiffness correspond to the transition to a faceted wall, which was predicted thermodynamically in Chapter 4.4. Fig. 4.19b,c,d and e demonstrate the increasing driving force for a faceted domain wall profile as H_x increases, which provides us with the mechanism for the observations noted from our qualitative Kerr images and thermodynamic modeling. In addition, the correlation between that the sharp decrease in surface stiffness and a vanishing elastic response provides a mechanism to explain the reversal field observed in the experimental domain wall velocity profiles, where a faceted domain wall appears to move counterintuitively faster. Qualitatively, the anomalous behavior of the velocity profiles are not unique to bubble domains as previously shown in Chapter 4.4, but also apply to planar wall profiles (Fig. 4.21a). This suggests that the surface stiffness mechanism for domain wall creep is fundamental process. As shown in Fig. 4.21b, the elastic creep model is able to accurately repeat the horizontal shifts in the curves as well as the reversal in growth asymmetry. Fitting the experimental domain wall profile with appropriate creep parameters shows that the the refined stiffness model is still operating in the creep regime Fig. 4.21c. Using the model, experimental data sets can be fit by adjusting the parameters: $\mu_0 H_k$, $\mu_0 H_{DMI}$, Θ_o (a quantitative value for domain wall roughness), and L (pinning distribution length scale). The model has fit our experimental data of a $TaN(3nm)/Pt(2.5nm)/[Co(0.2nm)/Ni(0.6nm)]_2/Co(0.2nm)/Ta(0.5nm)/TaN(6nm)$ system to the following values: $\mu_0 H_k = 1.5T$, $\mu_0 H_{DMI} = 106mT$, $\Theta_o = 8°$, and $L = 47nm$. The model overestimates H_k, but also gives reasonable values for pinning length scale and DMI. With this model, we have found that in the low L regime, $\mu_0 H_{DMI} \sim \mu_0 H_{min}$, validating the conventional method of extracting $\mu_0 H_{DMI}$ from a velocity curve. With additional work, the model has the potential to be used to extract DMI and pinning length scales accurately, properties that are normally difficult to extract.

4.5.3 Effects of Chiral Damping on Chiral Domain Wall Mobility

Although the stiffness model for interface elasticity can recreate the anomalous features in domain wall velocity profiles, there are some characteristics that cannot be fully explained.
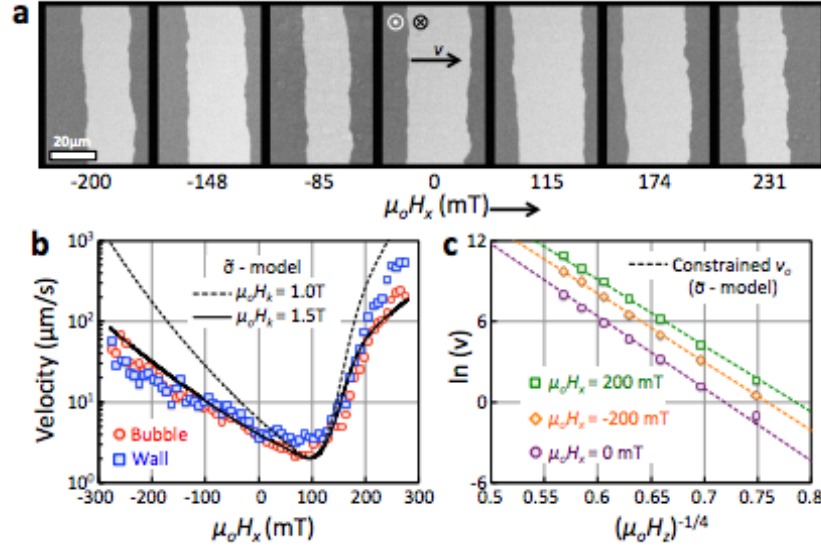
Figure 4.21: (a) Subtractive Kerr images that supplement collected bubble domain images. Identical velocity characteristic suggest that the 1D elastic string model applies to bubble domains as well. (b) Experimental data overlaid with velocity profile predicted by elastic creep model. (c) Elastic creep law fits and experimental data showing domain wall motion in the creep regime. [70]

For example, fitting the experimental data using reasonable parameters will generate the expected horizontal velocity shift and the asymmetric vertical shift in velocity. However, a consequence of the domain wall surface stiffness model is the observation that large enough in-plane fields, the driving force for faceting becomes minimal Fig. 4.20d. As a result, the qualitative features cancel out as the stiffness for both domain wall orientations ($\uparrow\downarrow$ and $\downarrow\uparrow$) converge. Based on the experimental velocity curves Fig. 4.12 where it is assumed that velocity profiles will not converge, requires the model to consider the effects of a chiral damping force in the system. Chiral damping is defined as a mechanism that arises due to the structural inversion symmetry of a system, like DMI. Essentially, the chiral damping mechanism induces the vertical asymmetric displacements seen in our experimental velocity curves and in similar systems from literature [71].

Although other possible explanantions for velocity curve asymmetry have been explored, the most compelling is chiral damping. Chiral damping is explained as a component of damping that appear in materials that do not have inversion symmetry. The Gilbert damping parameter in the LLGS equation (Equation (2.33)) can be expressed as a nonlocal second-

rank tensor from which three damping components can be extracted, isotropic damping, magnetocrystalline anisotropy damping, and chiral damping. Akosa et al shows that chiral damping has the same symmetry as the DMI and concludes that chiral damping is exhibited in materials that are noncentrosymmetric [72]. It is understood that the physical origins of chiral damping can be traced to spin-orbit coupling, dipolar coupling, and magnetic frustration. Due to its novelty, extracting the magnitude of chiral damping in materials has not been explored. However, there has been recent work suggesting a chiral damping role in chiral domain wall motion and asymmetric spin wave damping [71, 73]. Jue et al has suggested that it is a major cause of asymmetry in chiral domain wall velocity curves. By introducing an in-plane field to the magnetic domain wall, the mechanism of the chiral damping effects is extracted empirically. The chiral effects can be extracted by observing the anti-symmetric component of the velocity curves. Since chiral effects are asymmetric in nature, plotting the anti-symmetric component is a valuable indicator for identifying chiral effects (Equation (4.10)).

$$A(H_x) = ln\frac{v_{\uparrow\downarrow}(H_x)}{v_{\downarrow\uparrow}(H_x)} \tag{4.10}$$

Through a simple mathematical relation, they are able to empirically extract the the asymmetric contribution to velocity curves, inferring the strength of chiral damping in their magnetic sample, which is given by the equation:

$$\alpha_{CD} = \alpha_{CD_0} + \alpha_{CD_c} \cos\phi \tag{4.11}$$

where α_{CD_0} and α_{CD_c} are coefficients that depend on the magnetization in the domain wall and ϕ is the angle of the local magnetization with respect to the domain wall normal [71]. They have found that chiral damping scales inversely with the characteristic velocity fitting parameter, v_0, in the creep velocity equation (Equation (4.6)). For this thesis work, the effects of chiral damping are modeled by the following equation:

$$v_0(H_x) = v_0^*(1 + \alpha_{cd}cos(\phi_{eq}(H_x) - \Theta)) \tag{4.12}$$
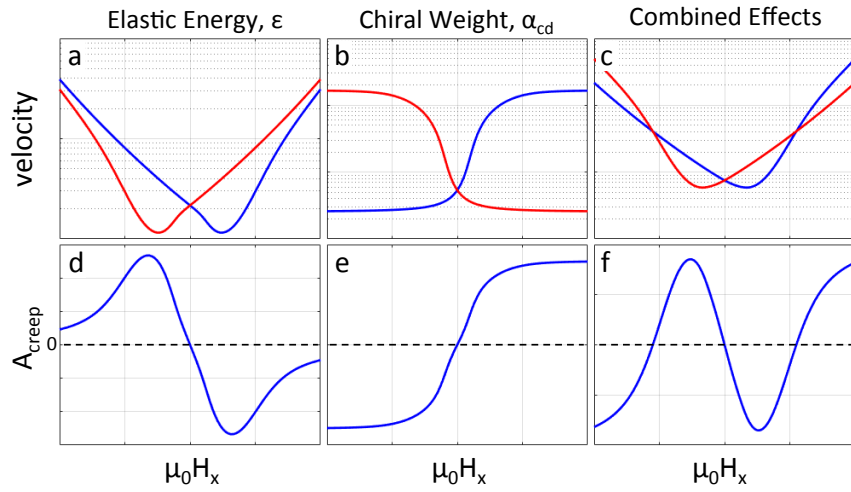
Figure 4.22: The effects of chiral energy and chiral damping terms extracted from a characteristic domain wall velocity profile.

where α_{CD} ranges from -1 to 1 and characterizes the strength of the chiral damping mechanism and Θ corresponds to the angle between the domain wall normal and applied field. With this implementation, it is possible to isolate the effects of the DMI and chiral damping on velocity profile and asymmetry from our experimental velocity profile, as seen in Fig. 4.22.

CHAPTER V

Engineering DMI and Device Performance Through Seedlayer Composition

In Chapter IV, the DMI originating from the interface between a Pt seedlayer and a Co/Ni is characterized and discussed in detail. However, it has been shown in theory that other transition metal interfaces are also capable of generating a significant DMI effect [74]. The effect of different seedlayers has also been shown experimentally in recent works [19, 20, 25–27]. Most of the work done on chiral magnetic materials have been in an effort to characterize their potential for domain wall devices. Much less work has been spent trying to tune the DMI properties of a material, although Mankovsky et al and Hanke et al have demonstrated, computationally, the effects of intermixing on DMI [75, 76]. There has been some engineering in this field involving characterizing the effect of seed layer thickness and magnetic layer thicknesses on DMI. In this work, we hope to explore the effects of varying composition in a seed layer in an effort to tune DMI in a $Pt/[Co/Ni]/Co/Ta$ system.

5.1 Motivation for Alloying Seedlayers

The motivation for investigating seedlayer alloying comes from the prevalence of alloying in magnetic systems. There are many examples of alloying materials in order to optimize their magnetic properties depending on their applications. Some well known examples in industrial applications are AlNiCo, Si-Fe Steels, and Permalloy, all which were developed in order to satisfy a property that was not addressed by using pure magnetic metals (Fe, Co, Ni, etc). $AlNiCo$, for example, is an alloy constructed of aluminum, nickel, and cobalt that is shown to have a coercivity much higher than the individual elements themselves, making

them valuable for applications that require a strong permanent magnet. The Si-Fe steels and Permalloy are both alloys that contain iron, silicon, and iron, nickel, respectively. Both alloys show high magnetic permeablilty, making them important for transformer and power generation applications. More advanced magnetic alloys have been developed and they are prevalent in industry and academic literature. Alloys such as FINEMET, HITPERM, and NANOPERM have been developed independently in order to provide high permeability, low hysteretic losses, large saturation magnetizations, remnant magnetizations, and a high curie temperature [77]. All three alloys are different combinations of transition metals to obtain properties similar to Si-Fe steels and Fe-Co alloys in terms of permeability and induction values. For example, Willard et al has shown that HITPERM (developed at CMU) have a high permeability at $2kHz$ with a loss value of $1W/g$ at $B_s = 510kG$ and $f = 510kHz$, important for applications that require soft magnets that can operate at high temperatures [78].

In addition to power applications, alloying has also been integral to the success of high density storage media. Some well known examples include $FePt$ and $CoPt$ alloys, both which have been integral in increasing the density of storage in perpendicularly oriented magnetic thin films. Yang et al has shown that $L1_0$ FePt exhibit high enough coercivity, magnetocrystalline anisotropy, and small enough grain sizes to be considered a stable, high-density recording medium [79]. Jeong et al has explored the relationship between thicknesses and textures in $CoPt$ and $FePt$ and their magnetic properties, relevant for optimizing coercivity and anisotropy direction for high density storage media [80, 81]. Alloys are ubiquitous in magnetic technologies and the variance in alloy compositions makes it challenging to characterize and optimize magnetic systems.

Unsurprisingly, the composition of magnetic alloys, in general, have significant effects on magnetic properties. Many studies have shown that magnetic properties of an alloyed system are not directly proportional to composition. For example, $CoPt$ exhibits a varying magnetocrystalline anisotropy as a function of Pt composition in the alloy, a phenomenon studied by Huan et al [82]. $SmTiFe_{11-x}Co_x$ alloys, used in applications that require a

permanent magnet, shows similar non-linear trends in saturation magnetization and Curie Temperature where they are functions of the Co concentration in the alloy [83]. At the atomic level, $Fe - Co$ alloys exhibit a magnetic dipole moment that is not linearly related to composition. In fact, magnetic dipole moment peaks when Co makes up ∼30 atomic percent of the alloy [77]. These discoveries make it reasonable to assume that DMI is subject to similar composition dependent trends that other magnetic properties exhibit, making it interesting to study the effects of alloying on DMI.

Recent computational work by researchers in this field have explored DMI in magnetic multilayers through first principles methods. Through their computational modeling, they have attempted to gain insight into the correlations between electronic structure and the induced DMI in a magnetic system. As such, many parameters have been explored, including thickness, interface properties, structure asymmetry, and composition. Belabbes et al showed in their work that the interfacial DMI in a material can be attributed to the interaction between the electrons in the 3d orbitals of ferromagnets and the electrons in the 5d orbitals of transition metals. Essentially, the sign and magnitude of DMI are directly correlated to the 3d-5d hybridization in magnetic multilayers. Using Hund's Rules, they show that for ferromagnetic materials that have unoccupied orbitals, a large DMI contribution is expected because they allow for more spin-flip excitations. Mn ($3d^5$), for example, was shown to contribute a large DMI because due to its electron configuration, all the spin-down channels are unoccupied. This trend appears to be true for all interfaces between ferromagnetic materials and 5d transition metals (except Au), demonstrated by their first principles calculations of DMI [74]. Computational work by Hanke et al further supported the significance of 3d-5d orbital hybridization for inducing DMI in heavy metal/ferromagnet interfaces. They were able to demonstrate a complex relationship between DMI and composition through ab initio calculations of band structure. Their simulated nine-layer structure comprised of a Pt (111) substrate and a Co monolayer followed by a capping layer of varying (Pt, Ir, Au) composition. By simulating the complex band structure (Fig. 5.1), they have shown that symmetric multilayer structures ($Pt/Co/Pt$) have symmetric band structures, while their asymmetric structures ($Pt/Co/Ir$ and $Pt/Co/Au$) demonstrate asymmetric band structures. By
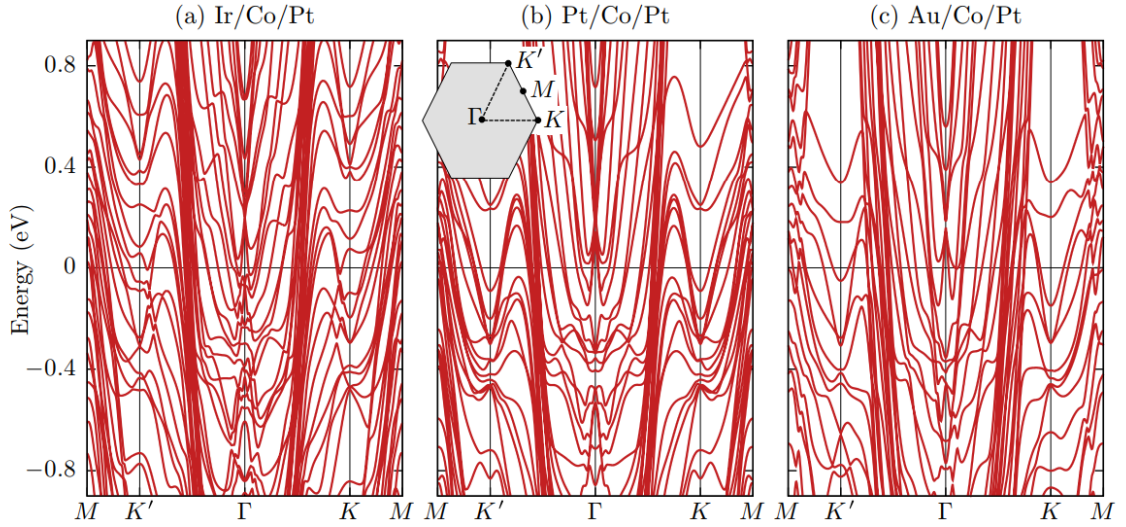
Figure 5.1: Electronic band structure in three heterostructures along high symmetry lines. [75]

calculating the DMI spiralization from occupied bands, they can show how electronic structure can influence total DMI. Their findings are in agreement with theoretical expectations where they show that in films with symmetric band structures, the calculated DMI contributions cancel exactly. On the other hand, in the asymmetric films simulated, there is clearly a net effect, resulting in a quantifiable DMI. From there first principles calculations of band structure, they demonstrate a nonlinear change in DMI magnitude and direction as the composition in the capping layer changes from $Ir \rightarrow Pt \rightarrow Au$ (Fig. 5.2). In both of these studies first principles computations have demonstrated a theoretical basis for tuning DMI in magnetic multilayers through composition for the purposes of engineering magnetic systems for practical applications and research.
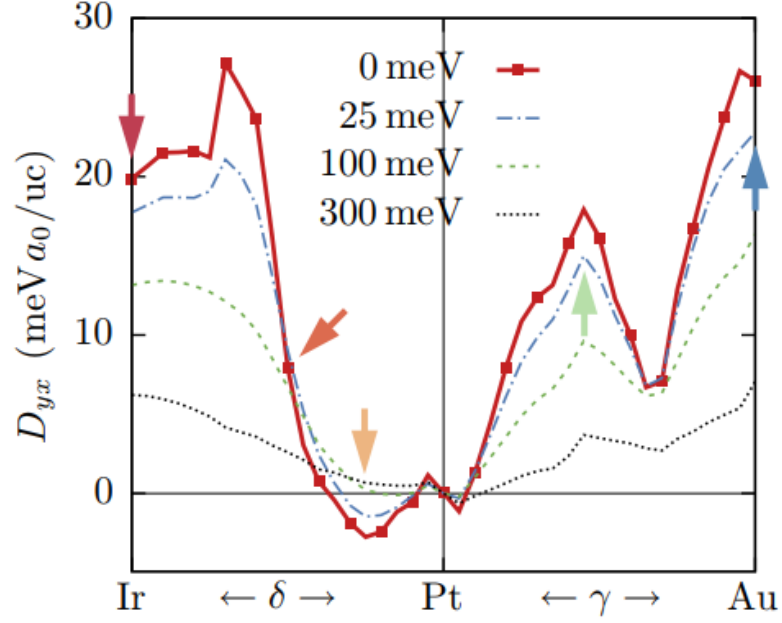
Figure 5.2: DMI magnitude and orientation as a function of capping layer composition. [75]

5.2 $Pt/Pt_xIr_{1-x}/[Co/Ni]/Co/Ta$ Magnetic Multilayer

The heavy metal seedlayer has predominantly been a pure element such as Pt, Ir, W, or Ta, but the range of possible alloy combinations remain largely unexplored. The ability to tune DMI via composition without compromising other magnetic properties is critical for engineering future devices. In this section, we explore the magnetic properties of a thin film made with a seedlayer composed of Pt and Ir. Ir is chosen because the material has been studied and has an expected DMI. It is known to have a significant DMI magnitude, like Pt, but with a vector pointing in the opposite direction [20]. Therefore, we reason that a compositional gradient made of Pt and Ir should have a subtractive effect to DMI as the content of Ir increases. Starting with the system that we are already familiar with in Chapter IV, we modify the seedlayer to create an Ir composition gradient, resulting in a thin film composition of: $TaN(3nm)$ / $Pt(3.5nm)$ / $Pt_xIr_{1-x}(1.2nm)$ / $[Co(0.2nm)/Ni(0.6nm)]_2$ / $Co(0.2nm)$ / $Ta(0.8nm)$ / $TaN(6nm)$, where x varies from 0 to 1. In addition to the composition varying thin film, variations of the film with pure seedlayers are fabricated for characterization, for consistency between samples. A

Figure 5.3: Pt-Ir alloy seedlayer film stacks deposited for film and device level characterization.

pure Pt and Ir seedlayer film are also explored: $TaN(3nm)$ / $Pt(3.5nm)$ / $Pt(1.2nm)$ / $[Co(0.2nm)/Ni(0.6nm)]_2$ / $Co(0.2nm)$ / $Ta(0.8nm)$ / $TaN(6nm)$ and $TaN(3nm)$ / $Pt(3.5nm)$ / $Ir(1.2nm)$ / $[Co(0.2nm)/Ni(0.6nm)]_2$ / $Co(0.2nm)$ / $Ta(0.8nm)$ / $TaN(6nm)$ (Fig. 5.3). A composition variation is deposited on our sample using the technique outline in Chapter 3.2 Fig. 3.8. By depositing each species monatomically, we are able to fabricate an alloyed seedlayer with a composition that varies by position. With the known deposition rates, we can map out the composition of a deposited species based on its position on the $3in.$ wafer.

5.2.1 Film Structure and Magnetic Properties

5.2.1.1 X-Ray Diffraction (XRD) Characterization

XRD is performed to insure that the (111) crystallographic orientation is maintained with the addition of Ir. Maintaining the (111) texture is critical because [Co/Ni] grown in the (111) direction displays perpendicular magnetic anisotropy. Efforts to promote the Ir (111) texture as a seedlayer has largely been unsuccessful. Instead, a Pt layer is grown first in order to establish the desired orientation, since the conditions for producing (111) texture in Pt has been successfully demonstrated (4.2). After growing Pt, Ir is sputtered directly on top of the layer serving as the actual seedlayer for the magnetic film. The main concern is that the (111) texture produced by the initial layer of Pt is maintained throughout the whole structure. Fig. 5.4 are XRD patterns obtained from samples that have a successfully

deposited layer of Ir on Pt and TaN to insure that (111) texture retention. The sample shown has the following composition: $TaN(3nm)$ / $Pt(2.5nm)$ / $Ir(10.0nm)$ / $TaN(6nm)$. Pt is expected to exhibit a peak at $2\theta = 39.750°$. The Ir (111) peak is expected to appear at $2\theta = 40.671°$, which overlaps with the Pt peak. There is a main peak located at $2\theta = 40.250°$, in between the two expected peaks, which may indicate strain in the deposited layers due to mismatch lattice parameters. Fig. 5.5 is the rocking curve test performed at $2\theta = 40.250°$. The resulting curve has a FWHM of $5.130°$, indicating a layer with good, consistent texture. Additional XRD characterization was performed to ensure that the Co magnetic layer grown on the Ir seedlayer also maintains the (111) texture. Fig. 5.6 show XRD patterns for a sample with a thickness varying layer of Co deposited on an Ir seedlayer with the composition: $TaN(3nm)$ / $Pt(2.5nm)$ / $Ir(2nm)$ / $Co(x)$ / $TaN(6nm)$, where x corresponds to a linear thickness gradient from $5nm$ to $10nm$. The resulting XRD patterns are similar to the XRD patterns seen in Chapter 4.2 and Fig. 4.7. The Pt and Ir peaks are located at $2\theta \sim 40°$, as expected. The Co peaks appear around $2\theta \sim 44°$ and seem stay constant as the thickness of Co increases (Fig. 5.6). Similar to Fig. 4.7, we believe there is some stress related to the lattice mismatch between the two species. Nevertheless, the results suggest that our procedure to grow (111) magnetic layers on top of Ir theoretically produces thin films with perpendicular magnetic anisotropy.

5.2.1.2 Magnetic Characterization of Pt-Ir Alloyed Seedlayer Thin Films

AGFM and VSM magnetic measurements are carried out to characterize the magnetic properties of the thin films. The XRD measurements show that the system can support perpendicular magnetic anisotropy, but optimizing the structure requires more fine tuning of the deposition procedure. As mentioned previously, $TaN(3nm)$ / $Pt(3.5nm)$ / $Pt_xIr_{1-x}(1.2nm)$ / $[Co(0.2nm)/Ni(0.6nm)]_2$ / $Co(0.2nm)$ / $Ta(0.8nm)$ / $TaN(6nm)$ is constructed for this study. We hope to show that the composition of the seedlayer has little effect on the magnetic properties of the sample. Fig. 5.8 and Fig. 5.7 are representative magnetization curves taken using the AGFM. AGFM characterization reports a coercivity of $\mu_0 H_c \sim 100Oe$ and an anisotropy field of $\mu_0 H_k \sim 13kOe$. Although individual samples vary in exact magnitudes measured, the shape of the curves remain the same. Measure-
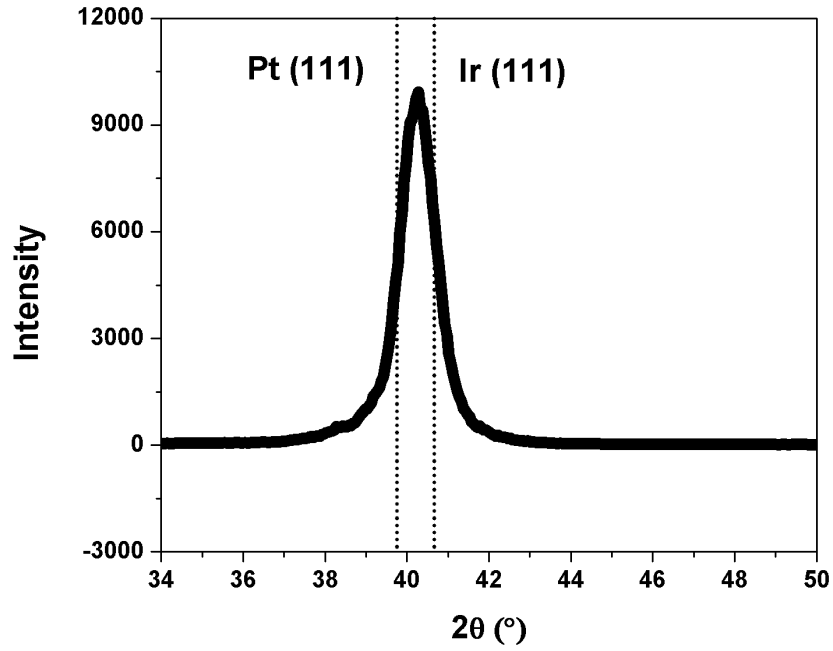
Figure 5.4: XRD spectra characterizing a *Pt* and *Ir* (111) thin film. Theoretical *Pt* and *Ir* (111) peak indicated.
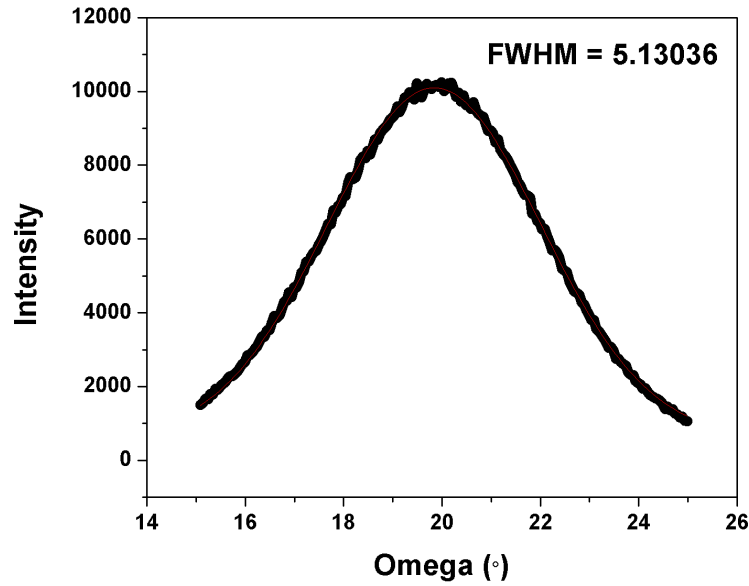
Figure 5.5: Omega rocking curve at $2\theta = 40.250°$ and the observed FWHM for the *Ir* peak.

ments in the AGFM are not as reliable as the applied field approaches the maximum field the tool can produce. So in addition to the magnetization curves, the VSM also provided
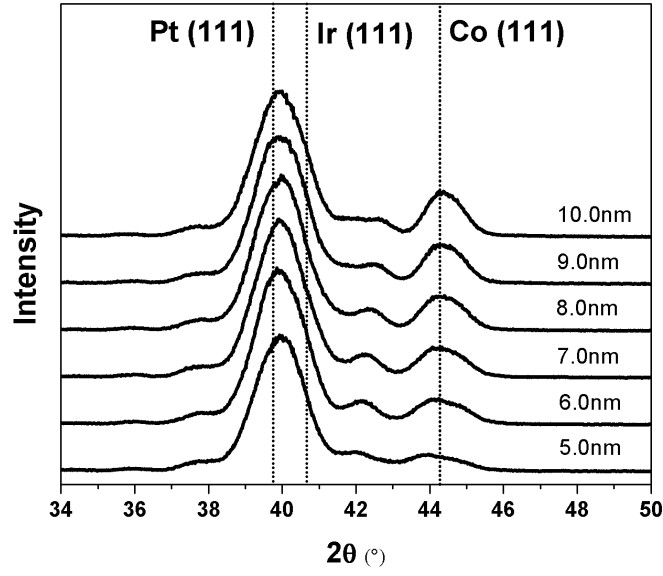
Figure 5.6: Offset XRD spectra characterizing the $Pt/Ir/Co$ structure as a function of Co thickness.

an accurate measurement of saturation magnetization: $M_s \sim 645 kA/m$. The samples show perpendicular anisotropy as well as the large enough anisotropy field necessary for films with smooth domain formation. Fig. 5.7 shows the measured anisotropy field for various pieces along the composition gradient. There are some variations, but $\mu_0 H_k$ remains consistent across the substrate. Based on these findings, we conclude that the magnetic properties are similar to the properties of the sample examined in Chapter IV, resulting in similar values of domain wall width (λ), K_D, K_{eff}, and σ_0.

5.2.2 DMI Characterization Using Kerr Microscopy

Like the samples tested in Chapter 4.3, the $Pt - Ir$ alloy samples are characterized by performing field driven asymmetric domain wall growth experiments. The fabricated $Pt_x Ir_{1-x}$ / $[Co/Ni]$ / Co /Ta samples are selectively damaged by a Ga+ ion beam in order to create domain nucleation sites with lowered anisotropy energy. $1.0cm$ x $0.5cm$ strips are cut away from the full $3in$ substrate to obtain numerous samples, each with a $\sim 10\mu m$ wide area milled away at their centers. A circular domain is nucleated with a short $\mu_0 H_z$ pulse, represented by the center gray region in the representative MOKE subtractive image in
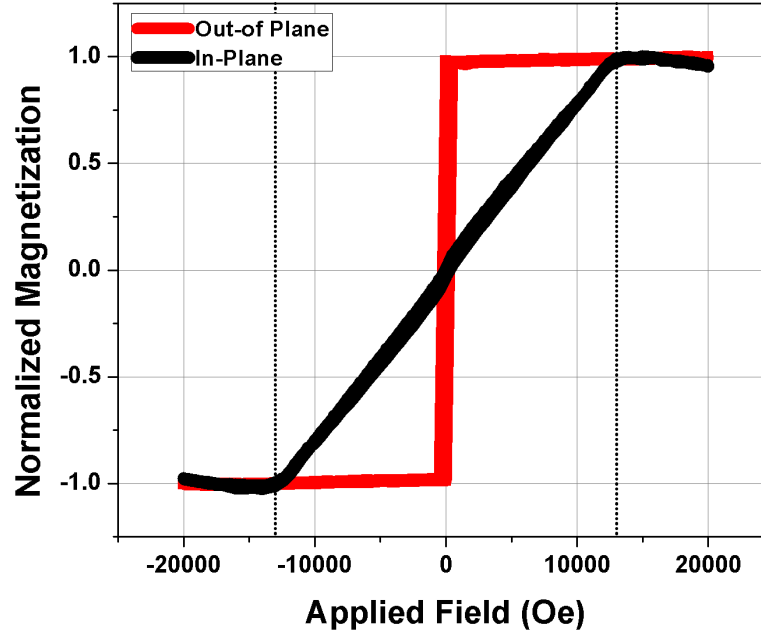
Figure 5.7: Magnetization loops along easy (red) and hard (black) axes of TaN / Pt / Ir / [Co/Ni] / Co / Ta / TaN filmstack. Measured anisotropy field of $H_k \sim 13kOe$.

Fig. 5.10. Afterwards, pulses with a constant magnitude of $\mu_0 H_z$ are applied to promote domain growth, represented by the white region in Fig. 5.10. White contrast areas are regions where the domain points in the +Z direction. Gray contrast areas depict domains pointing in the -Z direction. The domain at the center of the bubbles point in the +Z direction, but are depicted gray in the subtractive images because they are the point of origin.

Fig. 5.11 is a series of MOKE images gathered by pulsing the nucleated domains with $\mu_0 H_z$ fields. It was found that smoother velocity curves could be obtained using a $\mu_0 H_z$ pulse with a higher magnitude, mitigating the effect of the films' pinning distribution. Therefore, the bubble domains are grown asymmetrically by applying a $\mu_0 H_z = 7.00mT$ field at various pulse lengths for a sweep of $\mu_0 H_x$ fields. There is an inconsistent range of domain sizes due to the various pulse lengths applied to accommodate for the limited area of the viewing window provided by the microscope. The subtractive MOKE images show the formation of the flattened elliptical shape and its transition into a teardrop shape with the increase in external $\mu_0 H_x$, similar to the film discussed in 4.3. In addition, the transition of the
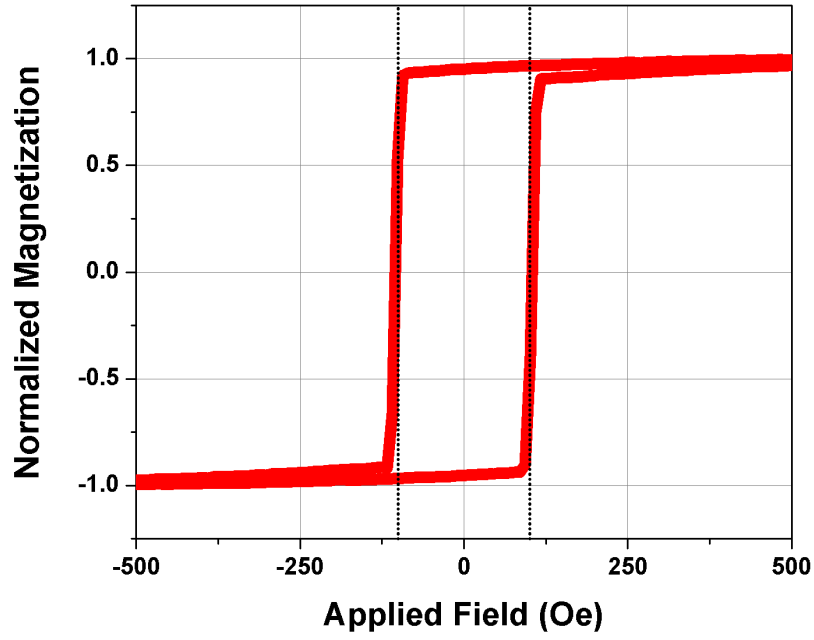
Figure 5.8: Magnetization of TaN/Pt/Ir/[Co/Ni]/Co/Ta/TaN filmstack along easy axis. Measured coercivity of $H_c \sim 100 Oe$.
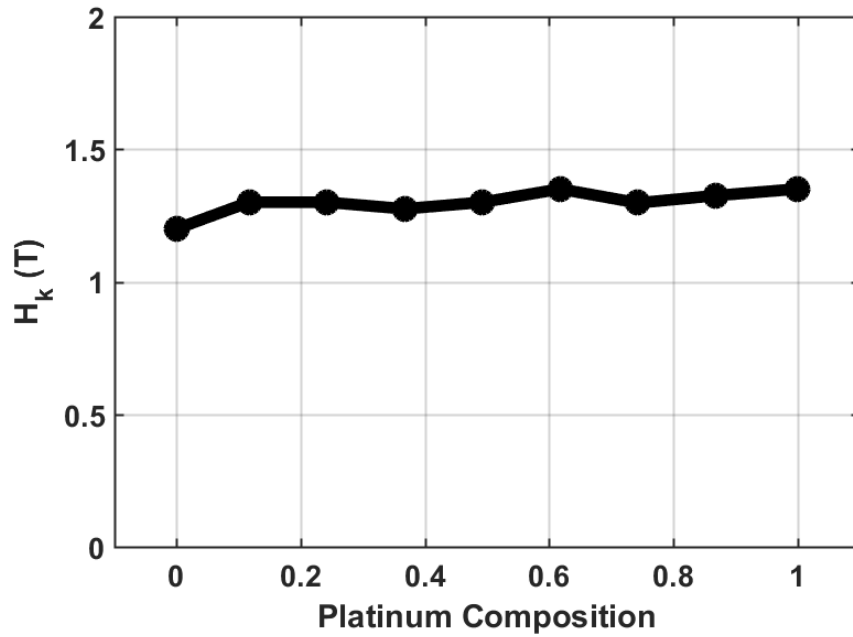
Figure 5.9: Magnetic anisotropy (H_k) as a function of platinum composition in the seedlayer.

shape seems vary from sample to sample. Fig. 5.11 shows that as the Pt content of the sample increases, the transition from a elliptical domain shape requires an increasing applied

Figure 5.10: Example MOKE image of a bubble domain for Pt-Ir alloy seedlayer films.

$\mu_0 H_x$ field. Starting with the Ir-rich sample, the transition to the teardrop shape happens almost immediately, at low $\mu_0 H_x$ fields. However, as the Pt content increases, the diagram illustrates a horizontal shift of the field where the teardrop shape is first seen. From the earlier discussion about the driving force for domain wall morphology, this is qualitative evidence that DMI is changing in response to the changing composition. In Chapter 4.4, the domain shape transition was discussed in more detail and it was suggested that a larger DMI was one of the driving forces for the formation of the teardrop domain. However, we see here that the teardrop domain, evidently, forms even for samples expected to have lower DMI (Ir-rich samples). The Ir rich films show a faster transition to the teardrop domain compared to the films with more Pt. This supports the modeling shown by Pellegren et al, where it was found that films with lower DMI tends to start faceting at lower in-plane fields than films that have higher DMI [70]. The flat elliptical shape is more prevalent in films with higher Pt content, which suggests that the metastable formation of facets along the domain wall is more likely. It appears that there are fewer regions where metastable walls can form in Ir-rich samples than in Pt-rich samples. It is likely that the seedlayer composition has a significant effect on DMI, domain wall dynamics, and domain wall energy energy as
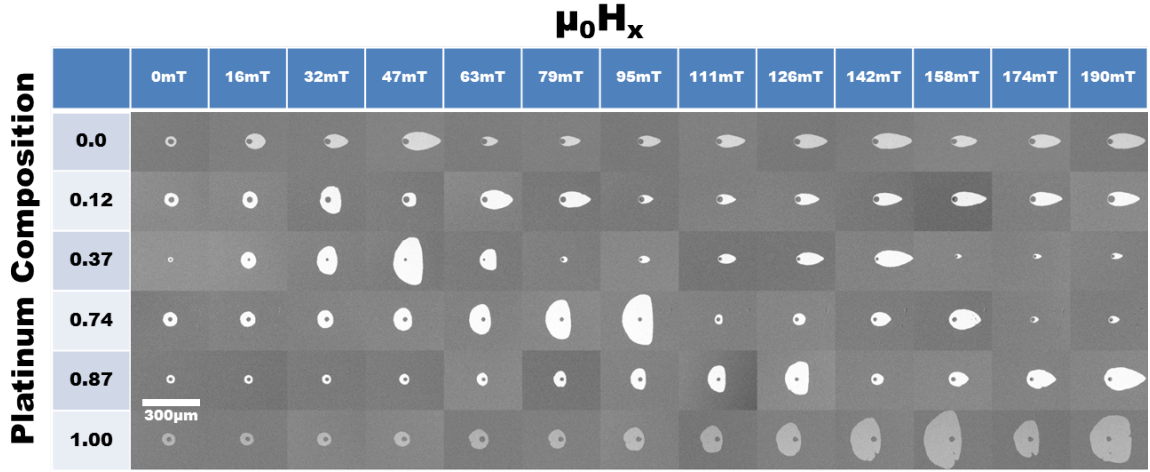
Figure 5.11: Series of MOKE images illustrating the magnetic domain shape as a function of composition and $\mu_0 H_x$. (White: Domains point in +Z. Gray: Domains point in -Z. Center: Domains point in +Z.)

previously hypothesized.

5.2.3 Effects of $Pt - Ir$ Alloy Seedlayer Composition on DMI

5.2.3.1 Applying the Dispersive Stiffness Creep Model to Extract DMI from Magnetic Multilayers

We now move on to discuss the experimental domain wall velocity profiles gathered from the $Pt_x Ir_{1-x}$ / $[Co/Ni]$ / Co / Ta samples. The refined model for Dzyaloshinskii DW creep was used to fit experimental measurements of asymmetric domain growth in Co/Ni multi-layers grown on Pt-Ir alloy seedlayers. The model incorporates elastic energy of the domain wall based on its dispersive stiffness [70] and also allows for a chirality dependent prefactor that would occur in the case of chiral damping given by

$$v_0(H_x) = v_0^*(1 + \alpha_{cd}cos(\phi_{eq}(H_x) - \Theta)) \tag{5.1}$$

where α_{cd} is a parameter from -1 to 1 that characterizes the weight of this effect - hereafter referred to as the chiral weight. ϕ_{eq} is the equilibrium internal magnetization orientation with respect to H_x as calculated in Pellegren et al [70]. v_0^* is the attempt frequency absent any chiral effects. For calculations of v_0, we only consider the case of $\Theta = 0$ or π to account for fits to the left and right velocities of the bubble domains. The velocity curves have been fit to the creep velocity equation discussed in Chapter 4.5:
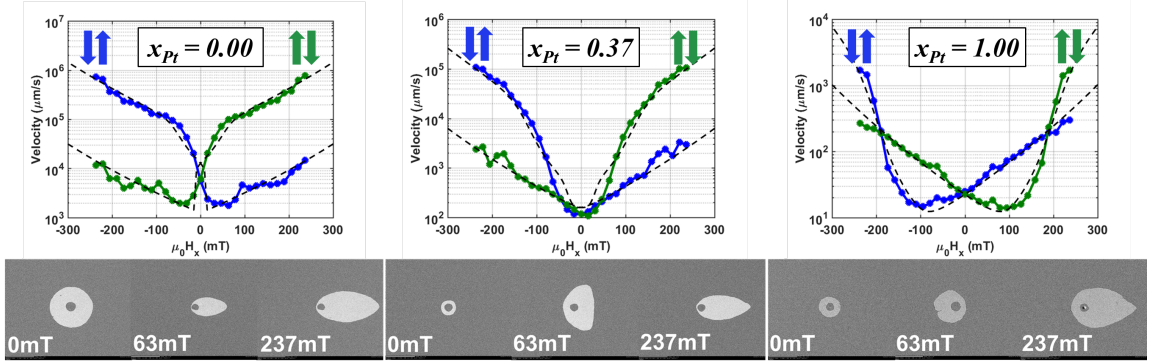
Figure 5.12: Experimental v vs. $\mu_0 H_x$ for seedlayers with varying x_{Pt} with representative MOKE images. Dashed lines are fits from Equation (5.2). The center grey of the Kerr images represent the initial bubble shape while the white region is the domain after growth under both $\mu_0 H_x$ and $\mu_0 H_z$, which was fixed at 7 mT

$$v_{creep} = v_0(H_x)exp\left[\kappa\frac{\tilde{\sigma}(H_x)}{\tilde{\sigma}(H_x=0)}H_z^{-1/4}\right] \tag{5.2}$$

where v_0 is the creep velocity prefactor constant and κ (previously described as α_0 in Chapter 4.5)is a creep scaling constant that does not depend on H_x. $\tilde{\sigma}$ is calculated using the dispersive stiffness model of Pellegren et al. in the limit of a vanishingly small deformation lengthscale, L as justified later [70]. The effects of elastic energy and chiral weight on the shape of velocity curves is shown qualitatively in Fig. 4.22. The asymmetric component,

$$A_{creep} = \ln(v_{\uparrow\downarrow}/v_{\downarrow\uparrow}) \tag{5.3}$$

, is included to further highlight experimental signatures associated with the different mechanisms. ($v_{\uparrow\downarrow}$ and $v_{\downarrow\uparrow}$ are the domain wall velocities, where the magnetization transitions from up to down and down to up, respectively. In the case where only elastic energy is considered, $v_{\uparrow\downarrow}$ and $v_{\downarrow\uparrow}$ converge (i.e. $A_{creep} = 0$) as $H_x \to \infty$. For a non-zero α_{cd}, A_{creep} saturates when $H_x > H_{DMI} + H_{DW}$ where H_{DW} is the DW anisotropy field. The experimental velocity curves are fit to the dispersive stiffness model by using automated fitting routines that solve non-linear, least squares fitting problems, in order to extract the key parameters necessary to draw conclusions about DMI and chiral damping.

Fig. 5.12 shows representative velocity profiles gathered from samples with a different seed-
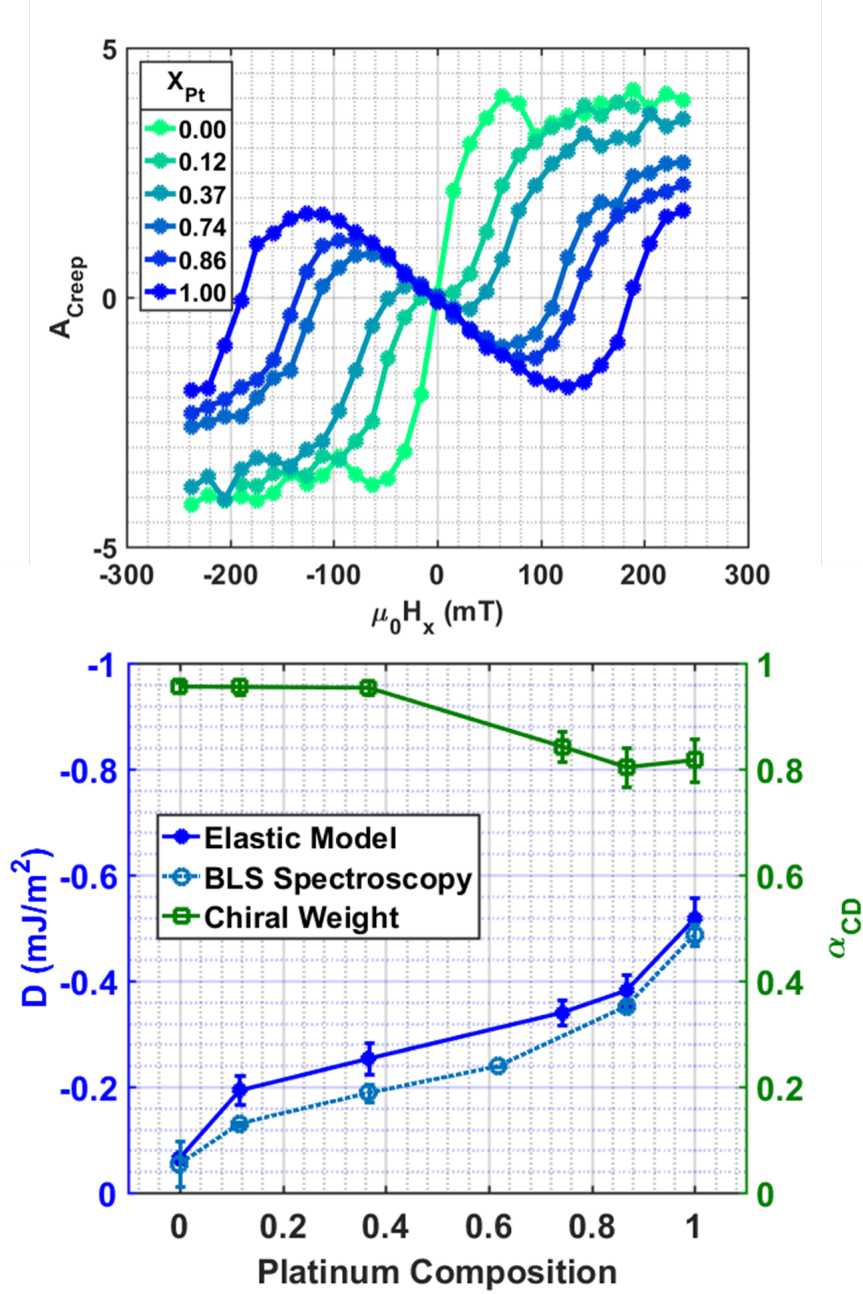
Figure 5.13: a) A$_{creep}$ vs. $\mu_0 H_x$ as a function of X$_{Pt}$. b) Extracted values of D and α_{cd} vs X$_{Pt}$ based on fits to (a). Closed blue (dark) circles represent fits extracted from the elastic domain wall model. Open blue (light) circles represent D values characterized using the Brillouin light scattering spectroscopy technique demonstrated by Nembach et al [52].

layer compositions as a function of in-plane field (H_x) and seedlayer composition with the corresponding v vs H_x curves. As seen in previous studies, the domain shape is highly non-elliptical evolving from a flattened shape at low field to a teardrop shape at higher field [62,63,84]. The field at which this occurs is found to be directly related to the amount

of Pt in the seedlayer (Fig. 5.11). The films with the pure Pt seedlayer retains the characteristics that were noted in Chapter 4.3. The velocity curve shows significant asymmetry resulting in a crossover of preferential growth. There is also horizontal shift in the velocity curve expected for films with significant DMI. As the Pt content decreases we see a shift in $\mu_0 H_{DMI}$, as expected. The velocity minima shifts towards the origin indicating a decrease in DMI. Because Ir has a DMI vector point that points in the opposite direction, a subtractive effect in the alloy is expected. From a conventional understanding of domain wall behavior, the horizontal shift can be attributed to a change in DMI of the system. Another feature worth noting is the fact that $\mu_0 H_{DMI}$ is expected to switch signs between the pure Ir seedlayer and the pure Pt layer, because the minimums of the velocity curves change sign with composition.

To gain more insight about the effect of composition on DMI, it is necessary separate the effects of elastic energy and chiral weight by examining the shape of v vs H_x and the calculated A_{creep} (Fig. 5.13). In all cases, the curve is highly asymmetric about a minimum velocity with the Pt rich cases exhibiting a reversal of the preferred growth direction, which is indicated by the intersection of the respective curves in Fig. 5.12 and by the zero crossing of A_{creep} in Fig. 5.13a. As identified previously, a change in sign of A_{creep} at non-zero H_x could be explained using a larger deformation lengthscale, L, in the dispersive stiffness model [70]. However, the observation that A_{creep} tends to saturate rather than return to zero suggests this is not the case. Therefore, we limit our fitting to the case of L $\rightarrow$ 0, which is consistent with the expectation that pinning sites in sputtered thin films are densely distributed. We note that as the composition shifts from $x_{Ir} = 0$ to 1, the minimum in velocity shifts towards $H_x = 0$ and changes sign near $x_{Ir} = 0.25$. However, as the creep fits show, D does not actually change sign and only approaches 0 for the case of pure Ir. This result is in stark contrast to the aforementioned creep models based only on the wall energy, which would have given the incorrect sign of D in this range [26, 31]. Even as D decreases with increasing x_{Ir}, the asymmetry of the curve is preserved suggesting that its origin is not exclusively due to iDMI. Indeed, A_{creep} appears to saturate in all cases even though its magnitude is reduced for increasing Pt content. The results of the fit to the velocity curves

are shown in Fig. 5.13b where it is evident that significant α_{cd} is needed to explain the data of Fig. 5.12 and Fig. 5.13a and dominates the trend for large X_{Ir}.

5.2.3.2 Chiral Damping in [Co/Ni] Magnetic Multilayer Systems

To further examine the impact of chiral weight and iDMI via the elastic energy, we have prepared films having Pt/[Co/Ni]$_2$/Co/Ir and Ir/[Co/Ni]$_2$/Co/Pt stacking sequence with velocity curves and asymmetry shown in Fig. 5.14. We note that the magnitude of D measured here should not be compared with the results tabulated in Fig. 5.13 because we have significantly increased the effective magnetic layer thickness by replacing the Ta cap (which creates a magnetic dead layer) with either Pt or Ir (both known to have a proximity induced magnetization [11]). Indeed, we see that the sign of D is reversed between these two cases with comparable magnitudes as expected. The Pt seed/Ir cap favors left-handed Néel walls ($D = -0.313mJ/m^2$) and the Ir seed/Pt cap favors right-handed Néel walls ($D = 0.214mJ/m^2$). It is interesting that despite the expected change in sign of D, α_{cd} remains nearly the same ($\alpha_{cd,Pt-seed} = 0.41$, $\alpha_{cd,Ir-seed} = 0.58$). If α_{cd} depended exclusively on the elements present and interface orientation, we should see a change in sign upon reversal of the film stack. The absence of this reversal suggests that there could be a contribution to the chiral weight that is intrinsic to the Co/Ni stack even though it is nominally symmetric. It is conceivable that the Co/Ni/Co/Ni/Co film stack itself could be structurally asymmetric if the lattice evolves through the thickness and/or the top and bottom Co/Ni interfaces are not identical. This assertion requires further investigation as it is also possible that the chiral weight contributions from Pt and Ir change when used as seed vs cap layers.

5.2.3.3 Brillouin Light Scattering Spectroscopy Characterization

Brillouin Light Scattering spectroscopy (BLS) was also used to establish an independent measure of the magnitude of the DMI. Damon-Eshbach spin-waves experience a non-reciprocal frequency-shift given by the relationship [52]:

$$\Delta f_{DMI} = |\frac{g^{\parallel}\mu_B}{h}|sgn(M)\frac{2D}{M_s}k \tag{5.4}$$
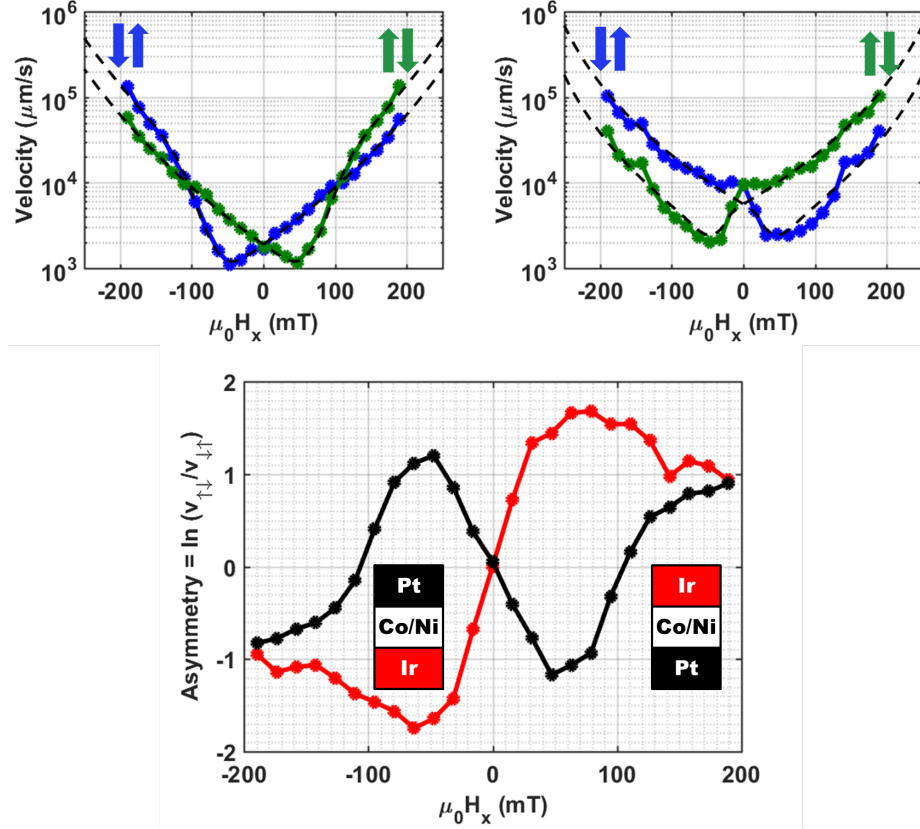
Figure 5.14: Experimental velocity vs. $\mu_0 H_x$ for samples grown with a) Pt seedlayer/Ir capping layer and b) Ir seedlayer/Pt capping layer. c) A_{creep} vs $\mu_0 H_x$ for calculated from (a) and (b)

in the presence of DMI. $g^{\|} = 2.19$ is the spectroscopic splitting factor [85], μ_B the Bohr Magneton, h Planck's constant and $\mathbf{k}$ is the spin-wave wavevector with $|k| = 16.7 \mu m^{-1}$. The spin-wave frequency for the two opposite directions of the magnetization was measured to determine Δf_{DMI} for each sample, as seen in Fig. 5.15. BLS measurements show, D does not change sign and approaches 0 for the case of pure Ir, a result that is in remarkable agreement with the D values obtained using a refined stiffness creep velocity model (Fig. 5.13b). Using BLS independently allowed us to verify and demonstrate the effectiveness of a high throughput Kerr Microscopy characterization technique for finding interfacial DMI. We have shown a monotonic increase of D with X$_{Pt}$ in Pt$_x$Ir$_{1-x}$ seedlayer alloys. The ability to tune iDMI via Pt-Ir composition and through reversal of Pt:Ir stacking sequence as demonstrated here provides new guidance for the design of film stacks in future spintronic applications.
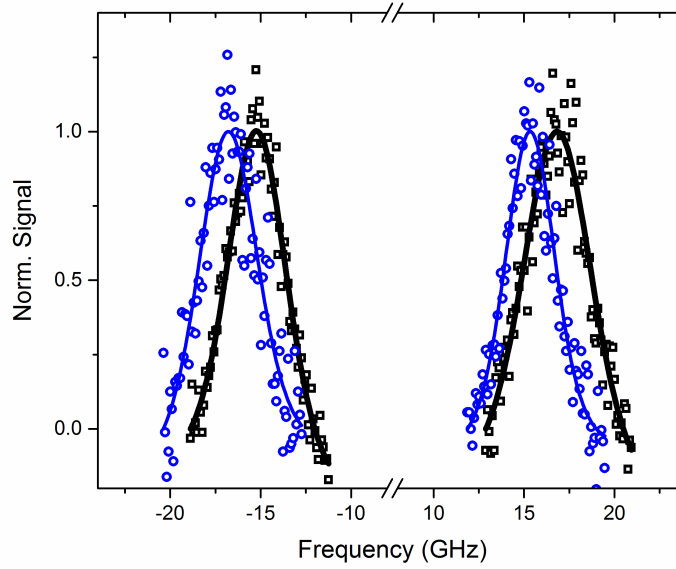
Figure 5.15: Characteristic BLS spin-wave spectra for Co/Ni multilayer grown on a pure Pt seedlayer and the corresponding Δf_{DMI}.

5.2.4 Domain Wall Nanowire Devices Grown on a Composition Varying $Pt - Ir$ Alloy Seedlayer

Domain wall nanowire devices were prepared from magnetic multilayers grown on $Pt - Ir$ alloyed seedlayers using photolithography as explained in Chapter 3.2.3. Nanowire devices are characterized using Kerr Microscopy as explained in Chapter 3.3. Because of the high-throughput technique used to fabricate the nanowire devices, it is relatively simple to find a correlation between seedlayer composition and interfacial DMI in the system. Fig. 5.16, Fig. 5.17, and Fig. 5.18 are example Kerr images obtained for characterizing domain wall displacement. Current is applied at different voltages in order to characterize achieved domain wall velocity as a function of current density, a useful metric for determining device performance. Current is applied in both directions along the nanowire, inducing domain wall motion in directions depending on applied current. Since the domain is originally nucleated on the right contact pad, domain walls growing in the -X(+X) direction is depicted by a white(black) displacement. The nanowire devices demonstrate domain wall motion moving in the direction opposite of electron flow in all cases. This observation indicates that the domain wall motion is driven by the Spin-Hall effect STT rather than the con-

ventional STT (where DWM would be in the direction of electron flow). The resistance of the nanowire can be measured using the same probe setup and with the known dimensions of the device and the magnitude of the applied voltage, the applied current density can easily be calculated. As expected, the chiral domain walls experiences a transition from the creep regime to the flow regime as current density increases and overcomes the pinning forces in the nanowire (Fig. 5.19). The domain wall velocity is found to have a linear relationship with current density until it reaches a maximum voltage. Beyond the threshold voltage, joule heating occurs in the wire causing random magnetic switching and a magnetic multi-domain state.

Critical current density and device efficiency are important device performance metrics can be extracted from domain wall velocity curves. The critical current density is defined as the current required to overcome the pinning forces in the nanowire and induce domain wall motion. Since the exact pinning forces are not explicitly known, the transition out of the creep regime is defined as a region along the velocity curves. We have defined the critical current density as the point where the velocity curves have a change in slope into a more linear trend, as defined by the flow regime characteristics. Plotting the linear fits for domain wall velocity in the flow regime (Fig. 5.20) demonstrates a linear dependence between critical current density and composition. A linear relationship was also demonstrated between interfacial DMI and composition in Fig. 5.13 shown earlier, which suggests correlations between composition, DMI, and device performance. The efficiency of domain wall nanowire devices can also be determined from velocity curves. Device efficiency is calculated at different magnitudes of applied current in order to demonstrate a link between seedlayer composition and device performance. The results are tabulated in the Fig. 5.21 and they show linear improvements in performance as Pt composition increases. This result is not a surprise considering Equation (2.39) predicts higher domain wall velocity for magnetic thin films with larger magnitudes of DMI. The performance of a magnetic thin film can be further improved in systems that have lower anisotropy. However, we have found that a lower anisotropy limits the usefulness of the device as they become more susceptible to thermally induced switching. We have found that for our test systems specifically, applying
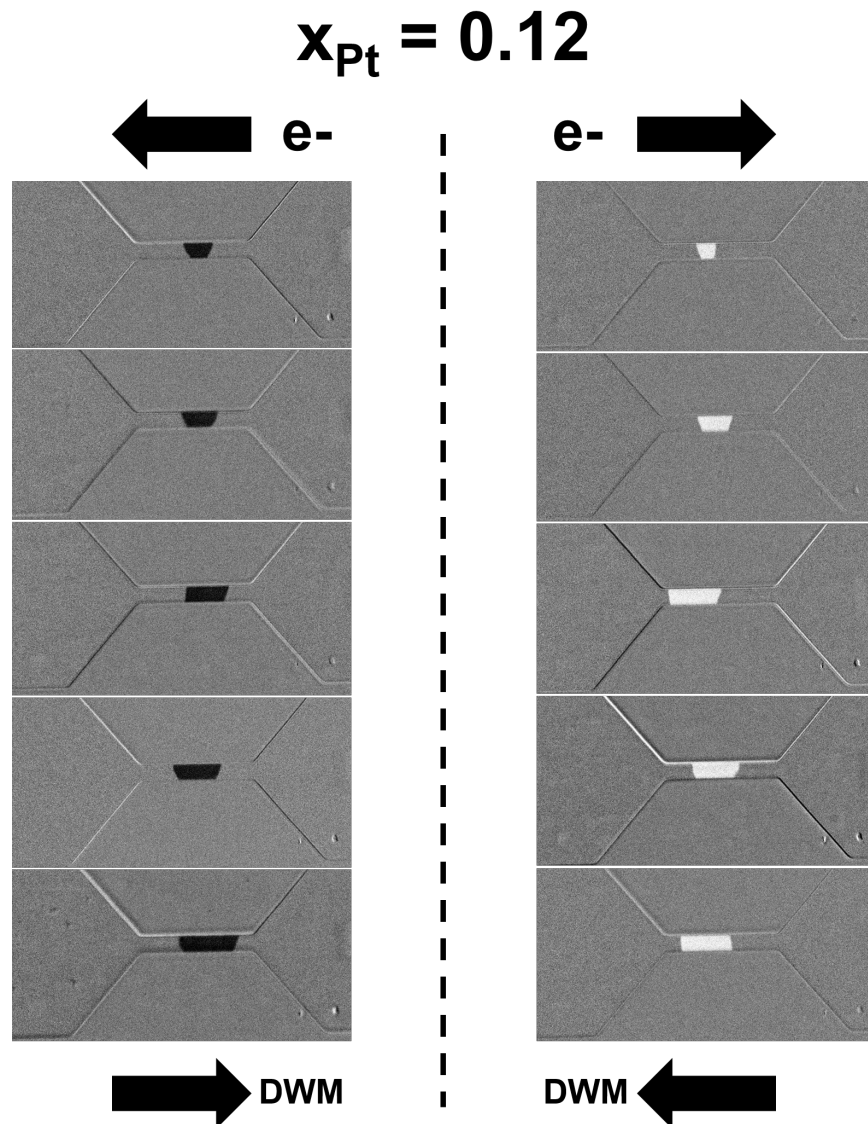
Figure 5.16: Characteristic Kerr microscopy images of domain wall motion along nanowires for seedlayer with Pt composition $\sim$ 0.12. Applied voltage (16V - 20V) increases from top to bottom. Varying pulse lengths were applied.

a voltage greater than 20V will introduce Joule heating causing random switching to occur. The challenge of engineering more efficient systems for domain wall motion means trying to incorporate large DMI and spin transport properties without reducing magnetic anisotropy and saturation magnetization.
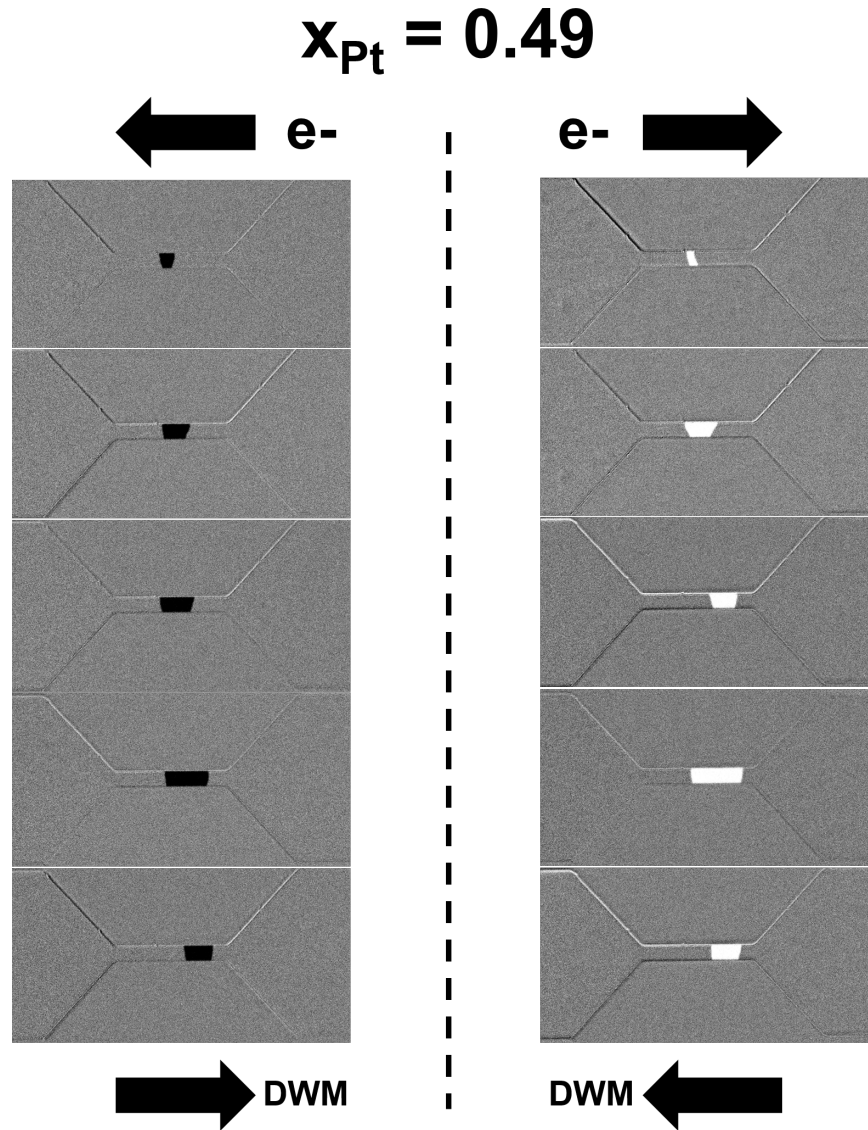
Figure 5.17: Characteristic Kerr microscopy images of domain wall motion along nanowires for seedlayer with Pt composition $\sim$ 0.49. Applied voltage (12V - 20V) increases from top to bottom. Varying pulse lengths were applied.
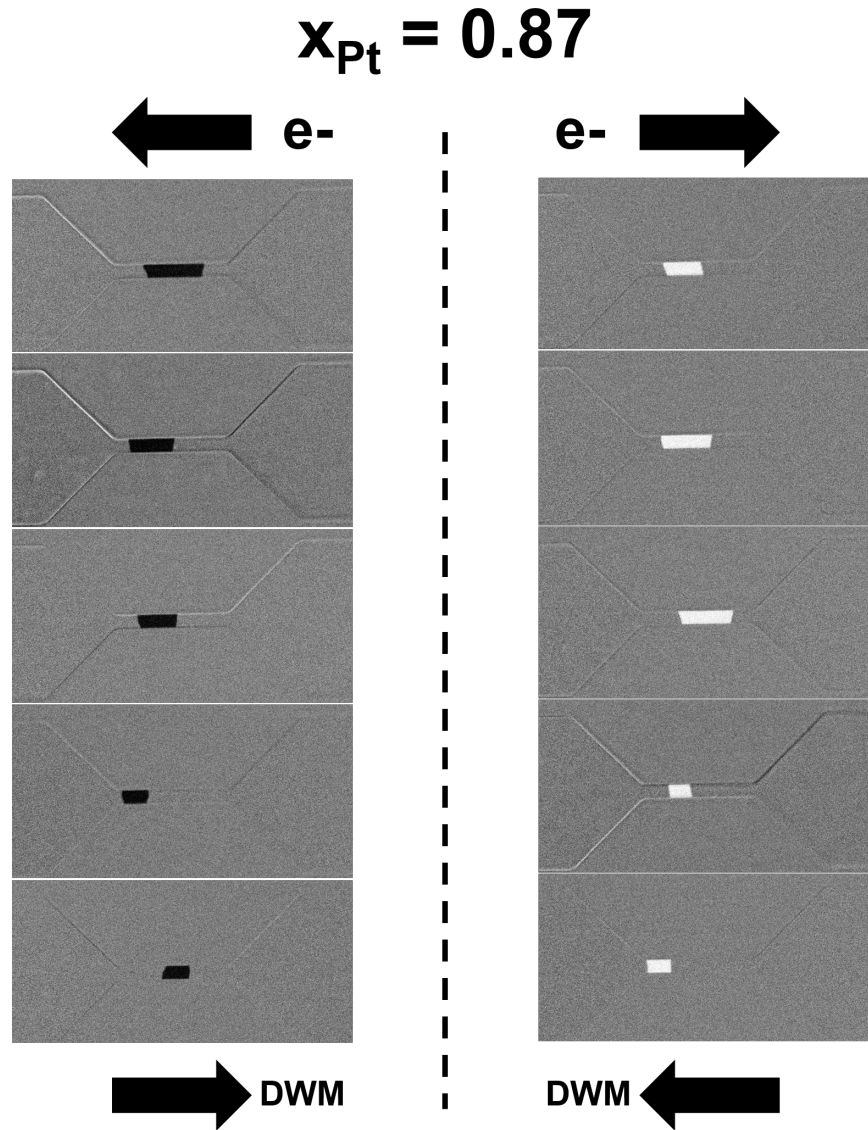
Figure 5.18: Characteristic Kerr microscopy images of domain wall motion along nanowires for seedlayer with Pt composition ~ 0.87. Applied voltage (12V - 20V) increases from top to bottom. Varying pulse lengths were applied.
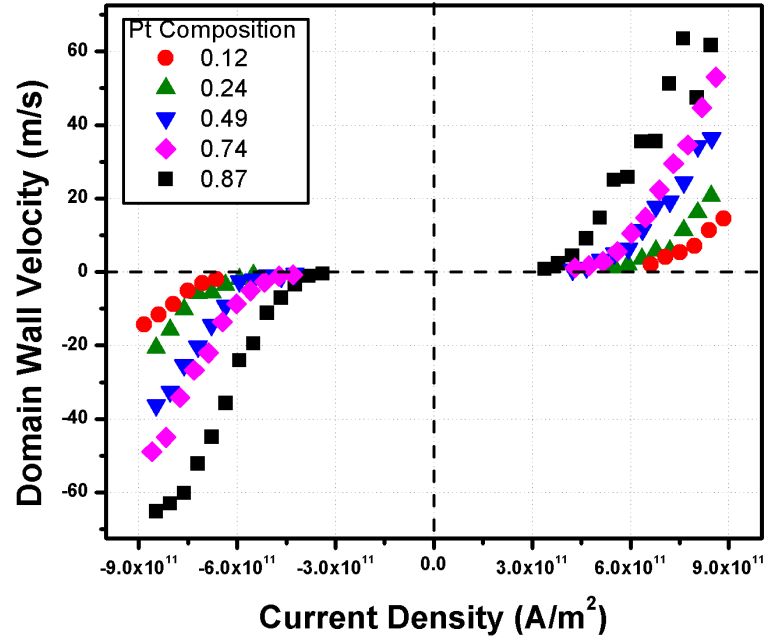
Figure 5.19: Domain wall velocity as a function of current density for varying Pt-Ir alloy seedlayer compositions.
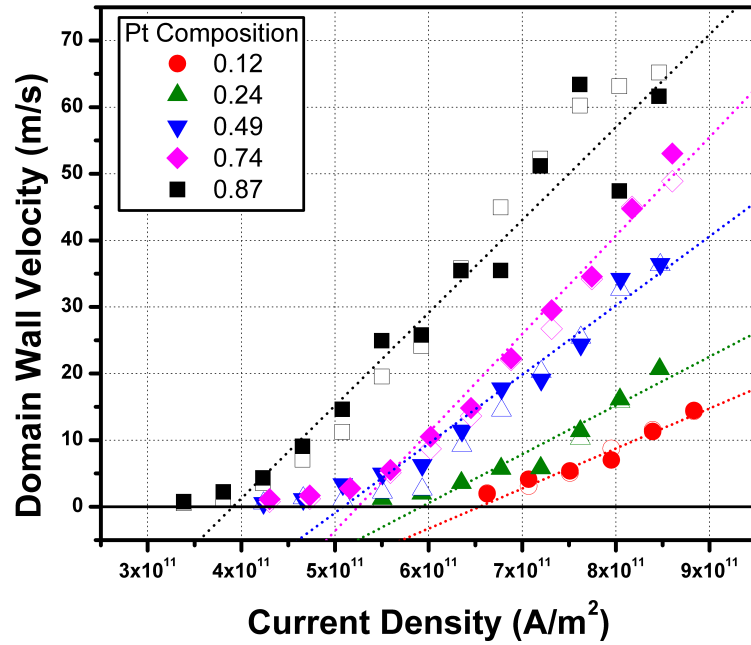
Figure 5.20: Domain wall velocity magnitude and current density with linear fits for domain wall motion in the flow regime.

Pt Composition	0.12	0.24	0.49	0.74	0.87
Critical Current Density (J_c)	6.54×10^{11} A/m^2 (R^2 = 0.93403)	5.92×10^{11} A/m^2 (R^2 = 0.90738)	5.09×10^{11} A/m^2 (R^2 = 0.95534)	5.25×10^{11} A/m^2 (R^2 = 0.97673)	3.91×10^{11} A/m^2 (R^2 = 0.91599)
Domain Wall Velocity (7×10^{11} A/m^2)	2.74 m/s	7.89 m/s	19.84 m/s	25.93 m/s	43.05 m/s
Domain Wall Velocity (8×10^{11} A/m^2)	8.75 m/s	15.21 m/s	30.22 m/s	40.71 m/s	56.98 m/s
Domain Wall Velocity (9×10^{11} A/m^2)	14.77 m/s	22.53 m/s	40.60 m/s	55.48 m/s	70.91 m/s

Figure 5.21: Domain wall velocity magnitude and current density with linear fits for domain wall motion in the flow regime.
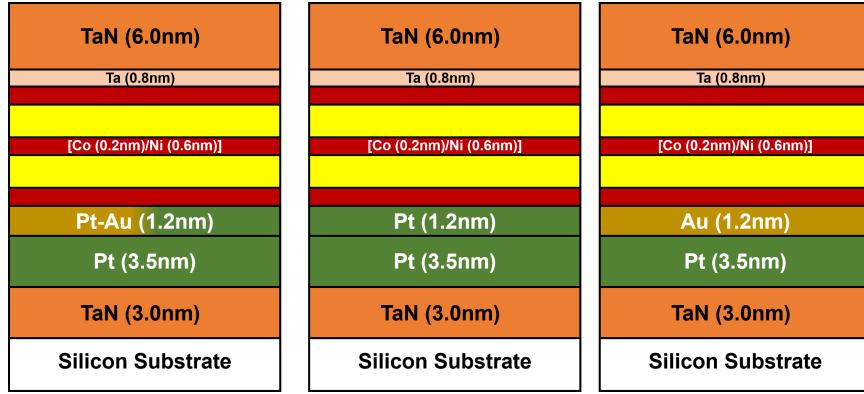
Figure 5.22: Pt-Au alloy seedlayer film stacks deposited for film and device level characterization.

5.3 $Pt/Pt_xAu_{1-x}/[Co/Ni]/Co/Ta$ Magnetic Multilayer

In this section, we illustrate the magnetic properties of a thin film system grown on a $Pt - Au$ alloy seedlayer. Unlike Ir, which was explored in the previous section, Au has been demonstrated to induce small magnitudes of DMI in thin films despite its large spin-orbit coupling. Although the exact magnitude is up for debate, general consensus seems to be that Au is not very conducive for establishing DMI in thin films with broken inversion symmetry [21,74]. We hypothesize that the addition of Au to a Pt seedlayer will reduce the DMI in the system monotomically, as we have shown with the $Pt - Ir$ alloy seedlayer. The deposition method outlined in 3.2 is used to fabricate thin films with a directionally dependent composition gradient. Several filmstacks of the following structure is made for film and device testing: $TaN(3nm)$ / $Pt(3.5nm)$ / $Pt_xAu_{1-x}(1.2nm)$ / $[Co(0.2nm)/Ni(0.6nm)]_2$ / $Co(0.2nm)$ / $Ta(0.8nm)$ / $TaN(6nm)$, where x varies from 0 to 1 (Fig. 5.22). By controlling the sputtering deposition rates, it is relatively simple to tune the recipe to deposit a gradient similar to the $Pt - Ir$ seedlayer explored previously.

5.3.1 Film Structure and Magnetic Properties

5.3.1.1 X-Ray Diffraction (XRD) Characterization

XRD is used to characterize the structural properties of a Pt/Au thin film to confirm the (111) orientation with the addition of gold. A $3nm$ Pt film is deposited on a $1.4nm$ TaN adhesion layer, followed by a $5nm$ layer of Au. The θ-2θ plot is shown in Fig. 5.23. A sharp peak is found at $2\theta = 38.53°$. The theoretical peaks for Pt and Au (111) are $2\theta = 39.75°$

and $2\theta = 38.19°$, respectively. It is possible that the experimental peak corresponds to the two peaks overlapping, which may indicate strain between the two deposited layers. In addition, there is also the presence of satellite peaks in the XRD spectra. We believe the satellite peaks may be a result of the interface between the Pt and Au layers causing coherence in the x-rays, but it has been unconfirmed. Fig. 5.24 is the rocking curve test performed at $2\theta = 38.53°$, the angle of the experimental peak. Fitting the curve to a Gaussian distribution gives a FWHM of $5.459°$, which demonstrates a deposited layer with reasonable texture and roughness. Additional XRD characterization was performed on a thin film with the structure: $TaN(1.4nm)$ / $Pt(2.5nm)$ / $Au(5nm)$ / $Co(10nm)$ to confirm the deposition conditions for obtaining (111) magnetic layers. The spectra shown in Fig. 5.25 shows two main peaks and a satellite peak that matches up reasonably well with the expected (111) peaks for Pt, Au, and Co. The Co (111) peak is expected to appear at $2\theta = 44.28°$ and was experimentally characterized at $2\theta = 44.45°$. Performing a rocking curve analysis at that peak gives a FWHM of $3.981°$, confirming the texture quality of the deposited Co film. With the deposition conditions verified, the magnetic multilayers are expected to show perpendicular magnetic anisotropy.

5.3.1.2 Magnetic Characterization of Pt-Au Alloyed Seedlayer Thin Films

In order to identify relevant magnetic properties of the thin film system, VSM were used extensively. Fig. 5.27 and Fig. 5.28 are representative M-H loops obtained from VSM measurements. The deposited film, $TaN(3nm)$ / $Pt(3.5nm)$ / $Pt_x Ir_{1-x}(1.2nm)$ / $[Co(0.2nm)$ / $Ni(0.6nm)]_2$ / $Co(0.2nm)$ / $Ta(0.8nm)$ / $TaN(6nm)$, shows perpendicular anisotropy, with the easy axis pointing out of plane and the hard axis pointing in-plane. We report coercivity in the perpendicular direction to be $\mu_0 H_c \ sim \ 100Oe$ and the anisotropy field along the in-plane direction to be $\mu_0 H_k \ sim \ 10kOe$ as a function of composition. Fig. 5.29 shows the measured anisotropy field (H_k) as a function of composition in the $Pt - Au$ seedlayer. Except for the pure Pt and pure Au seedlayers, the anisotropy of the thin films are consistently around $10kOe$. From the VSM measurements, the saturation magnetization of the thin films were found to be $M_s \sim 625kA/m$.
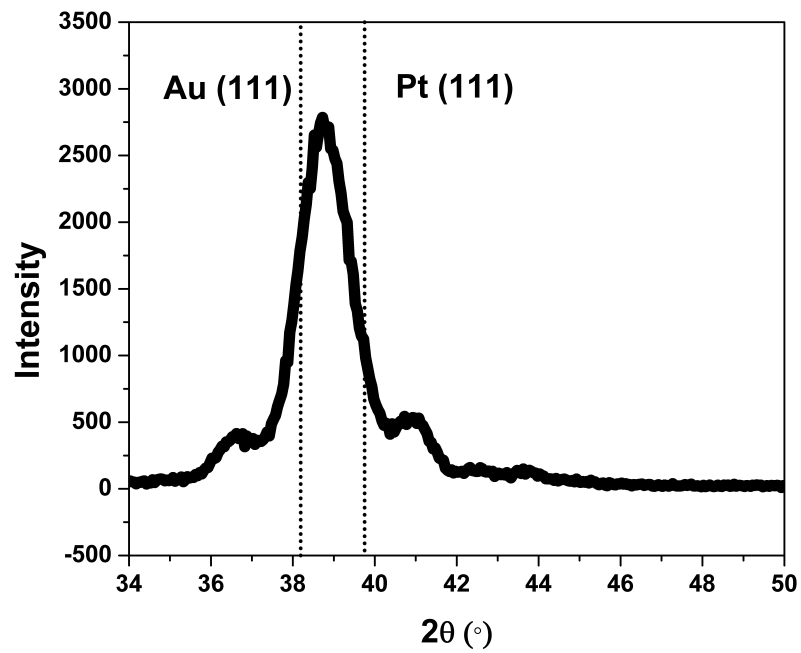
Figure 5.23: XRD spectra characterizing a *Pt* and *Au* (111) thin film. Theoretical *Pt* and *Au* (111) peaks indicated.
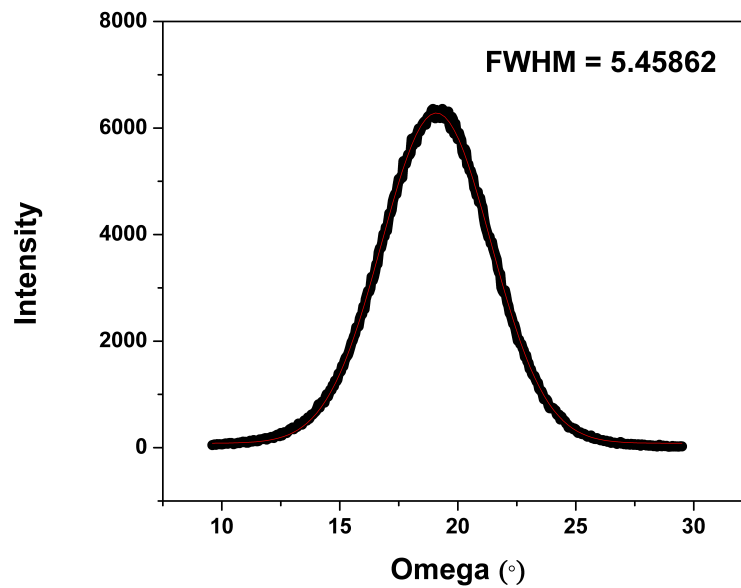
Figure 5.24: Omega rocking curve at $2\theta = 38.53°$ and the observed FWHM for the *Au* (111) peak.
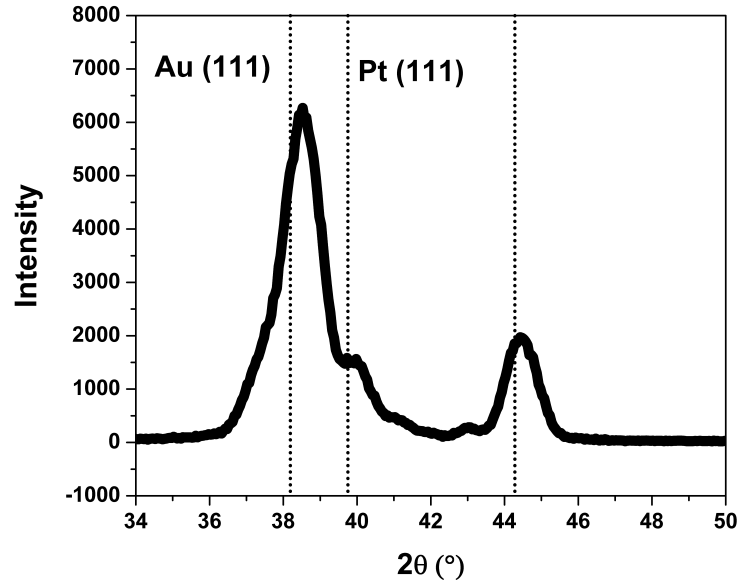
Figure 5.25: XRD spectra characterizing the *Pt/Au/Co* structure. Theoretical *Pt*, *Au*, and *Co* (111) peaks are indicated.
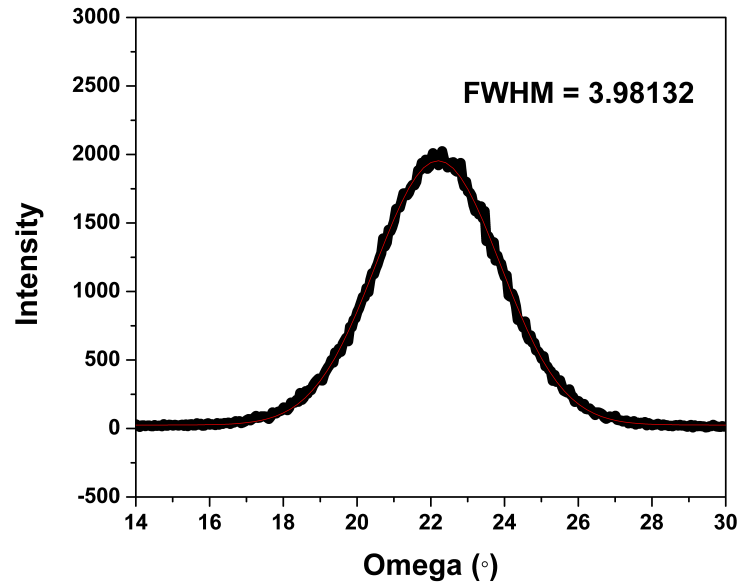
Figure 5.26: Omega rocking curve at $2\theta = 44.45°$ and the observed FWHM for the *Co* (111) peak.

5.3.1.3   DMI Characterization using Kerr Microscopy

$Pt - Au$ alloy samples are prepared for asymmetric domain wall growth experiments by selectively damaging films with a Ga+ ion beam. The process for $Pt - Ir$ sample preparation
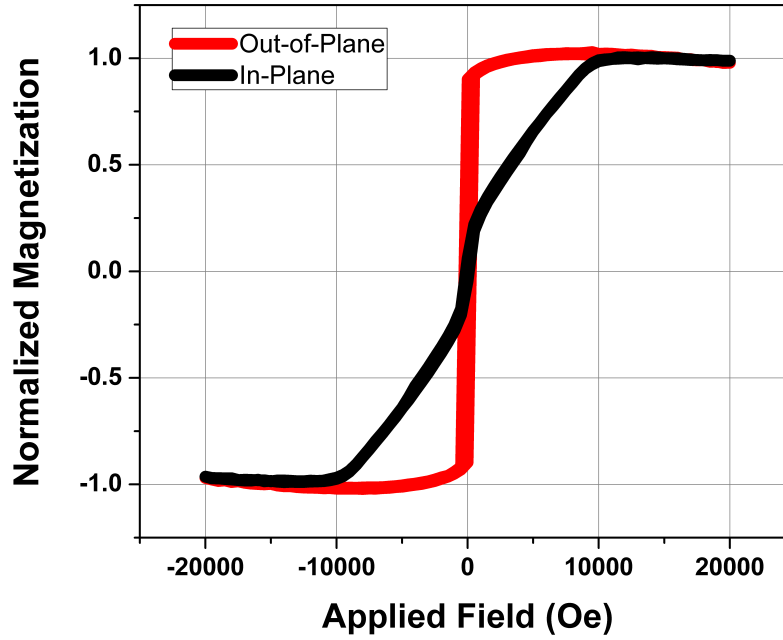
Figure 5.27: Magnetization loops along easy (red) and hard (black) axes of TaN / Pt / Au / [Co/Ni] / Co / Ta / TaN filmstack. Measured anisotropy field of $H_k \sim 13 kOe$.

is repeated for the $Pt - Au$ samples because the film stacks have the same structure. Using the same FIB parameters, a $\sim 10 \mu m$, region is milled away at the center of the $1.0cm$ x $0.5cm$ strips. The FIB operating conditions are tuned to superficially damage the magnetic layer in order to lower the local anisotropy, without affecting the magnetic properties in the surrounding film. With this nucleation site, domain bubbles can be nucleated consistently using an applied perpendicular field ($\mu_0 H_z$), as seen in Fig. 5.30. Additional perpendicular field pulses are applied (+Z) to promote domain bubble expansion, shown in white. A symmetric domain wall growth is depicted when no in-plane field ($\mu_0 H_x$) is applied to the system.

Fig. 5.31 is shows the asymmetric bubble domain growth as a function of applied in-plane field for different seedlayer compositions. The bubble domains are grown by applying a $\mu_0 H_z = 7.00mT$ at different pulse widths to account for the limited size of the viewing screen. We have demonstrated from previous work that the magnitude of the applied field and the applied pulse length does not drastically change the velocity and growth behavior
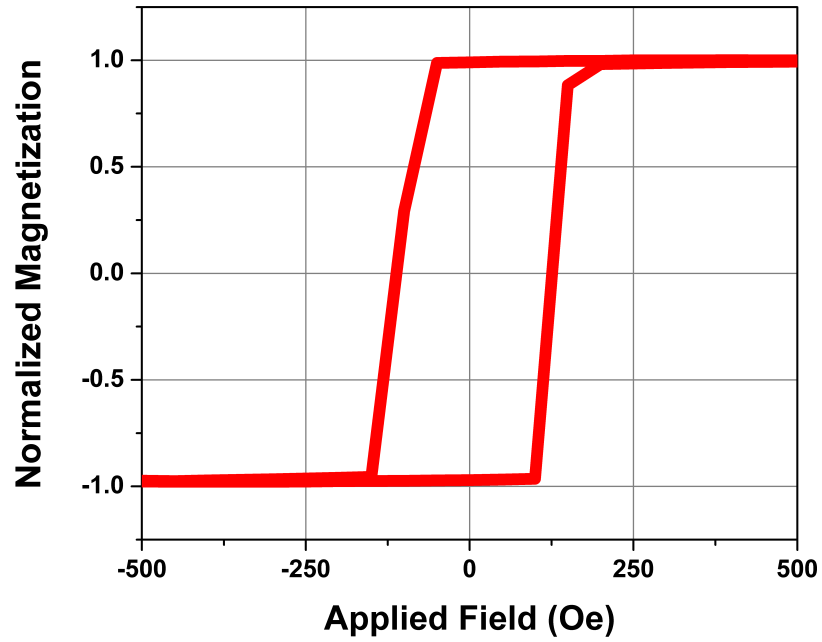
Figure 5.28: Magnetization of TaN/Pt/Au/[Co/Ni]/Co/Ta/TaN filmstack along easy axis. Measured coercivity of $H_c \sim 100 Oe$.
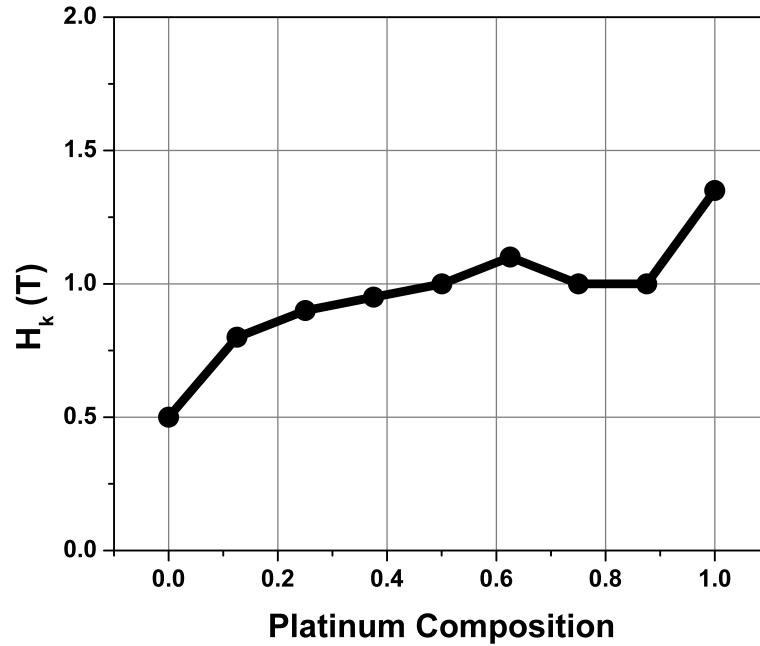
Figure 5.29: Magnetic anisotropy (H_k) as a function of platinum composition in the seedlayer.
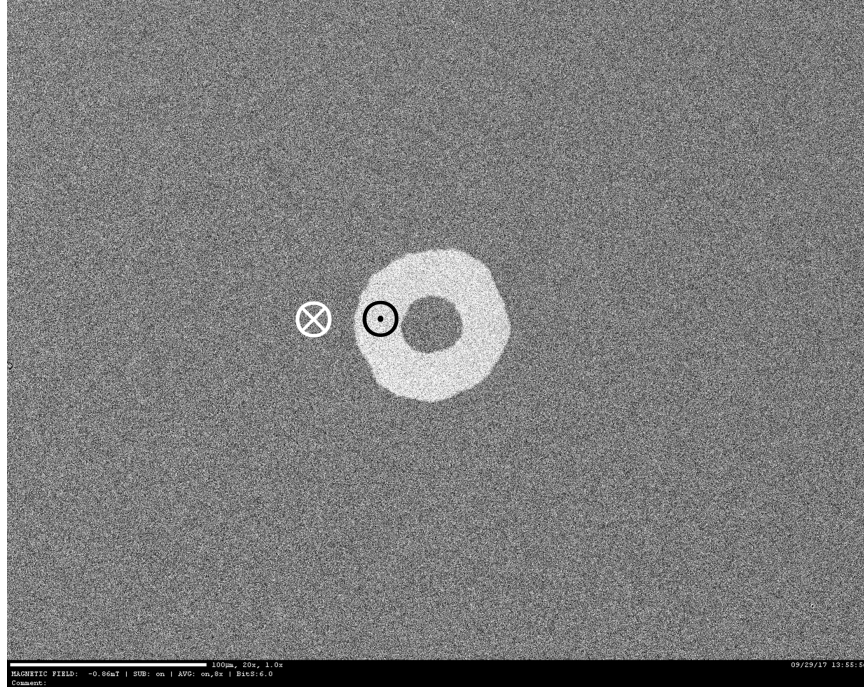
Figure 5.30: Example MOKE image of a bubble domain for Pt-Au alloy seedlayer films.

of the chiral bubble domains [63]. Like the asymmetric bubble growth seen in $Pt - Ir$ alloy samples, the asymmetric domain growth seems to have some dependence on seedlayer composition. It is clear that the bubble domains in $Pt - Au$ show asymmetric growth as a function of in-plane field, but we also find that they experience the same chirality switching behavior noted previously. As the composition of the seedlayer increases, there is an obvious increase in the critical field where this occurs, which is apparent in the series of Kerr images. One significant distinction that is seen in the $Pt - Au$ seedlayers is the lack of the teardrop domains. The bubble domains remain elliptical even as the applied in-plane field increases. Based on the findings discussed in IV, it is likely that the driving force for faceting in these films is significantly lower compared to the films grown on $Pt - Ir$, where more teardrop domains is observed. Qualitatively, the bubble domains suggest a transition from a right handed chirality seen in the pure Au seedlayer to a left handed chirality as the Pt content increases. As seen in the $Pt - Ir$ samples the composition of the seedlayer directly impacts the DMI in the system.
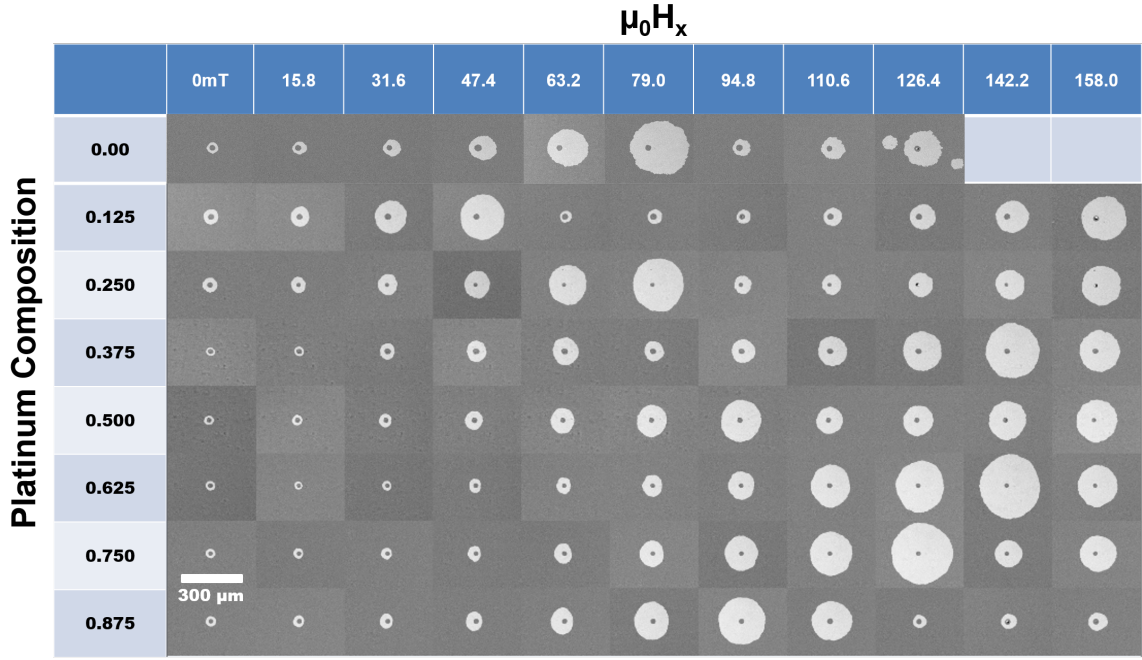
Figure 5.31: Series of MOKE images illustrating the magnetic domain shape as a function of composition and $\mu_0 H_x$. (White: Domains point in +Z. Gray: Domains point in -Z. Center: Domains point in +Z.)

5.3.2 Effects of $Pt - Au$ Alloy Seedlayer Composition on DMI

5.3.2.1 Applying the Dispersive Stiffness Creep Model to Magnetic Multilayers Grown on $Pt - Au$ Alloys

Using the same data fitting method described in 5.2.3, the asymmetric domain wall motion was fit to the Dispersive Stiffness Creep model, given by the equation:

$$v_{creep} = v_0(H_x)exp\left[\kappa\frac{\tilde{\sigma}(H_x)}{\tilde{\sigma}(H_x = 0)}H_z^{-1/4}\right] \tag{5.5}$$

where v_0 is a prefactor given by the chiral damping properties of the magnetic system. The chiral damping is given by:

$$v_0(H_x) = v_0^*(1 + \alpha_{cd}cos(\phi_{eq}(H_x) - \Theta)) \tag{5.6}$$

Experimental fits for selected Pt compositions (0.000, 0.500, and 0.875) are shown in Fig. 5.32. The velocity curves have been observed to shift horizontally in response to the increasing Pt composition in the seedlayers, similar to our observations in the $Pt - Ir$

films. Following the velocity profile for the ↑↓ domains, the observed H_{DMI} changes from negative to positive, indicating a change in domain wall chirality. This change in chirality occurs when $x_{Pt} < 0.125$. The observed magnitude of the effective DMI field is also lower, which is expected considering the low DMI that is usually found in Au interfaces. The vertical asymmetry of the velocity curves does not appear to be as significant compared to the $Pt - Ir$ seedlayer films, indicative of a system that has little chiral damping effects. Plotting A_{creep} of the velocity curves (Fig. 5.33) demonstrates how the chiral effects in the system changes with composition. The magnitudes of the asymmetric effects are significantly lower compared to the $Pt - Ir$ films. In all cases, there is evidence of chiral damping in the thin films tested. The effects of chiral damping dominates the velocity curves for high Au content seedlayers and the elastic domain wall contribution increases as Pt content increases. Although the asymemtric component is dominated by the elastic effects of a chiral domain wall, the asymemtry curves always saturate without returning to zero, which would be expected in films without chiral damping effects. The plotted asymmetric component also describes the change in DMI direction as the slopes of the curves at $H_x = 0mT$ change signs with composition, indicating a change in preferred domain bubble growth. Finally, we observe the emergence of minima and maxima points (attributed to domain wall energy/stiffness) as Pt composition increases, indicating an increase of DMI in response to the addition of Pt in the seedlayer. Our domain bubble characterization reveals that pure Au seedlayers show very little DMI with some chiral damping component. The addition of Pt in the seedlayer reduces DMI without affecting chiral damping too significantly. As Pt content increases, the direction of the DMi vector switches and starts to increase significantly. However, we demonstrated in 5.3 that the velocity and asymmetry plots do not necessarily reflect the actual DMI in the system, requiring a more systematic method of fitting velocity curves. In Fig. 5.33, the velocity curves are fit to the dispersive stiffness model and the extracted values of DMI is confirmed to increase with Pt content. The creep fits show a change in sign of the DMI vector, although the magnitude is extremely small and may actually be closer to zero in all Au rich seedlayers. The actual magnitudes of the extracted DMI vectors are much lower than what we observed from the $Pt - Ir$ cases. The chiral damping weight is also shown to be more significant for Au rich seedlayers and Pt
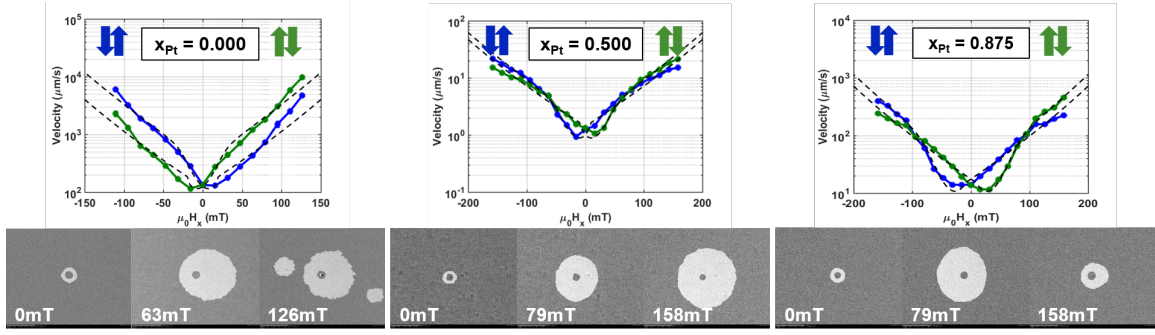
Figure 5.32: Experimental v vs. $\mu_0 H_x$ for seedlayers with varying x_{Pt} with representative MOKE images. Dashed lines are fits from Equation (5.2). The center grey of the Kerr images represent the initial bubble shape while the white region is the domain after growth under both $\mu_0 H_x$ and $\mu_0 H_z$, which was fixed at 7 mT

rich seedlayers. It is worth noting that the magnitude of the chiral weight in Pt (characterized previously) is much higher than the chiral weight found in Au. For the compositions in between the two extremes, the chiral weight seems to cancel each other out. Our findings suggest that pure Au induces very low DMI and low chiral damping effects in thin films compared to Ir and Pt. It seems that the addition of Au to a Pt seedlayer significantly reduces the total DMI and chiral damping effects in the system.

5.3.3   Domain Wall Nanowire Devices Grown on a Composition Varying $Pt - Au$ Alloy Seedlayer

Domain wall nanowire devices have been fabricated from the $Pt - Au$ alloy seedlayer thin films to test device performance as a function of composition. Fig. 5.34, Fig. 5.35, and Fig. 5.36 are example Kerr images obtained for characterizing domain wall displacement. As with the $Pt - Ir$ nanowire devices, a domain wall is nucleated from a region on the rightmost pad into a nanowire measuring $\sim 30\mu m$ by $4\mu m$ (length x width). Current is applied in both directions in order to control the direction of domain wall motion seen in the Kerr images. Since the domain is originally nucleated on the right contact pad, domain walls growing in the -X(+X) direction is depicted by a white(black) displacement. In all cases, current driven domain wall motion is shown to be in the direction opposite of electron flow, indicating spin-transfer torque through the spin-hall effect. Domain wall motion travels in the creep regime until the driving force becomes large enough where the pinning potential in the film is essentially ignored, resulting in a sharp increase in domain wall motion past
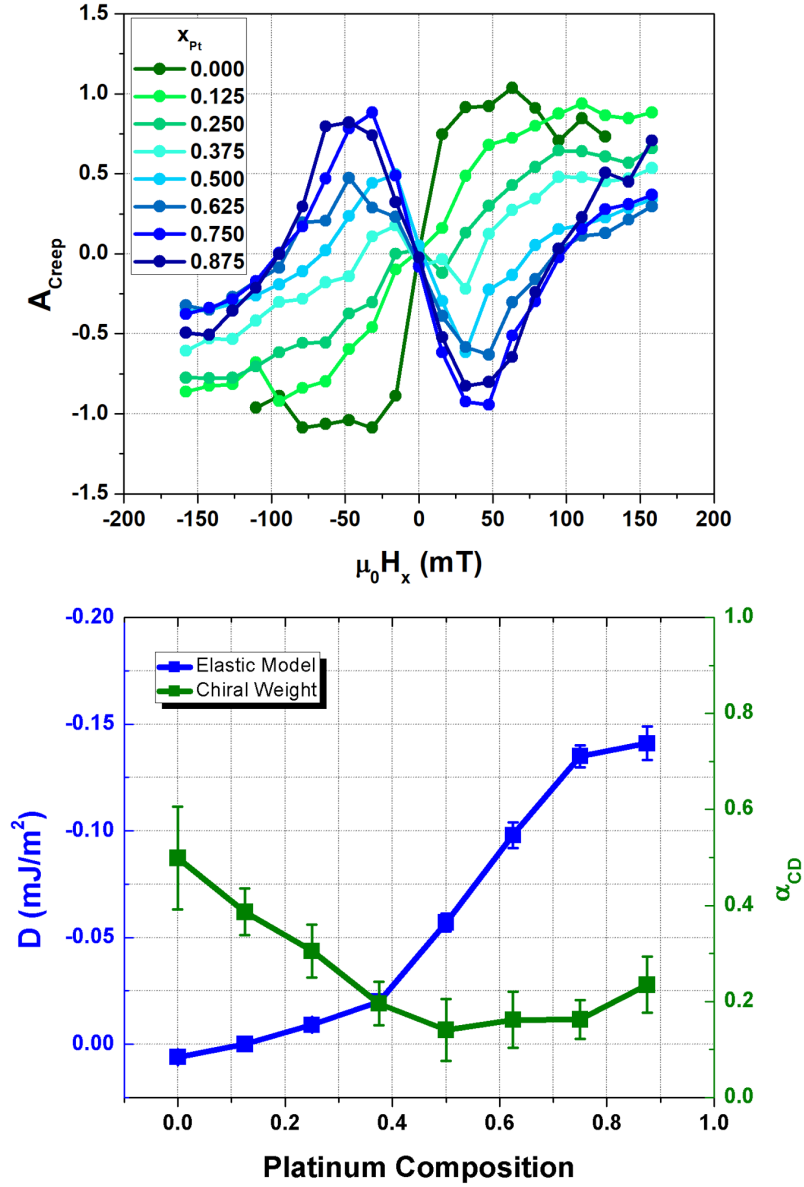
Figure 5.33: a) A$_{creep}$ vs. $\mu_0 H_x$ as a function of X$_{Pt}$. b) Extracted values of D and α_{cd} vs X$_{Pt}$ based on fits to (a).

the critical current density, as seen in Fig. 5.37. Like the $Pt - Ir$ seedlayers, we have found that past 20V of applied voltage, heating issues are introduced, resulting in random domain nucleation/switching and a multi domain state. our experimentation is done in a region where accurate domain wall displacement can be measured in the Kerr microscope, usually between 10V-20V.
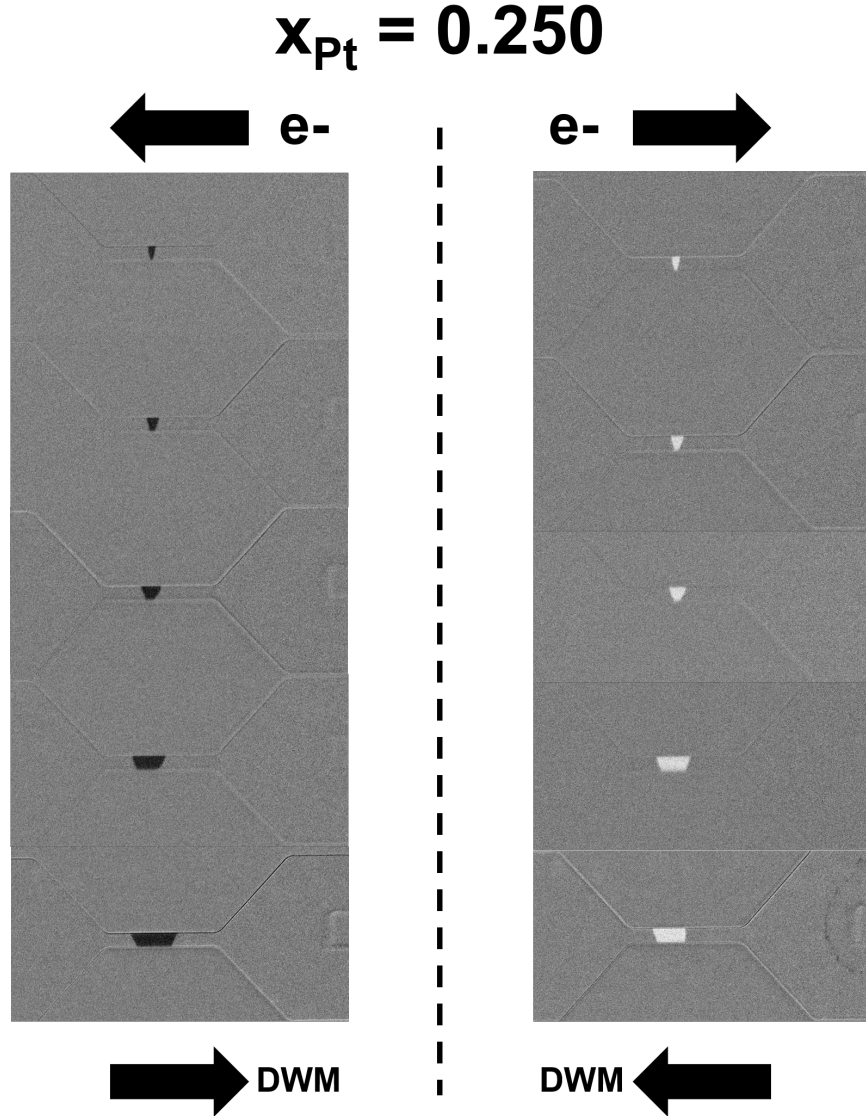
Figure 5.34: Characteristic Kerr microscopy images of domain wall motion along nanowires for seedlayer with Pt composition ~ 0.12. Applied voltage (12V - 20V) increases from top to bottom. Varying pulse lengths were applied.

Critical current density is calculated by fitting the linear portion of the velocity curves as seen in Fig. 5.38. We find a similar trend seen in the $Pt-Ir$ samples that show an increase in critical current density as the Pt content decreases. This indicates a larger field required to induce domain wall motion for devices that contain less Pt. In that case, the critical current density appears to be correlated to the effective DMI in the system. However, it should be noted that presence of Au in the seedlayer severely dampens the device performance
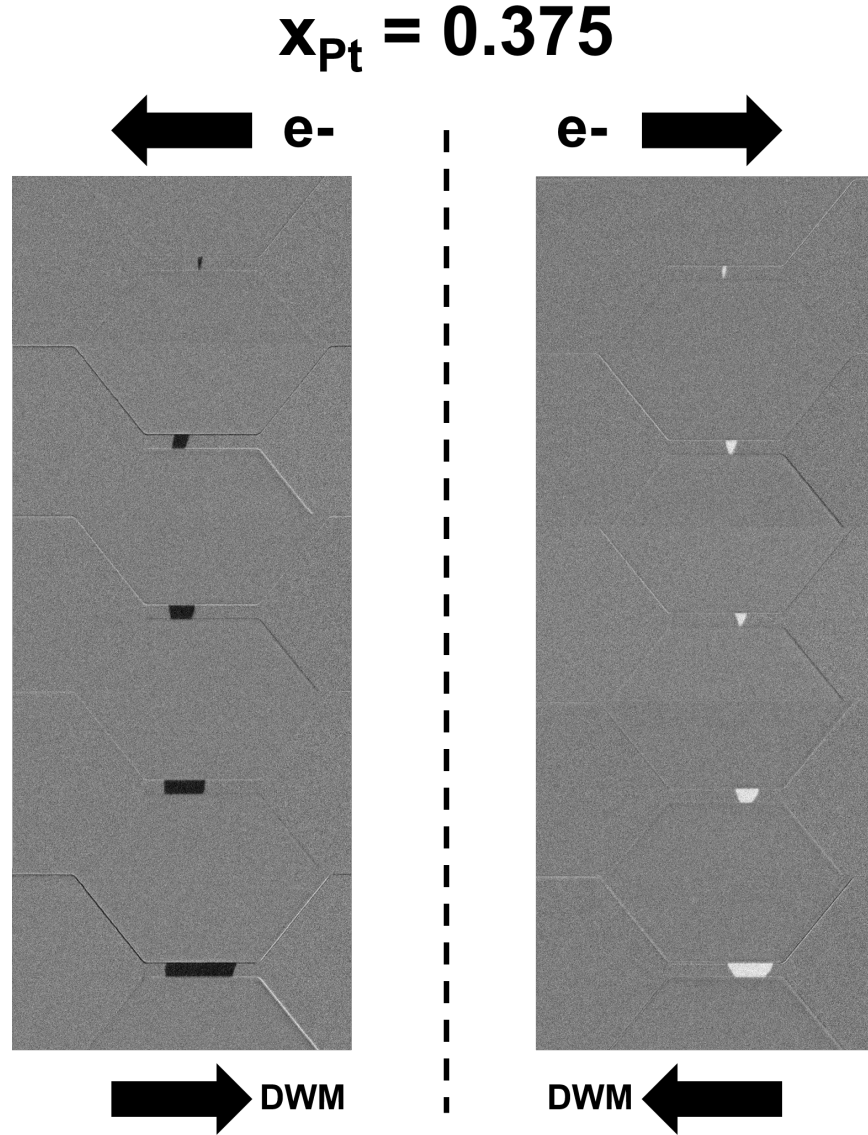
Figure 5.35: Characteristic Kerr microscopy images of domain wall motion along nanowires for seedlayer with Pt composition ~ 0.49. Applied voltage (12V - 20V) increases from top to bottom. Varying pulse lengths were applied.

even though the critical current density is comparable to the the $Pt - Ir$ nanowires. As seen in the tabulated efficiency values in Fig. 5.39, the domain wall velocity achieved by the nanowires is significantly lower compared to domain wall velocity magnitudes achieved with the $Pt - Ir$ nanowires. However, we are hesitant to draw any conclusions comparing the two systems, since they were fabricated under different conditions. But, we have shown in both cases, that DMI can be engineered to tune the performance of current driven domain wall devices.
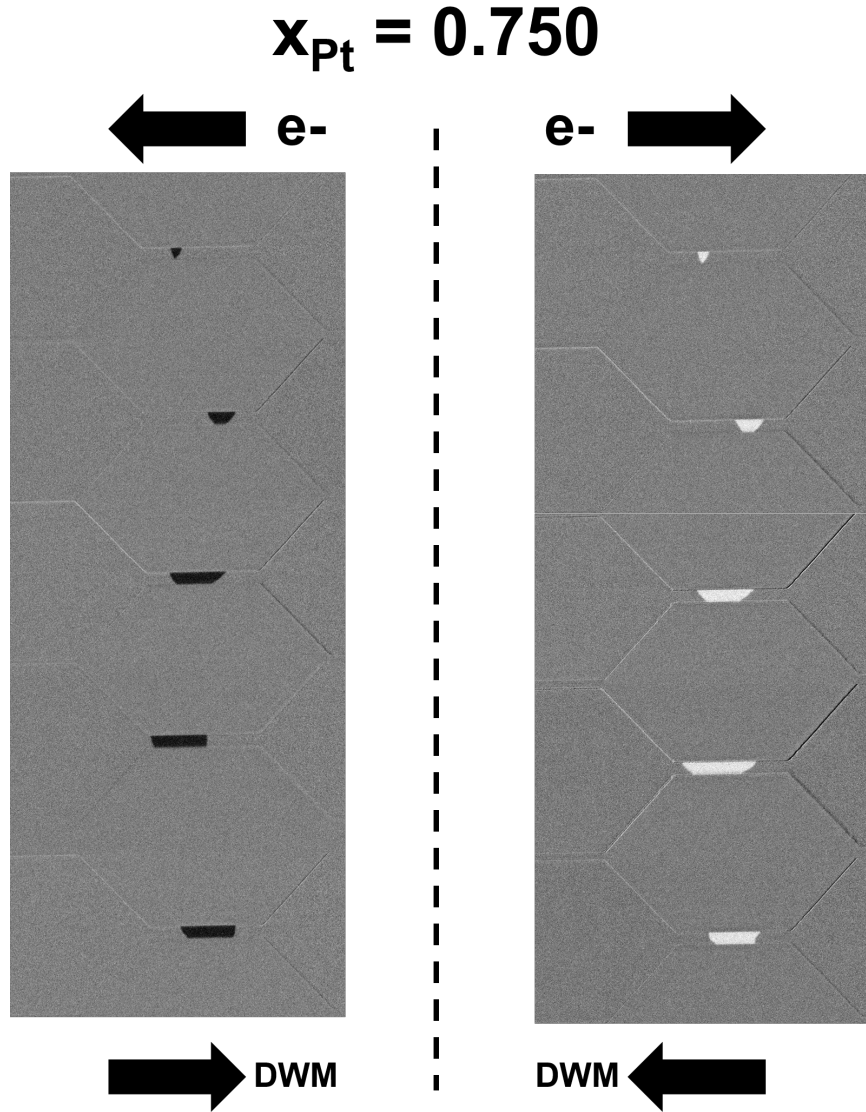
Figure 5.36: Characteristic Kerr microscopy images of domain wall motion along nanowires for seedlayer with Pt composition $\sim$ 0.87. Applied voltage (12V - 20V) increases from top to bottom. Varying pulse lengths were applied.

The tabulated domain wall velocity values are plotted as a function of DMI magnitude of both the $Pt - Ir$ and $Pt - Au$ systems, as seen in Fig. 5.40. Our current drivent velocity experiments demonstrate an almost linear relationship between DMI and nanowire device performance. Although we cannot compare the two systems directly, we observe a direct impact of DMI magnitude on domain wall velocity. In general, the devices characterized with smaller(larger) DMI will induce slower(faster) domain wall velocities, predicted in simulation work by Thiaville et al [86]. From Equations (2.27), (2.28), (2.32), the critical
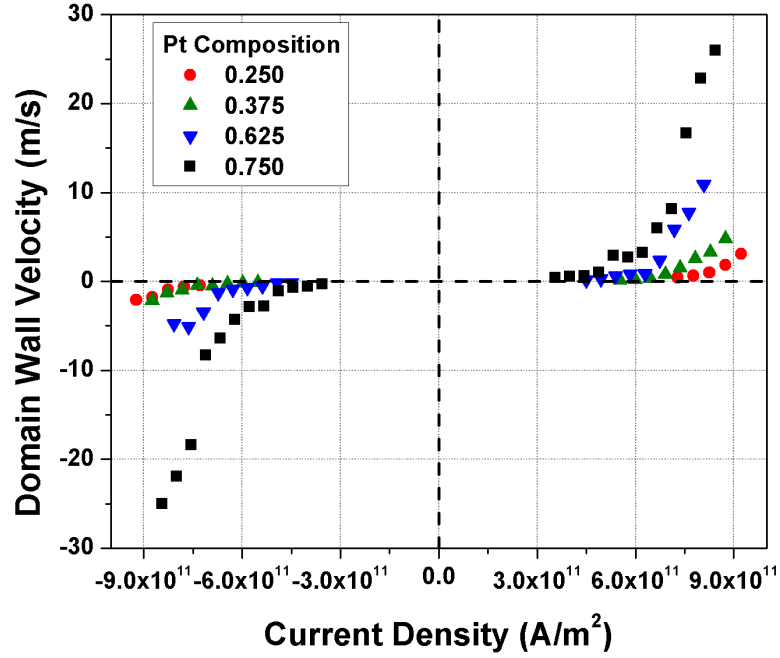
Figure 5.37: Domain wall velocity as a function of current density for varying Pt-Ir alloy seedlayer compositions.

DMI magnitude for inducing Néel Domain Walls (without externally applied fields) in thin films is calculated using the equation:

$$D_{critical} = \frac{\ln 2}{\pi} \mu_0 M_s^2 t_f \tag{5.7}$$

Calculating the critical DMI for both systems establishes different ranges of DMI that correspond to Bloch Wall, Néel Wall, and their intermediate configurations, as seen in Fig. 5.40. Interestingly, the plots show an increase in current driven domain wall velocity with DMI, and continues to increase past the critical DMI magnitude. Recent theoretical predictions, however, demonstrate a saturation in current induced domain wall velocity after a domain wall becomes fully Néel, contrary to our findings [87]. One likely explanation is that larger DMI magnitudes continue to stabilize domain walls even after the Néel Wall configuration is achieved, although this requires more evidence not covered in this thesis work. In summary, our experimental results from DMI characterization and domain wall motion characterization experiments have demonstrated the possibility of achieving more
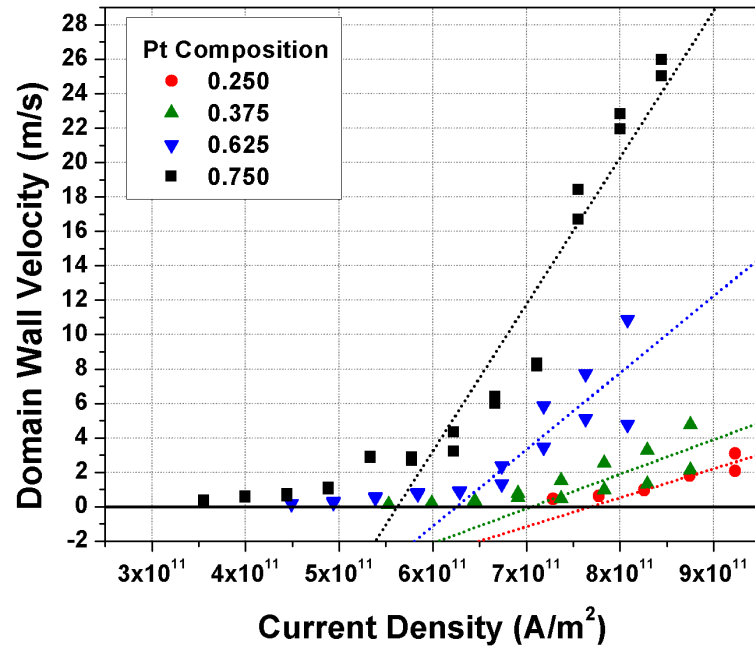
Figure 5.38: Domain wall velocity magnitude and current density with linear fits for domain wall motion in the flow regime.

Pt Composition	0.250	0.375	0.625	0.750
Critical Current Density (J_c)	7.68x10^{11} A/m^2 (R^2 = 0.70729)	7.05x10^{11} A/m^2 (R^2 = 0.37605)	6.25x10^{11} A/m^2 (R^2 = 0.43525)	5.62x10^{11} A/m^2 (R^2 = 0.89654)
Domain Wall Velocity (7x10^{11} A/m^2)	0.00 m/s	0.00 m/s	3.33 m/s	11.77 m/s
Domain Wall Velocity (8x10^{11} A/m^2)	0.53 m/s	1.90 m/s	7.79 m/s	20.30 m/s
Domain Wall Velocity (9x10^{11} A/m^2)	2.22 m/s	3.90 m/s	12.25 m/s	28.83 m/s

Figure 5.39: Domain wall velocity magnitude and current density with linear fits for domain wall motion in the flow regime.

efficient domain wall through seedlayer composition tuning.
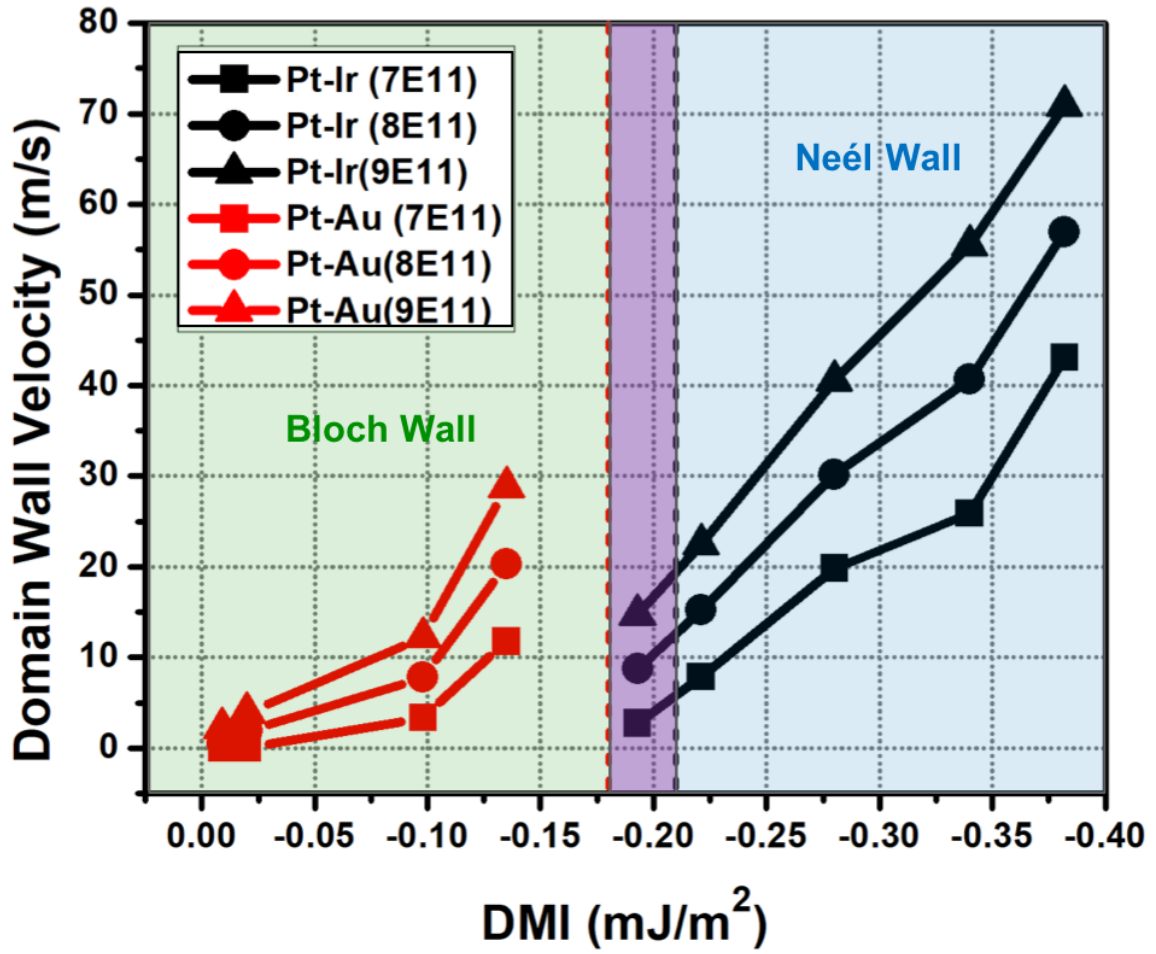
Figure 5.40: Domain wall velocity as a function of DMI magnitude for different current densities. Regions corresponding to Bloch Walls and Néel Walls are calculated based on the critical DMI magnitude for each system. The center region marks a range where both systems may have domain walls that show both Bloch and Néel characteristics.

The Effect of Terminating Interfaces on Interfacial DMI in Co/Ni Thin Films

This chapter is discussion of the experimental work performed to gain insight on the interfacial nature of DMI in magnetic multilayer thin films. The main focus is to demonstrate how terminating interfaces influence the effective DMI magnitude and direction in the system. In literature, asymmetric magnetic multilayers have been researched extensively, with emphasis on different heavy metal interfaces to determine their potential to induce DMI [11, 19, 20, 25–27, 88, 89]. In addition, there has also been efforts to characterize the DMI in materials through computational methods [21, 74–76, 90]. One of the main motivations for this research is to engineer larger spin-orbit effects in thin films by taking advantage of the theoretical additive property of DMI from multiple interfaces. Although most of the experimental work conducted so far focus on DMI originating from the seedlayer, it is worthwhile to investigate any additive (or subtractive) effects that the capping layer interface may produce. In this work, we examine the effects of Co/Pt, Co/Ir, Ni/Co, and Ni/Ir terminating interfaces that have been grown on the Pt/Co seedlayer interface.

6.1 DMI Contribution from a Co/Pt Terminating Interface

A symmetric multilayer sample with the structure: TaN / Pt / $[Co/Ni]_2$ / Co / Pt / TaN is fabricated with the intention of comparing its DMI to its asymmetric counterparts'. A 3.5nm thick Pt layer is deposited on top of the 1.8nm $[Co/Ni]$ multilayer that has been grown on a 3.5nm thick Pt seedlayer Fig. 6.1. Compared to the structure tested in Chapters IV and V (TaN / Pt / $[Co/Ni]_2$ / Co / Ta / TaN), the DMI is expected to be

nonexistent because of its symmetric structure. Magnetic characterization through VSM demonstrated that the system is perpendicularly magnetized, has an anisotropy field $H_k \sim 7 - 8kOe$, and a magnetic saturation $M_s \sim 622 \ kA/cm^3$ Fig. 6.2. Representative Kerr images are shown in Fig. 6.3 at different magnitudes of applied in-plane field. Based on the asymmetric growth of the bubbles, the domain walls appear to have chirality. At first glance, the symmetric growth suggests a right handed chirality, but there is the possibility that the domain bubbles experience the critical chirality switching field at much lower magnetic fields. There is also evidence of dendritic domains forming as the magnitude of the applied in-plane field increases. This observation is likely due to the lower anisotropy and coercivity that was characterized in this system. It is also possible that this particular sample has a denser pinning distribution compared to other samples tested, but that is difficult to quantify experimentally. Plotting out the velocity profile suggests that the film has very low DMI. As seen in Fig. 6.3, the velocity curves for both types of domain walls ($\uparrow\downarrow$ and $\downarrow\uparrow$) show no horizontal shift, indicating lower DMI. However, there is evidence of preferential growth as seen by the asymmetry about the velocity minimum in both cases. This is reminiscent of the velocity curves characterized by Jue et al [71] magnetic systems under the influence of only chiral damping. The asymmetry curves plotted in Fig. 6.3 also supports that conclusion. The asymmetric component of the creep velocity is characteristic of a system that only has chiral damping (Fig. 4.22). Fitting the velocity profile using the dispersive stiffness model gives a DMI of $D = -0.08mJ/m^2$ and a chiral damping factor of $\alpha_{cd} = 0.40$. Compared to the asymmetric filmstack, the characterized DMI is much lower with some chiral damping factor contributing to the observed curve asymmetry, as expected.

Figure 6.1: Symmetric multilayer with Pt/Co and Co/Pt interfaces.

Figure 6.2: In-Plane M-H loop for $Pt/[Co/Ni]_2/Co/Pt$ symmetric multilayer showing magnetization along hard axis.

Figure 6.3: a) Domain wall velocity profile with fits using the Dispersive Stiffness Model. b) A_{creep} vs. applied in-plane field (H_x) c) Representative Kerr images at different in-plane fields applied in the positive x-direction.

6.2   DMI Contribution from a Co/Ir Terminating Interface

We now move on to magnetic structures that are capped by a layer of Ir, creating a Co/Pt terminating interface Fig. 6.4. This breaks the inversion symmetry in the structure and induces DMI in the system, much like the structures explored in Chapters IV and V. However, the effective DMI considering the spin-orbit contribution from an Ir capping layer is something that we have yet to characterize. Characterizing the magnetic properties of this system gives an anisotropy field $H_k \sim 7 - 8kOe$, and a magnetic saturation $M_s \sim 615$ kA/cm^3 Fig. 6.5. Based on the representative Kerr images (Fig. 6.4), asymmetric bubble growth is observed, indicating the presence of chiral domain walls and the influence of DMI. In this case, a large DMI is expected because of the asymmetric nature of the magnetic multilayer. We also observe the lack of dendritic domain growth, which may be the result of the higher anisotropy measured in the sample or the relatively lower applied in-plane field for this experiment compared to the symmetric system tested in Chapter 6.1. Looking at the velocity plot, the profiles resemble the shifted and asymmetric curves seen in earlier chapters, which suggests a DMI component as well as a chiral damping component in the system. As seen in Fig. 6.6, the velocity curves for both types of domain walls ($\uparrow\downarrow$ and $\downarrow\uparrow$) show significant horizontal shift, indicating larger DMI. In addition, the velocity curves are vertically offset and asymmetric, indicating chiral weight. This observation is further supported by the plot of the asymmetric component of the sample, indicative of both elastic energy effects and chiral weight in the system, as seen in Fig. 4.22. Fitting the data to the dispersive stiffness model extracts a DMI of $D = -0.313mJ/m^2$ and a chiral damping factor of $\alpha_{cd} = 0.41$.

Figure 6.4: Asymmetric multilayer with Pt/Co and Co/Ir interfaces.

Figure 6.5: In-Plane M-H loop for $Pt/[Co/Ni]_2/Co/Ir$ asymmetric multilayer showing magnetization along hard axis.

Figure 6.6: a) Domain wall velocity profile with fits using the Dispersive Stiffness Model. b) A_{creep} vs. applied in-plane field (H_x) c) Representative Kerr images at different in-plane fields applied in the positive x-direction.

6.3   DMI Contribution from a Ni/Ir Terminating Interface

From our previous test cases, we observe a large increase in DMI when the Pt capping layer in a symmetric structure is replaced with an Ir capping layer. This increases is most likely the result of the magnetic system losing its inversion center, as expected. We start with the assumption that Ni/Ir interface has a similar contribution as the Pt/Ir interface. We make this assumption based on the fact that the thin monolayers is effectively a single uniform magnetic layer. Theoretically, having an Ir capping layer breaks the symmetry of the system, inducing DMI. In the case where the capping layer is Pt, there is effectively no DMI, theoretically. In order to test this theory, we have fabricated a thin film with a wedge Ir cap, using the method outlined in 3.2 (Fig. 6.7). The idea is that as the thickness of the Ir cap decreases, the system becomes more symmetric, resulting in a monotomically decreasing trend in interfacial DMI. From magnetic characterization, we obtain an anisotropy field $H_k \sim 7 - 8kOe$, and a magnetic saturation $M_s \sim 615 \ kA/cm^3$ Fig. 6.8. The representative Kerr images show asymmetric domain growth as well as the reversal of chirality, supported by the domain wall velocity profile shown in Fig. 6.9. Like in previous sections, the velocity profile displays a horizontal displacement as well as some vertical asymmetry, indicating DMI and chiral damping. Fitting the data from various samples (with varying Ir layer thicknesses) to the dispersive stiffness model shows no obvious trends as a function of Ir layer thickness. We extract an average DMI value of $D = -0.386mJ/m^2$ and an average chiral damping factor of $\alpha_{cd} = 0.30$. With this result, we demonstrate that the thickness of the Ir capping layer seems to have no effect on the effective DMI in the system. Based on this, it is probable that most of the effective DMI is induced by the Pt/Co interface at the seedlayer which may be much larger than the DMI induced at the Ir/Pt capping layer.
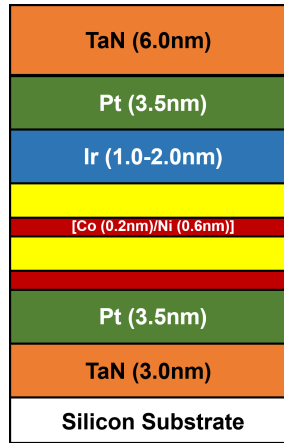
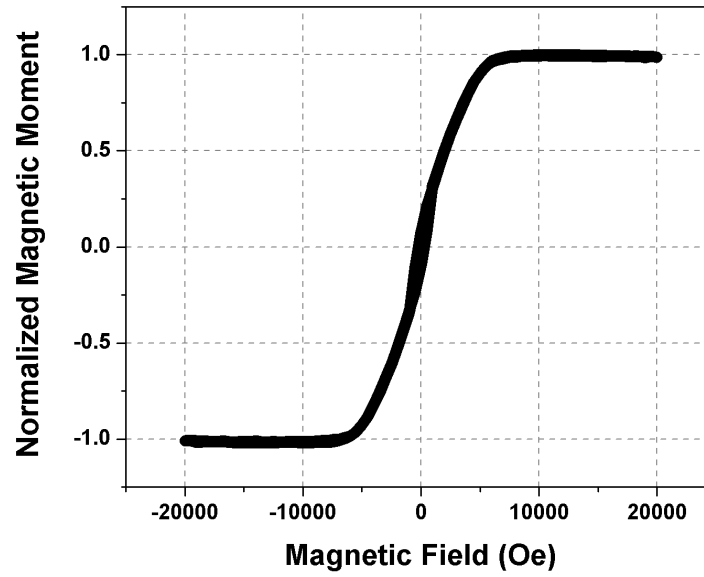Figure 6.7: Asymmetric multilayer with Pt/Co and Ni/Ir interfaces.

Figure 6.8: In-Plane M-H loop for $Pt/[Co/Ni]_2/Ir$ asymmetric multilayer showing magnetization along hard axis.
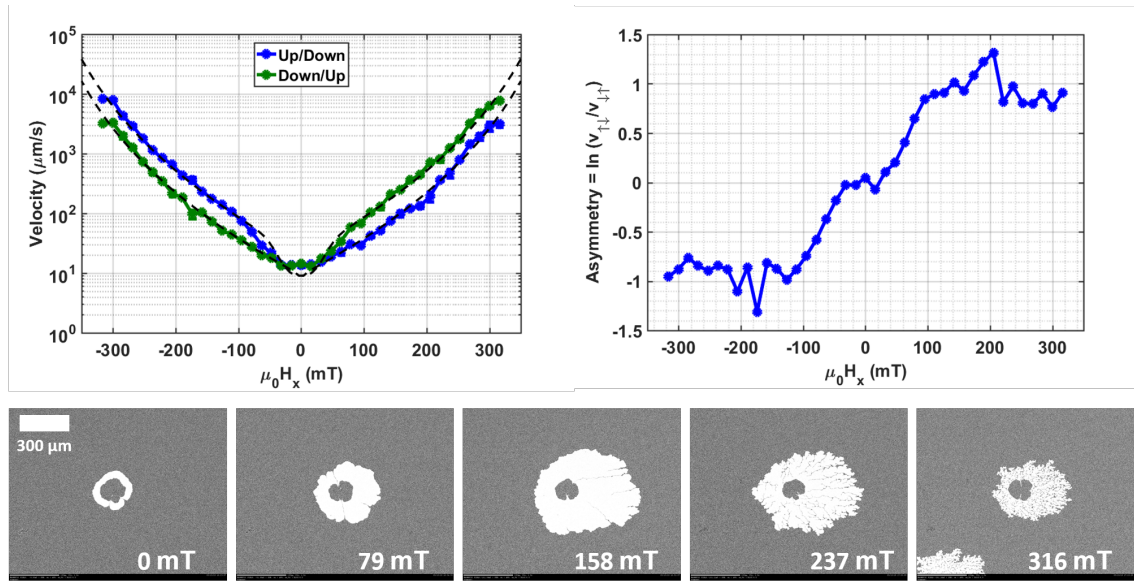
Figure 6.9: a) Domain wall velocity profile with fits using the Dispersive Stiffness Model. b) A_{creep} vs. applied in-plane field (H_x) c) Representative Kerr images at different in-plane fields applied in the positive x-direction.

6.4 DMI Contribution from a Ni/Pt Terminating Interface

In this section, we expand on prior work in order to characterize the spin-orbit interaction from a Ni/Pt interface, relative to the strength from the bottom Pt/Co interface. In the previous section, we found that the addition of an Ir capping layer consistently gives an asymmetric system with high DMI, even though the terminating interface is Ni. It is unclear if the Ni/Ir terminating interface contributes to the overall interfacial DMI in the system. Therefore, it is necessary to characterize the effective DMI of a magnetic thin film grown on a Pt seedlayer that terminates with a Ni/Pt interface as seen in Fig. 6.10, in order to isolate the contribution from the $Ni/HeavyMetal$ interfaces. If the DMI vector from the Ni/Pt interface is similar magnitude and direction, the effective DMI in the system is expected to cancel out, resulting in a system with properties similar to the symmetric filmstack case. However, if the DMI vector points in the opposite direction, the effective DMI might be expected to increase overall. From VSM characterization, we find that this system is perpendicularly magnetized with an anisotropy field $H_k \sim 7 - 8kOe$, and a magnetic saturation $M_s \sim 600 \ kA/cm^3$ (Fig. 6.11). Representative Kerr microscopy images shown in Fig. 6.12 reveal a system that is qualitatively similar to the asymmetric thin film explored in the previous section. The chiral domain walls appear to have a left-handed orientation and seen in their asymmetric growth. However, at $\mu_0 H_x \sim 100mT$, there is an apparent change in chirality as the side of preferred growth reverses. The plotted velocity curves are also qualitatively similar. They are vertically offset indicating a chiral damping contribution. The velocity curves are also horizontally shifted like the curves observed previously, but the minimum occurs at a slightly larger in-plane field, indicating a slightly larger DMI. Based on the asymmetric component of velocity plotted in Fig. 6.10, the profile shape results from the combined effects of domain wall stiffness and chiral damping. Fitting the velocity curves gives a DMI value of $D = -0.365mJ/m^2$ and a chiral damping factor of $\alpha_{cd} = 0.46$. The extracted values are very similar to the values extracted from 6.2 and 6.3 which indicates very little contribution from the Ni/Pt interface on system DMI, but the results remain inconclusive.
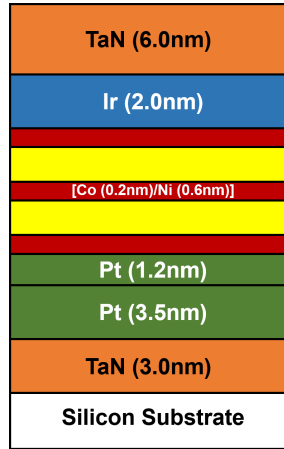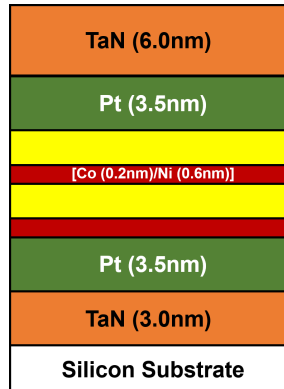
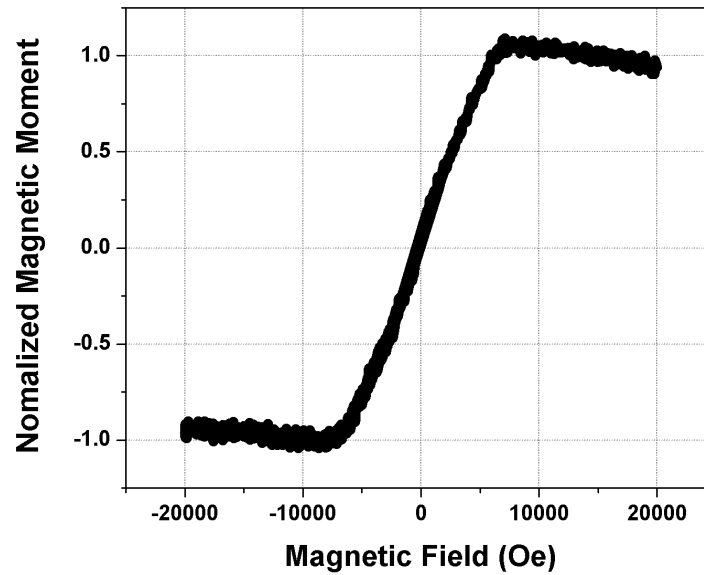Figure 6.10: Asymmetric multilayer with Pt/Co and Ni/Pt interfaces.
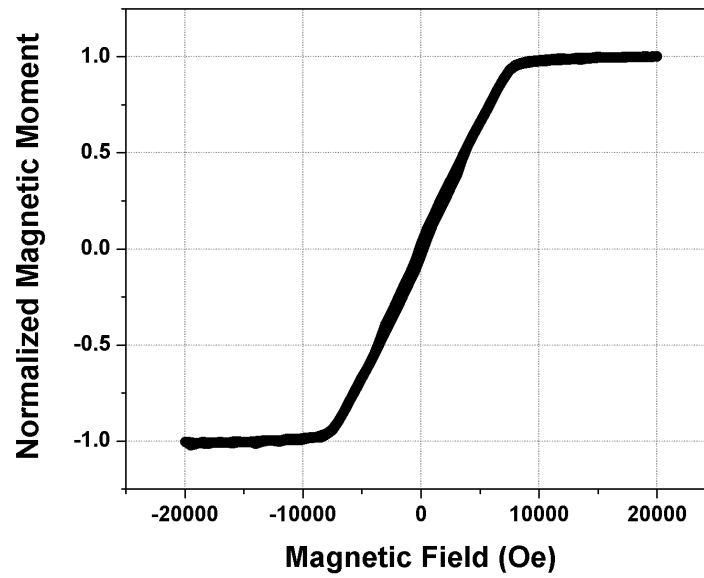
Figure 6.11: In-Plane M-H loop for $Pt/[Co/Ni]_2/Pt$ asymmetric multilayer showing magnetization along hard axis.
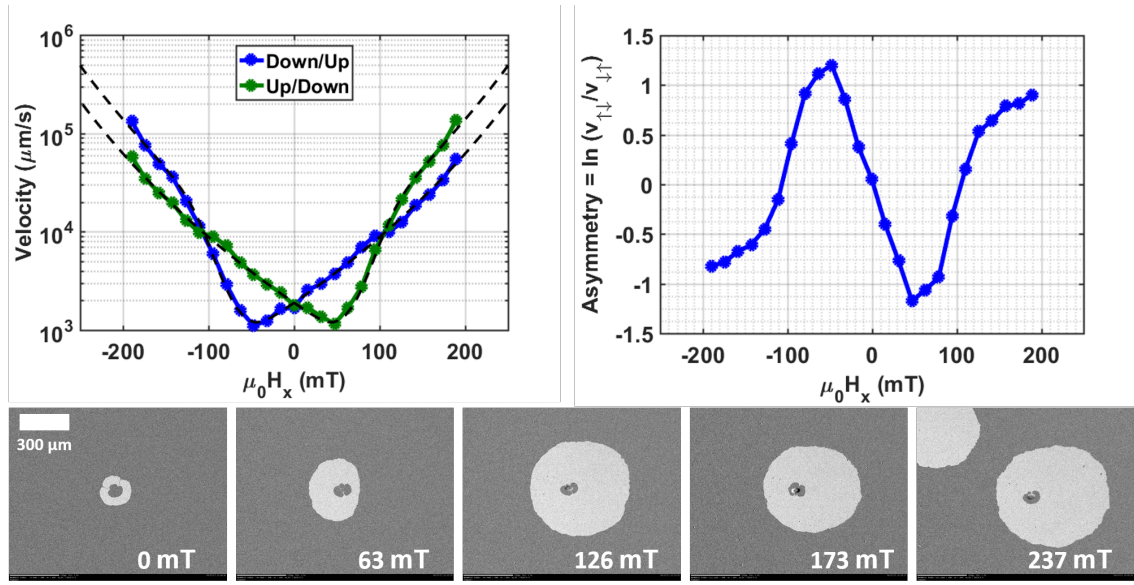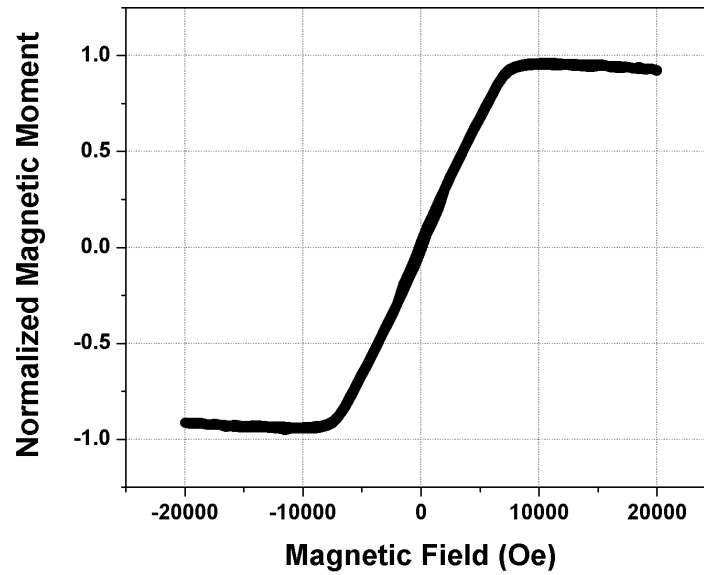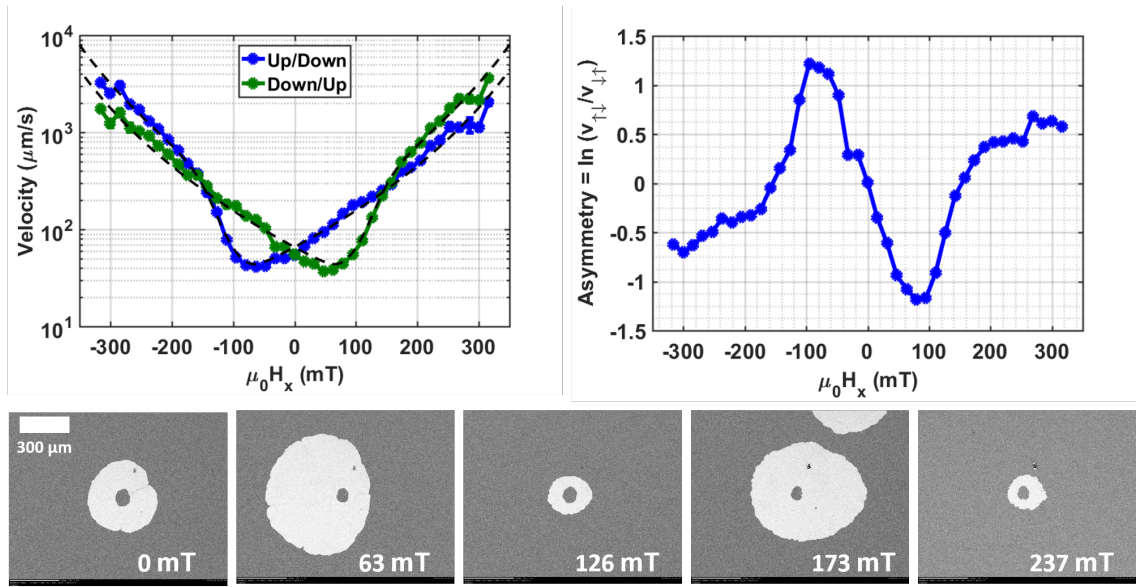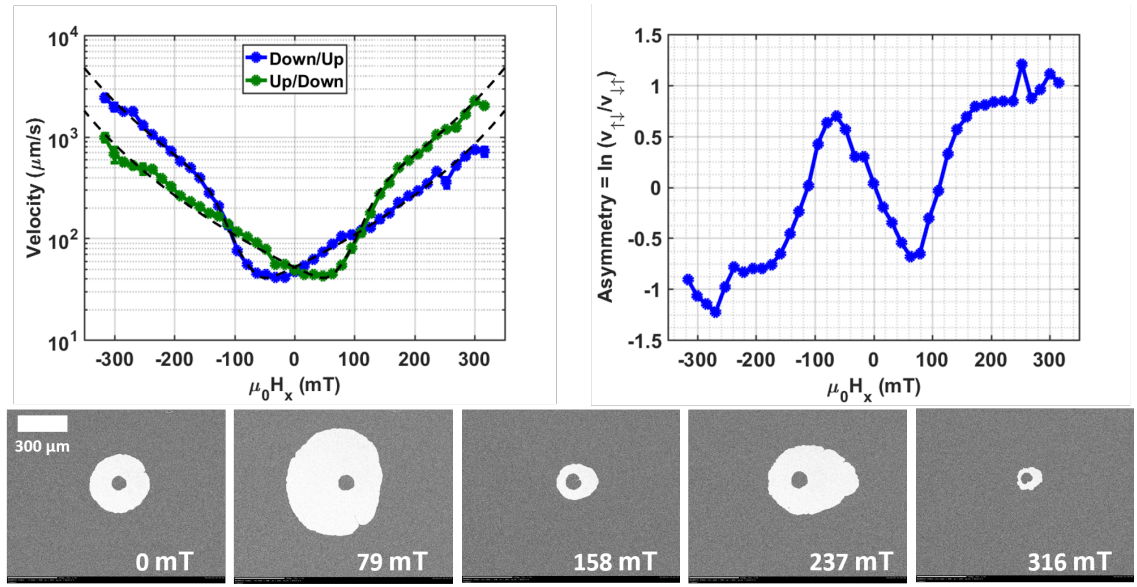
Figure 6.12: a) Domain wall velocity profile with fits using the Dispersive Stiffness Model. b) A_{creep} vs. applied in-plane field (H_x) c) Representative Kerr images at different in-plane fields applied in the positive x-direction.

6.5 Conclusions and Future Directions

In this chapter, preliminary experimental work was performed to elucidate the role terminating interfaces has in inducing interfacial DMI. Several samples were grown on Pt/Co seedlayer interfaces in indentical conditions in order to isolate the effects of the capping layer interfaces. We have characterized samples with Co/Pt, Co/Ir, Ni/Ir, and Ni/Pt capping layer interfaces. The extracted DMI and several relevant magnetic properties are tabulated in Fig. 6.13. Our findings suggest the Pt/Co interface from the seedlayer is much more significant compared to any of the interfaces used as a capping layer. We see that the interfacial DMI is consistently large despite changing the capping layer structure. This points to the Pt/Co interface dominating the spin-orbit interactions in the magnetic multilayer which contributes the most to the DMI in the system. When the capping layer is a symmetric Co/Pt interface, we observe a sharp decrease in DMI, as expected for structures that have a center of inversion. We also observe that the chiral weight found in symmetric $[Co/Ni/Co]$ multilayers is significantly different from asymmetric $[Co/Ni]$ multilayers, which may support an earlier observation where we postulated the chiral weight is intrinsic to the magnetic layer in a system. However, the chiral weight for the $[Co/Ni]$ multilayer is dramatically different when different capping layers are deposited, so that conclusion is not entirely supported. In conclusion, we have shown the significance of considering seeding layer and capping layer interfaces when engineering DMI even though we were unable to draw conclusions about the DMI from each individual interface quantitatively. This preliminary work shows the potential and motivation for quantitatively characterizing the DMI of different $Ferromagnet/HeavyMetal$ interface in order to design and engineer DMI materials more efficiently. We hope to incorporate our findings into related research where magnetic thin film superlattices must be optimized to induce skyrmions and other chiral magnetic textures. It will also be worthwhile to continue this work using computational methods for ab initio calculations of spin-orbit interactions between interfaces, a research thrust that we hope to continue with collaborators in the future.

Film Structure	M_s (kA/cm³)	H_k (T)	K_{eff} (J/m³)	DMI (mJ/m2)	Chiral Weight
Pt/[Co/Ni]$_2$/Co/Pt	622	~0.7-0.8	2.18×10^5	**-0.08**	**0.40**
Pt/[Co/Ni]$_2$/Co/Ir	615	~0.7-0.8	2.15×10^5	**-0.313**	**0.41**
Pt/[Co/Ni]$_2$/Ir	615	~0.7-0.8	2.46×10^5	**-0.386**	**0.30**
Pt/[Co/Ni]$_2$/Pt	600	~0.7-0.8	2.43×10^5	**-0.365**	**0.46**

Figure 6.13: Tabulated values for relevant magnetic properties and extracted values for interfacial DMI and chiral weight.

CHAPTER VII

Summary and Future Work

7.1 Summary

The primary goal of this research is to demonstrate the capability of tuning DMI in magnetic multilayers through seedlayer alloying. The ability to engineer DMI in materials shows great potential in designing spintronic devices for next generation technology. Alloying has traditionally been a widely used technique in the magnetics community for improving magnetic properties of materials for different applications. However, the idea of adjusting composition to tune DMI is something that has not been experimentally studied in much detail. By applying this technique to domain wall nanowire devices, we hope to show that alloying can be used to tune performance and efficiency in spintronics devices.

In the first part of this thesis, the experimental work was focused on developing a high throughput technique that can be used to characterize DMi in thin films accurately and efficiently. Currently, studying field-driven, asymmetric domain growth is a simple and popular way to characterize DMI strength in a thin film system. However, it has been shown to have some flaws, especially in the accuracy of the technique. Our work with anomalous domain growth behavior set the foundation for the development of a refined model that addresses a lot of those concerns. Our experimental work first demonstrated the significance of domain wall energy in determining equilibrium bubble shapes. Ultimately, our work with domain wall energy helped show that, it was the incorporation of domain wall elasticity (rather than energy) that provided a more accurate model for describing domain wall behavior in the creep regime.

In the second part of the thesis work, several magnetic systems were fabricated in order to test the effects of seedlayer composition on DMI. The $Pt - Ir$ and $Pt - Au$ alloys were the two systems that were experimentally characterized. The refined stiffness model was used as the primary method for characterizing DMI. Using this method, we demonstrated an almost linear relationship between composition and effective DMI. We were able to show that the addition of Ir and Au to a Pt seedlayer severely reduced the effective DMI in the system (more so with the addition of gold). In addition, we were also able to characterize the chiral damping property in our thin films, a new magnetic property that causes the anomalous velocity asymmetry seen in chiral domain walls. We show that Pt and Ir have significant chiral damping while Au appears to show lower chiral damping effects. Our findings were independently supported by collaborators through the BLS technique, showing remarkably similar conclusions. Finally, by fabricating thin film devices, we have also been able to show a correlation between seedlayer composittion and prototype nanowire device performance.

In the final section of this thesis, additional experiments were conducted to get more insight on effect of terminating interfaces on inducing DMI. Previous work in this thesis has mainly focused on engineering DMI through the seedlayer. Hwoever, it has been suggested in literature that a heavy metal capping layer will also contribute significantly to the overall DMI in a magnetic thin film. Our experimental work has shown that the DMI contribution from a Pt/Co seedlayer is significantly larger than contributions from Pt/Ir, Ni/Pt, and Ni/Ir interfaces. When the seedlayer is made up of the Pt/Co, the magnitude of the induced DMI was consistently large, regardless of the interface from the capping layer. The only instance that resulted in low DMI was the case where the film was symmetric and the terminating interface was Co/Pt. These preliminary findings have shown the significance of considering various heavy metal/ferromagnet interfaces for the purposes of engineering DMI in magnetic thin films.

7.2 Revisiting the Hypothesis

(1) Interfacial DMI in a magnetic multilayer can be optimized via filmstack structure and layer engineering to achieve DMI magnitudes larger than values found in pure Heavy Metal/Ferromagnet interfaces.

(2) The efficiency of current-driven domain wall motion in magnetic multilayers is directly correlated with DMI, which can be enhanced through seedlayer alloying.

The hypothesis we set out to address in this thesis work is actually two-fold. We have shown the possibility for the interfacial DMI in a magnetic thin film system to be tunable by engineering the composition in seed and capping layers. Early work also demonstrates the possibility of combining seed and capping layers to increase the total DMI in the system. In addition, we have shown that tuning the interfacial DMI in a magnetic system influences the efficiency and performance of domain wall motion in nanowire devices.

We have found that DMI can be tuned through seedlayer composition, but we could not achieve a peak value through alloying. The work in this thesis has demonstrated a monotomic relationship between composition and DMI. Although initial data suggests otherwise, we believe that DMI does not necessarily show a linear dependence on composition. However, the mechanism through which composition determines DMI is still unclear and requires more experimental and computational work. Alternatively, preliminary work showed the possibility to optimize DMI by using different heavy metal interfaces. More experimental and computational work is required to explore the DMI originating from a combination of the initializing and terminating interfaces. The ability to tune DMI in a system is promising in future spintronic applications that require fast, efficient, and stable domain wall motion. To that end, we have confirmed that device efficiency can be improved by optimizing DMI. In addition, we show that increasing DMI past a critical value will continue to improve device performance. Through DMI optimization, the properties of current-driven domain wall motion may change significantly, and will result in an improvement in performance and ef-

ficiency compared to using pure elements.

7.3 Future Work: Heavy-Metal Alloy Exploration for Seed and Capping Layers

Seed and capping layer optimization is an aspect of DMI that is still relatively unexplored. Some work has been done on different transition metals, but, the bulk of materials that would satisfy the criteria for high DMI has not been characterized. Pt, Ir, W, and Au are among those materials that have been characterized in literature. However, materials like Rh, Cr and V have not been studied experimentally. Even less attention has been given to the possibility of alloying transition metals for the purpose of improving interfacial DMI. The DMI characterization of uncommon transition metals and their potential to form alloyed seed and capping layers will be a major part of this project moving forward. Long term goals will be to explore new metals and to create alloys to characterize metals that have not been explored. The experimental evaluation of systems with varying initializing and terminating interfaces should be explored moving forward. In addition, there has been a lot of interest in the community to explore new multilayer designs, incorporating anti-ferromagnets and ferrimanetic layers to achieve efficient domain wall motion. Future characterization will also include BLS (Brillouin Light Spectroscopy), a technique that has been shown to characterize DMI in a system accurately [27, 33, 91], for independent characterization of thin films to verify our results. The additional effort will help verify the DMI that will be extracted from domain wall creep motion behavior through Kerr microscopy. Another aspect of materials exploration unexplored in this thesis work is the computational modeling of different heavy metal/ferromagnet interface combinations. The role of ab initio simulations (through the VASP and FLEUR packages) will play an important role in determining the potential and viability of unexplored combinations of alloys and seed/capping layers for engineering larger DMI materials. Going forward, the main focus of this research project will be exploring heavy-metal combinations in an effort to tune DMI.

7.4 Future Work: Improved Current-Induced Domain Wall Motion by DMI Optimization

Although the film level field driven characterization will be prioritized, device testing will still make up a significant portion of the thesis. In order to address the second part of our hypothesis, films with various seed and capping layer combinations and compositions will be fabricated and tested. In addition, one aspect of current induced domain wall motion not explored in this thesis work is current induced domain wall motion in the presence of an applied in-plane field. Theoretically, such a study would provide another means to characterize DMI in domain wall devices. The main complication from device testing is fabricating devices that can be tested in our experimental setup. One of the challenges about comparing samples of different compositions is controlling the different variables as best as possible, which will be simplified using our high throughput technique for film deposition. Another aspect that we have not yet explored is the effect of composition on spin-hall effect properties, which is extremely important for inducing domain wall motion. Future work will require more research on how seedlayer composition affects spin-transport properties in addition to DMI, as they originate from the same heavy metal layer. The main goal for this project was to identify the effects of seedlayer composition in device performance. In addition to that, the work shown in this thesis also introduced a high throughput way to characterize DMI in materials for thin film applications. Independent testing of nanowire devices will prove extremely valuable in confirming our film level findings and its viability as a high-throughput method.

7.5 Future Work: Publication Plan

Publications in Preparation

1. **D. Lau**, J. P. Pellegren, H.T. Nembach, J.M. Shaw, and V. Sokalski. Disentangling factors governing Dzyaloshinskii domain wall creep in Co/Ni thin films using Pt_xIr_{1-x} Seedlayers (*Physical Review Letters* or *Physical Review B*). (In Preparation)

Future Publications

2. Publications detailing the ab initio calculations of DMI in specific interfaces and comparison to experimental DMI characterization results.

   (Journal of Applied Physics or Physical Review B)

3. Publication detailing findings from current-induced domain wall motion experiments linking DMI in alloyed seedlayers to device performance

   (Journal of Applied Physics, AIP Advances, or IEEE Transactions on Magnetics)

BIBLIOGRAPHY

[1] B.D. Cullity and C.D. Graham. *Introduction to Magnetic Materials*. Wiley, 2 edition, 2009.

[2] Albert Fert, Vincent Cros, and Joao Sampaio. Skyrmions on the track. *Nat Nano*, 8(3):152–156, 03 2013.

[3] Ezequiel E. Ferrero, Sebastian Bustingorry, Alejandro B. Kolton, and Alberto Rosso. Numerical approaches on driven elastic interfaces in random media. *Comptes Rendus Physique*, 14(8):641 – 650, 2013. Disordered systems / Systèmes désordonnés.

[4] Luqiao Liu. Spin orbit electronics: From heavy metals to topological insulators. https://www.eecs.mit.edu/node/6509, May 2016. Accessed: 2017-06-15.

[5] Arne Brataas, Andrew D. Kent, and Hideo Ohno. Current-induced torques in magnetic materials. *Nature Materials*, 11(5):372–381, Apr 2012.

[6] D.C. Ralph and M.D. Stiles. Spin transfer torques. *Journal of Magnetism and Magnetic Materials*, 320(7):1190–1216, Apr 2008.

[7] Yan Li Roland K. Kawakami, Kathleen McCreary. *Nanoelectronics and Photonics Nanoelectronics and Photonics: From Atoms to Materials, Devices, and Architectures*, chapter Fundamentals of Spintronics in Metal and Semiconductor Systems. Springer Nature, 2008. Accessed: 2017-06-15.

[8] Sergio O. Valenzuela. Spin hall effect and spin transfer torques : An overview. http://benasque.org/2014magnetism/talks_contr/137_Valenzuela.pdf, 2014. Accessed: 2017-06-15.

[9] Alex Hubert and Rudolf Schafer. *Magnetic Domains: The Analysis of Magnetic Microstructures*. Springer Nature, 2009.

[10] Hans T. Nembach, Justin M. Shaw, Mathias Weiler, Emilie Jue, and Thomas J. Silva. Linear relation between heisenberg exchange and interfacial dzyaloshinskii-moriya interaction in metal films. *Nat Phys*, 11(10):825–829, 10 2015.

[11] M. Jaris, D. Lau, V. Sokalski, and H. Schmidt. Magnetization dynamics and damping behavior of co/ni multilayers with a graded ta capping layer. *Journal of Applied Physics*, 121(16):163903, 2017.

[12] Price Pellegren, Derek Lau, and Vincent Sokalski. Dispersive stiffness of dzyaloshinskii domain walls. *Physical Review Letters*, 09 2017.

[13] Jan-Philipp Hanke, Frank Freimuth, Stefan Blgel, and Yuriy Mokrousov. Higher-dimensional wannier interpolation for the modern theory of the dzyaloshinskiimoriya interaction: Application to co-based trilayers. *Journal of the Physical Society of Japan*, 87(4):041010, 2018.

[14] Stuart Parkin and See-Hun Yang. Memory on the racetrack. *Nat Nano*, 10(3):195–198, 03 2015.

[15] Stuart S. P. Parkin, Masamitsu Hayashi, and Luc Thomas. Magnetic domain-wall racetrack memory. *Science*, 320(5873):190–194, 2008.

[16] D. M. Bromberg, M. T. Moneck, V. M. Sokalski, J. Zhu, L. Pileggi, and J. G. Zhu. Experimental demonstration of four-terminal magnetic logic device with separate read- and write-paths. In *2014 IEEE International Electron Devices Meeting*, pages 33.1.1–33.1.4, Dec 2014.

[17] Masamitsu Hayashi, Luc Thomas, Rai Moriya, Charles Rettner, and Stuart S. P. Parkin. Current-controlled magnetic domain-wall nanowire shift register. *Science*, 320(5873):209–211, 2008.

[18] Daichi Chiba, Gen Yamada, Tomohiro Koyama, Kohei Ueda, Hironobu Tanigawa, Shunsuke Fukami, Tetsuhiro Suzuki, Norikazu Ohshima, Nobuyuki Ishiwata, Yoshinobu Nakatani, and Teruo Ono. Control of multiple magnetic domain walls by current in a co/ni nano-wire. *Applied Physics Express*, 3(7):073004, 2010.

[19] T. Koyama, D. Chiba, K. Ueda, K. Kondou, H. Tanigawa, S. Fukami, T. Suzuki, N. Ohshima, N. Ishiwata, Y. Nakatani, K. Kobayashi, and T. Ono. Observation of the intrinsic pinning of a magnetic domain wall in a ferromagnetic nanowire. *Nat Mater*, 10(3):194–197, 03 2011.

[20] L. Thomas, See-Hun Yang, Kwang-Su Ryu, B. Hughes, C. Rettner, Ding-Shuo Wang, Ching-Hsiang Tsai, Kuei-Hung Shen, and S. S. P. Parkin. Racetrack memory: A high-performance, low-cost, non-volatile memory based on magnetic domain walls. In *2011 International Electron Devices Meeting*, pages 24.2.1–24.2.4, Dec 2011.

[21] Kwang-Su Ryu, See-Hun Yang, and Stuart Parkin. Experimentally tunable chiral spin transfer torque in domain wall motion. *New Journal of Physics*, 18(5):053027, 2016.

[22] Kwang-Su Ryu, Luc Thomas, See-Hun Yang, and Stuart S. P. Parkin. Current induced tilting of domain walls in high velocity motion along perpendicularly magnetized micron-sized co/ni/co racetracks. *Applied Physics Express*, 5(9):093006, 2012.

[23] Kwang-Su Ryu, Luc Thomas, See-Hun Yang, and Stuart Parkin. Chiral spin torque at magnetic domain walls. *Nature Nanotechnology*, 8(7):527–533, Jun 2013.

[24] Kwang-Su Ryu, See-Hun Yang, Luc Thomas, and Stuart S. P. Parkin. Chiral spin torque arising from proximity-induced magnetization. *Nature Communications*, 5, May 2014.

[25] Carl Rod Nave. Hyperphysics. http://hyperphysics.phy-astr.gsu.edu/hbase/index.html, 2000.

[26] Dmitry Zakharov, Hans-Albrecht Krug von Nidda, Mikhail Eremin, Joachim Deisenhofer, Rushana Eremina, and Alois Loidl. Anisotropic exchange in spin chains. In Bernard Barbara, Yosef Imry, G. Sawatzky, and P.C.E. Stamp, editors, *Quantum Magnetism*, pages 193–297. Springer Nature, 2006.

[27] V E Dmitrienko, E N Ovchinnikova, S P Collins, G Nisbet, and G Beutier. An x-ray study of the dzyaloshinskii-moriya interaction in the weak ferromagnet febo 3. *Journal of Physics: Conference Series*, 519(1):012003, 2014.

[28] Christopher L. Henley. Spin hamiltonians and exchange interactions. http://www.lassp.cornell.edu/clh/p654/MM-Lec0.pdf.

[29] I. Dzyaloshinsky. A thermodynamic theory of "weak" ferromagnetism of antiferromagnetics. *Journal of Physics and Chemistry of Solids*, 4(4):241 – 255, 1958.

[30] Tôru Moriya. Anisotropic superexchange interaction and weak ferromagnetism. *Phys. Rev.*, 120:91–98, Oct 1960.

[31] M. J. Benitez, A. Hrabec, A. P. Mihai, T. A. Moore, G. Burnell, D. McGrouther, C. H. Marrows, and S. McVitie. Magnetic microscopy and topological stability of homochiral néel domain walls in a pt/co/alox trilayer. 6:8957 EP –, 12 2015.

[32] Gong Chen, Tianping Ma, Alpha T. N'Diaye, Heeyoung Kwon, Changyeon Won, Yizheng Wu, and Andreas K. Schmid. Tailoring the chirality of magnetic domain walls by interface engineering. 4:2671 EP –, 10 2013.

[33] Hongxin Yang, André Thiaville, Stanislas Rohart, Albert Fert, and Mairbek Chshiev. Anatomy of dzyaloshinskii-moriya interaction at co/pt interfaces. *Phys. Rev. Lett.*, 115:267210, Dec 2015.

[34] M T Johnson, P J H Bloemen, F J A den Broeder, and J J de Vries. Magnetic anisotropy in metallic multilayers. *Reports on Progress in Physics*, 59(11):1409, 1996.

[35] G. H. O. Daalderop, P. J. Kelly, and F. J. A. den Broeder. Prediction and confirmation of perpendicular magnetic anisotropy in co/ni multilayers. *Phys. Rev. Lett.*, 68:682–685, Feb 1992.

[36] I. Gross, L. J. Martínez, J.-P. Tetienne, T. Hingant, J.-F. Roch, K. Garcia, R. Soucaille, J. P. Adam, J.-V. Kim, S. Rohart, A. Thiaville, J. Torrejon, M. Hayashi, and V. Jacques. Direct measurement of interfacial dzyaloshinskii-moriya interaction in $x|$CoFeB$|$MgO heterostructures with a scanning nv magnetometer ($x =$ Ta, TaN, and W). *Phys. Rev. B*, 94:064413, Aug 2016.

[37] A. Hrabec, N. A. Porter, A. Wells, M. J. Benitez, G. Burnell, S. McVitie, D. McGrouther, T. A. Moore, and C. H. Marrows. Measuring and tailoring the dzyaloshinskii-moriya interaction in perpendicularly magnetized thin films. *Physical Review B*, 90(2), Jul 2014.

[38] R. Soucaille, M. Belmeguenai, J. Torrejon, J.-V. Kim, T. Devolder, Y. Roussigné, S.-M. Chérif, A. A. Stashkevich, M. Hayashi, and J.-P. Adam. Probing the dzyaloshinskii-moriya interaction in cofeb ultrathin films using domain wall creep and brillouin light spectroscopy. *Physical Review B*, 94(10), Sep 2016.

[39] Seonghoon Woo, Kai Litzius, Benjamin Krüger, Mi-Young Im, Lucas Caretta, Kornel Richter, Maxwell Mann, Andrea Krone, Robert M. Reeve, Markus Weigand, and et al. Observation of room-temperature magnetic skyrmions and their current-driven dynamics in ultrathin metallic ferromagnets. *Nature Materials*, 15(5):501–506, Feb 2016.

[40] Dae-Yun Kim, Duck-Ho Kim, and Sug-Bong Choe. Intrinsic asymmetry in chiral domain walls due to the dzyaloshinskii–moriya interaction. *Applied Physics Express*, 9(5):053001, 2016.

[41] Jiawei Yu, Xuepeng Qiu, Yang Wu, Jungbum Yoon, Praveen Deorani, Jean Mourad Besbas, Aurelien Manchon, and Hyunsoo Yang. Spin orbit torques and dzyaloshinskii-moriya interaction in dual-interfaced co-ni multilayers. 6:32629 EP –, 09 2016.

[42] Soong-Geun Je, Duck-Ho Kim, Sang-Cheol Yoo, Byoung-Chul Min, Kyung-Jin Lee, and Sug-Bong Choe. Asymmetric magnetic domain-wall motion by the dzyaloshinskii-moriya interaction. *Phys. Rev. B*, 88:214401, Dec 2013.

[43] M Vaňatka, J-C Rojas-Sánchez, J Vogel, M Bonfim, M Belmeguenai, Y Roussigné, A Stashkevich, A Thiaville, and S Pizzini. Velocity asymmetry of dzyaloshinskii domain walls in the creep and flow regimes. *Journal of Physics: Condensed Matter*, 27(32):326002, 2015.

[44] Satoru Emori, Uwe Bauer, Sung-Min Ahn, Eduardo Martinez, and Geoffrey S. D. Beach. Current-driven dynamics of chiral ferromagnetic domain walls. *Nature Materials*, 12(7):611–616, Jun 2013.

[45] J.C Slonczewski. Currents and torques in metallic magnetic multilayers. *Journal of Magnetism and Magnetic Materials*, 247(3):324 – 338, 2002.

[46] L. Berger. Analysis of measured transport properties of domain walls in magnetic nanowires and films. *Phys. Rev. B*, 73:014407, Jan 2006.

[47] L. Berger. Relation between damping, current-induced torques, and wall resistance for domain walls in magnetic nanowires. *Phys. Rev. B*, 75:174401, May 2007.

[48] Sonali Mukherjee and Luc Berger. Switching of composite media by wall propagation. *Journal of Applied Physics*, 99(8):08Q909, 2006.

[49] J. E. Hirsch. Spin hall effect. *Phys. Rev. Lett.*, 83:1834–1837, Aug 1999.

[50] Jairo Sinova, Sergio O. Valenzuela, J. Wunderlich, C. H. Back, and T. Jungwirth. Spin hall effects. *Rev. Mod. Phys.*, 87:1213–1260, Oct 2015.

[51] Yi Wang, Praveen Deorani, Xuepeng Qiu, Jae Hyun Kwon, and Hyunsoo Yang. Determination of intrinsic spin hall angle in pt. *Applied Physics Letters*, 105(15):152412, 2014.

[52] Luqiao Liu, O. J. Lee, T. J. Gudmundsen, D. C. Ralph, and R. A. Buhrman. Current-induced switching of perpendicularly magnetized magnetic layers using spin torque from the spin hall effect. *Physical Review Letters*, 109(9), Aug 2012.

[53] A. V. Khvalkovskiy, V. Cros, D. Apalkov, V. Nikitin, M. Krounbi, K. A. Zvezdin, A. Anane, J. Grollier, and A. Fert. Matching domain-wall configuration and spin-orbit torques for efficient domain-wall motion. *Physical Review B*, 87(2), Jan 2013.

[54] Luqiao Liu, Chi-Feng Pai, Y Li, HW Tseng, DC Ralph, and RA Buhrman. Spin-torque switching with the giant spin hall effect of tantalum. *Science*, 336(6081):555–558, 2012.

[55] K.H.J. Buschow. *Concise Encyclopedia of Magnetic and Superconducting Materials*. Advances in Materials Sciences and Engineering. Elsevier Science, 2005.

[56] Juyoung Jeong, Ilkyu Yang, Jinho Yang, Oscar E. Ayala-Valenzuela, Dirk Wulferding, J.-S. Zhou, John B. Goodenough, Alex de Lozanne, J. F. Mitchell, Neliza Leon, Roman Movshovich, Yoon Hee Jeong, Han Woong Yeom, and Jeehoon Kim. Magnetic domain tuning and the emergence of bubble domains in the bilayer manganite $la_{2-2x}sr_{1+2x}mn_2o_7$ ($x = 0.32$). *Phys. Rev. B*, 92:054426, Aug 2015.

[57] Hao-Liang Liu, Wei He, Hai-Feng Du, Qiong Wu, Ya-Peng Fang, Yun Zhu, Jian-Wang Cai, and Zhao-Hua Cheng. Direct observation of dendritic domain growth in perpendicular magnetic anisotropy cofe/pt multilayers. *Journal of Magnetism and Magnetic Materials*, 323(17):2238 – 2242, 2011.

[58] R. C. Woodward, A. M. Lance, R. Street, and R. L. Stamps. Variation of the magnetic domain structure with reversal field (invited). *Journal of Applied Physics*, 93(10):6567–6571, 2003.

[59] R. D. Shull, Y. L. Iunin, Y. P. Kabanov, V. I. Nikitenko, O. V. Skryabina, and C. L. Chien. Influence of pt spacer thickness on the domain nucleation in ultrathin co/pt/co trilayers. *Journal of Applied Physics*, 113(17):17C101, 2013.

[60] Guangzhong Wang, Zongzhi Zhang, Bin Ma, and Q. Y. Jin. Magnetic anisotropy and thermal stability study of perpendicular co/ni multilayers. *Journal of Applied Physics*, 113(17):17C111, 2013.

[61] En Yang, Vincent M. Sokalski, Matthew T. Moneck, David M. Bromberg, and Jian-Gang Zhu. Annealing effect and under/capping layer study on co/ni multilayer thin films for domain wall motion. *Journal of Applied Physics*, 113(17):17C116, 2013.

[62] Jeong-Heon Park, Chando Park, Taehee Jeong, Matthew T. Moneck, Noel T. Nufer, and Jian-Gang Zhu. Copt multilayer based magnetic tunnel junctions using perpendicular magnetic anisotropy. *Journal of Applied Physics*, 103(7):07A917, 2008.

[63] P. Mazalski, Z. Kurant, A. Maziewski, M. O. Liedke, J. Fassbender, L. T. Baczewski, and A. Wawro. Ion irradiation induced enhancement of out-of-plane magnetic anisotropy in ultrathin co films. *Journal of Applied Physics*, 113(17):17C109, 2013.

[64] R. Lavrijsen, D. M. F. Hartmann, A. van den Brink, Y. Yin, B. Barcones, R. A. Duine, M. A. Verheijen, H. J. M. Swagten, and B. Koopmans. Asymmetric magnetic bubble expansion under in-plane field in pt/co/pt: Effect of interface engineering. *Physical Review B*, 91(10), Mar 2015.

[65] Derek Lau, Vignesh Sundar, Jian-Gang Zhu, and Vincent Sokalski. Energetic molding of chiral magnetic bubbles. *Physical Review B*, 94(6), Aug 2016.

[66] S. Pizzini, J. Vogel, S. Rohart, L. D. Buda-Prejbeanu, E. Jué, O. Boulle, I. M. Miron, C. K. Safeer, S. Auffret, G. Gaudin, and A. Thiaville. Chirality-induced asymmetric magnetic nucleation in Pt/Co/alo$_x$ ultrathin microstructures. *Phys. Rev. Lett.*, 113:047203, Jul 2014.

[67] Conyers Herring. Some theorems on the free energies of crystal surfaces. *Phys. Rev.*, 82:87–93, Apr 1951.

[68] G. Wulff. Zur frage der geschwindigkeit des wachstums und der auflösung der krystallflagen. *Zeitschrift für Krystallographie und Mineralogie*, 34 (5/6):449–530, 1901.

[69] James Price Pellegren. Analyzing creep mobility of dzyaloshinskii domain walls with an effective elastic band model. *Dissertations*, (1088), 2017.

[70] Kab-Jin Kim, Jae-Chul Lee, Sung-Min Ahn, Kang-Soo Lee, Chang-Won Lee, Young Jin Cho, Sunae Seo, Kyung-Ho Shin, Sug-Bong Choe, and Hyun-Woo Lee. Interdimensional universality of dynamic interfaces. *Nature*, 458(7239):740–742, 04 2009.

[71] S. Lemerle, J. Ferré, C. Chappert, V. Mathet, T. Giamarchi, and P. Le Doussal. Domain wall creep in an ising ultrathin magnetic film. *Phys. Rev. Lett.*, 80:849–852, Jan 1998.

[72] Emilie Jué, C. K. Safeer, Marc Drouard, Alexandre Lopez, Paul Balint, Liliana Buda-Prejbeanu, Olivier Boulle, Stephane Auffret, Alain Schuhl, Aurelien Manchon, and et al. Chiral damping of magnetic domain walls. *Nature Materials*, 15(3):272–277, Dec 2015.

[73] Collins Ashu Akosa, Ioan Mihai Miron, Gilles Gaudin, and Aurélien Manchon. Phenomenology of chiral damping in noncentrosymmetric magnets. *Physical Review B*, 93(21), Jun 2016.

[74] Kh. Zakeri, Y. Zhang, T.-H. Chuang, and J. Kirschner. Magnon lifetimes on the fe(110) surface: The role of spin-orbit coupling. *Phys. Rev. Lett.*, 108:197205, May 2012.

[75] A. Belabbes, G. Bihlmayer, F. Bechstedt, S. Blügel, and A. Manchon. Hund's rule-driven dzyaloshinskii-moriya interaction at $3d-5d$ interfaces. *Phys. Rev. Lett.*, 117:247202, Dec 2016.

[76] S. Mankovsky and H. Ebert. Accurate scheme to calculate the interatomic dzyaloshinskii-moriya interaction parameters. *Phys. Rev. B*, 96:104416, Sep 2017.

[77] Michael E McHenry, Matthew A Willard, and David E Laughlin. Amorphous and nanocrystalline materials for applications as soft magnets. *Progress in Materials Science*, 44(4):291 – 433, 1999.

[78] M. A. Willard, D. E. Laughlin, M. E. McHenry, D. Thoma, K. Sickafus, J. O. Cross, and V. G. Harris. Structure and magnetic properties of (fe0.5co0.5)88zr7b4cu1 nanocrystalline alloys. *Journal of Applied Physics*, 84(12):6773–6777, 1998.

[79] En Yang and David E. Laughlin. L10 fept-oxide columnar perpendicular media with high coercivity and small grain size. *Journal of Applied Physics*, 104(2):023904, 2008.

[80] S. Jeong, Y. N. Hsu, D. E. Laughlin, and M. E. McHenry. Magnetic properties of nanostructured copt and fept thin films. *IEEE Transactions on Magnetics*, 36(5):2336–2338, Sep 2000.

[81] Sangki Jeong, M. E. McHenry, and D. E. Laughlin. Growth and characterization of l10 fept and copt (001) textured polycrystalline thin films. *IEEE Transactions on Magnetics*, 37(4):1309–1311, Jul 2001.

[82] Hua Yuan and David E. Laughlin. Effects of substrate bias on magnetocrystalline anisotropy ku of copt thin films with increasing pt content. *Journal of Applied Physics*, 105(7):07A712, 2009.

[83] S.F. Cheng, V.K. Sinha, Y. Xu, J.M. Elbicki, E.B. Boltich, W.E. Wallace, S.G. Sankar, and D.E. Laughlin. Magnetic and structural properties of smtife11-xcox alloys. *Journal of Magnetism and Magnetic Materials*, 75(3):330 – 338, 1988.

[84] Seonghoon Woo, Kai Litzius, Benjamin Kruger, Mi-Young Im, Lucas Caretta, Kornel Richter, Maxwell Mann, Andrea Krone, Robert M. Reeve, Markus Weigand, Parnika Agrawal, Ivan Lemesh, Mohamad-Assaad Mawass, Peter Fischer, Mathias Klaui, and Geoffrey S. D. Beach. Observation of room-temperature magnetic skyrmions and their current-driven dynamics in ultrathin metallic ferromagnets. *Nat Mater*, 15(5):501–506, 05 2016.

[85] M. Arora, R. Hübner, D. Suess, B. Heinrich, and E. Girt. Origin of perpendicular magnetic anisotropy in co/ni multilayers. *Phys. Rev. B*, 96:024401, Jul 2017.

[86] Andr Thiaville, Stanislas Rohart, milie Ju, Vincent Cros, and Albert Fert. Dynamics of dzyaloshinskii domain walls in ultrathin magnetic films. *EPL (Europhysics Letters)*, 100(5):57002, 2012.

[87] PPJ Haazen, E Murè, JH Franken, Reinoud Lavrijsen, HJM Swagten, and Bert Koopmans. Domain wall depinning governed by the spin hall effect. *Nature materials*, 12(4):299, 2013.

[88] Jacob Torrejon, Junyeon Kim, Jaivardhan Sinha, Seiji Mitani, Masamitsu Hayashi, Michihiko Yamanouchi, and Hideo Ohno. Interface control of the magnetic chirality in cofeb/mgo heterostructures with heavy-metal underlayers. *Nature communications*, 5:4655, 2014.

[89] S. Tacchi, R. E. Troncoso, M. Ahlberg, G. Gubbiotti, M. Madami, J. Åkerman, and P. Landeros. Interfacial dzyaloshinskii-moriya interaction in Pt/CoFeB films: Effect of the heavy-metal thickness. *Phys. Rev. Lett.*, 118:147201, Apr 2017.

[90] Abderrezak Belabbes, Gustav Bihlmayer, Stefan Blügel, and Aurélien Manchon. Oxygen-enabled control of dzyaloshinskii-moriya interaction in ultra-thin magnetic films. *Scientific reports*, 6:24634, 2016.

[91] Jaehun Cho, Nam-Hui Kim, Sukmock Lee, June-Seo Kim, Reinoud Lavrijsen, Aurelie Solignac, Yuxiang Yin, Dong-Soo Han, Niels J. J. van Hoof, Henk J. M. Swagten, Bert Koopmans, and Chun-Yeol You. Thickness dependence of the interfacial dzyaloshinskii–moriya interaction in inversion symmetry broken systems. 6:7635 EP –, 07 2015.